Modelling of fullerenes on silicon surfaces

by

David John King

A Doctoral Thesis

Submitted in partial fulfilment of the requirements for the award of Doctor of Philosophy of Loughborough University

8th September 2008

Acknowledgments

Firstly I would like to thank my supervisor Dr. Steven Kenny, for his guidance, support, continued understanding, and motivation when needed, which have ensured that I have reached the end of my research.

I would like to thank EPSRC and Loughborough University for providing me with the necessary funding and equipment to carry out my research.

I thank my family, in particular my parents and brother, for their unconditional support, understanding and belief throughout my research; words cannot even attempt to express how much my family have helped me.

I would also like to extend my appreciation to all of the postgraduate researchers who I have been privileged enough to share offices with during the period of my research, as they helped to provide an productive and at times enjoyable, working environment.

Additionally I would like to acknowledge the help I have received, directly or otherwise, from all the members of the materials modelling research group, both past and present.

Finally, the last year of my research bought with it some extra difficulties, so I would like to extend my eternal gratitude to all the friends and university staff who have helped during this time, and in particular to Karen Watts, whose support and encouragement has been invaluable.

"A mathematician is a blind man in a dark room looking for a black cat which isn't there."

Charles Darwin (English naturalist) [1809-1882]

"I may not have gone where I intended to go, but I think I have ended up where I needed to be."

Douglas Adams (English humourist & science fiction novelist) [1952 - 2001]

Abstract

An extension to the capabilities of an *ab-initio* density functional theory package, PLATO, has been undertaken. This concerned the calculation of Slater-Koster integrals and their derivatives, via the recursive methods initially proposed by Podolskiy and Vogl, and developed by Elena and Meister. This extension provides the ability to include the previously unavailable f-orbitals (and beyond) within PLATO calculations. Calculations have been performed, including f-orbitals, on silver, silicon and nitrogen systems. The results show a modest improvement, in terms of the convergence of the total energies calculated, when comparing the calculations including f-orbitals to those without. The impact on computational time is mixed, with both decreases and increases in compuational time demonstrated, dependent on the system in question and the type of calculation performed.

The interactions between C_{60} molecules and the Si (100) surface, as well as the interactions between the endohedrally doped N@C_{60} molecules and the Si (100) surface have been explored via *ab-initio* total energy calculations. Configurations which have the cage located upon the dimer row bonded to two dimers (r2) and within the dimer trench bonded to four dimers (t4) have been investigated, as these have previously been found to be the most stable for the C_{60} molecule. We show that our results for the adsorption of the C_{60} molecule upon the Si (100) surface are comparable with previous studies. We have investigated the differences between the adsorption of the C_{60} and N@C_{60} molecules upon the Si (100) surface and found that there are only minimal differences. It is shown that the effects on the endohedral nitrogen atom, due to its placement within the fullerene cage, are small. Bader analysis has been used to explore differences between the C_{60} and N@C_{60} molecules.

The interactions between pairs of C_{60} molecules adsorbed upon the Si (100) surface have also been studied. The same selection of t4 configurations used

for the isolated fullerenes is explored in all possible pairs of fullerene configuration combinations. A previous study by Frangou explored pairs of fullerenes in adjacent bonding sites on the silicon surface, this study, however, investigates bonding sites separated by one silicon dimer. Comparisons between the two studies confirm the trend of the combinations becoming more favourable at a greater fullerene separation. There are several cases where the combined pair of fullerenes are less favourable than the two isolated cases, so these are studied in-depth. The separation chosen in our study reflects the experimental separation observed by Moriarty *et al.*.

Contents

List of Figures

List of Tables

Chapter 1

Introduction

It has been over twenty years since the allotrope of carbon commonly known as the fullerene was first discovered [1]. This quite remarkable molecule possesses a cage structure constructed of pentagonal and hexagonal faces. The number of constituent carbon atoms can vary greatly, however the most common structure size consists of sixty atoms. This particular variation is named buckminster-fullerene, and has a high degree of symmetry.

Many different and varied applications for fullerenes have been suggested over the years since the molecules were first discovered. Several medical uses have been proposed, such as the exohedral binding of specific antibiotics to the fullerene cage, enabling the targeting of resistant bacteria and even certain cancer cells, such as melanoma. Another medical use is as chemical sponges, a water-based solution of fullerenes could reduce the tissue damage caused by free radicals following a head injury or a stroke (as the fullerenes could retain the free radicals). There have also been more commercial applications such as using the fullerenes as "molecular ball bearings" in lubricants or using the fullerenes to replace conventional photocopier toner (Xerox owns patents for this).

It has been shown that if an endohedral species is placed within the confines of the fullerene cage, then the endohedral species behaves as if it were in isolation, with little or no interaction with the fullerene cage itself [2]. Of course this depends on the size of the atom or molecule that is placed within the cage, as

the cage needs to be large enough to adequately house the endohedral species. Individual C_{60} fullerene molecules have been successfully manipulated across a surface with a scanning tunneling microscope (STM) tip [3, 4], and multiple C_{60} fullerene molecules have also been successfully manipulated with a STM tip, where the interactions between the fullerene molecules is of great interest. Only a small amount of the cage actually interacts with the surface itself, because of the the curvature of the cage (which is due to the pentagonal regions of the cage's surface). These properties, as well as others, make the study of endohedrally doped fullerenes an exciting area of research, that may have a far-reaching impact in the burgeoning field of nanotechnology.

The topic of quantum computing is an emerging technology, that in spite of recent rapid progress, is still in its infancy. This is illustrated by the large number of potential candidates that are being investigated as quantum computing solutions. Quantum computing makes direct use of quantum mechanical phenomena such as superposition and entanglement in order to to perform operations on data. Classically computational information is stored as bits, where each bit contains either a one or a zero. The quantum equivalent of bits are qubits (quantum bits), where each qubit holds either a one, a zero or a quantum superposition of these.

A number of differing solid-state quantum computing architectures have been proposed that rely on the unique properties of endohedral fullerenes (some of which are mentioned above), in order to represent the qubits, within the system. Some of these schemes suggest the usage of chains of endohedral fullerenes, with alternating endohedral species (nitrogen and phosphorus have been discussed as candidates) [5, 6]. The use of both the electronic and nuclear spin as qubits has also been discussed [6]. There are still some fundamental issues that need to be addressed with an architecture of this type, for example the qubit readout, however various solutions have been suggested [6].

Many studies [7, 8, 9, 10, 11, 12] have been carried out experimentally which show that the C_{60} molecule adsorbs in the dimer trench at room temperature,

and is only observed above the dimer row when the system is heated. A study of the larger endohedral La@C_{82} molecules suggested that the adsorption of an endohedral molecule is similar to that of a fullerene without the presence of an endohedral atom [13].

The research presented in this thesis is intended to investigate the initial *ab-initio* studies [2, 14, 15, 16, 17] by re-evaluating the original C_{60} in isolation upon the silicon surface systems, before moving onto new systems involving endohedral and multiple fullerenes. Before this is possible, it is important to first discuss the methodology of the calculations we have performed. This is addressed in Chapter 2, which explores *ab-initio* calculations and the code, PLATO [18], that we employ in order to model all of the systems we have considered. The methodology that underlies PLATO is discussed, and a detailed description of how PLATO actually operates, is included.

In Chapter 3, we further explore a specific aspect of the calculations within PLATO, namely the calculation of the Slater-Koster integrals and their derivatives [19]. Two approaches to the calculation of the Slater-Koster integrals are evaluated, the most suitable of which [20, 21] was then implemented. Here we discuss this significant extension to the capabilities of PLATO, which we have added as part of our research. This is discussed in-depth, and several aspects of modern programming techniques are illustrated before we elaborate on the testing and evaluation methods performed. The potential scope of this extension to PLATO is also addressed.

An introduction to the geometry and properties of fullerene molecules is given in Chapter 4; following on from this there is a discussion of the types of silicon surface reconstructions that are typically used for systems of this type. The numerous different orientations for the placement of a fullerene molecule on the Si (100) surface are then explored. We then discuss a selection of previous experimental studies, starting with the study that discovered the fullerene molecules in the first place [1], before commenting on several studies [12, 22] that have investigated the manipulation of C_{60} molecules that have adsorbed

onto the silicon surface. Finally experimental studies on endohedral fullerenes are introduced. These cover both the physical creation and properties of these molecules [23] and the most exciting (and relevant to our interests) application for endohedral fullerenes, namely spin based quantum computing [5]. We conclude by discussing the selection of computational studies [2, 14, 15, 16, 17], that form the basis for our own calculations.

Our work on the adsorption of isolated C_{60} and $N@C_{60}$ molecules upon the Si (100) surface, is then presented in Chapter 5. Our results are then compared with previous computational studies [2, 14, 15, 16, 17], and an in-depth analysis of our work is given. This evaluation explores all aspects of the fullerene molecules adsorption onto the silicon surface, including binding energies, the properties of the bonds involved (both the C-Si bonds formed and the internal rebonding within the fullerene cage), and an analysis of how the endohedral nitrogen atom is affected by the fullerene cage, as well as the impact its presence has on the fullerene molecule. Comparisons between the C_{60} and $N@C_{60}$ molecules are made, with particular attention being paid to the specific qualities that would be required for the development of a spin based quantum computer using $N@C_{60}$ molecules. These results have allowed for favourable conclusions to be made concerning the potential applications of $N@C_{60}$ molecules.

The investigation we have performed concerning the adsorption of multiple C_{60} molecules upon the silicon surface is presented in Chapter 6. This begins with the discussion of previous studies into systems of this type [4, 24], and then of the changes required in terms of the simulation cell required, from those implemented in Chapter 5. An initial study into the affects of periodic fullerene repeats, on both of these types of simulation cells, is then presented with some interesting conclusions drawn. An exploration of the combinations that the fullerene configurations can take upon the silicon surface is performed, in order to formulate a definitive list of the calculations required. The favourability of the systems are then discussed and the separation of the fullerene pairs are also investigated, with comparisons being made to the previous computational study

[24]. Several interesting combinations are then explored and discussed more in-depth, before some general conclusions are drawn.

In Chapter 7 (which is the final chapter) we draw some overall conclusions from the research we have performed, and make some recommendations and proposals for future studies related to our own work.

Chapter 2

Density functional theory methodology

2.1 Background theory

In order to study the interactions of molecules such as fullerenes, there are two options open to the modern scientist. The first being the traditional method of experimental study, and the second being computational simulation. While both techniques have their own positives and negatives, for a genuinely complete understanding, both methods should be implemented. For the purpose of this research, however, we have performed computational simulations, because as mathematicians our expertise lies more in the theoretical than the practical.

When it comes to computational simulations, there are two main methodologies that are usually implemented in order to study problems of this type. These are classical mechanics, which typically in this context equates to empirical potential calculations, and quantum mechanics, which in our case means *ab-initio* calculations. As with everything there are drawbacks and benefits to both techniques. The reason for our choice of *ab-initio* calculations is that they allow a more precise examination of systems. However, due to the large computational cost incurred, this level of precision is limited to much smaller systems than classical mechanics is capable of modelling.

2.1.1 Schrödinger's equation

Solving Schrödinger's equation, for the system that is being studied, is the crux of quantum mechanical *ab-initio* calculations, as the time dependence of quantum mechanical systems is described by Schrödinger's equation. For every instantaneous state of the system there is a unit vector (in the complex Hilbert space[1]). As the state of the system, in general, changes over time, the state vector is thus a function of time. Schrödinger's equation provides a quantitive description of the rate of change of this state vector. For every time-independent Hamiltonian, H, there exists a set of quantum states, known as energy eigenstates, that satisfy the time independent Schrödinger equation (see Equation 2.1).

$$H\Psi = E\Psi \tag{2.1}$$

Such a state possesses a definite total energy, whose value, E, is the eigenvalue of the state vector with the Hamiltonian. It has been shown that the time-independent Schrödinger equation can be solved exactly for the hydrogen atom. However, solving the time-independent Schrödinger equation for anything more complex than a hydrogen atom (in other words any system that is not an isolated hydrogen atom, *i.e.* everything else!), requires a number of approximations which are subsequently discussed.

2.1.2 The Born-Oppenheimer approximation

This approximation, which was proposed by Born and Oppenheimer in 1927 [25], still plays a vital role in modern quantum mechanics. It allows the wave function of a molecule to be broken up into its electronic, $\psi_{electronic}$, and nuclear, $\psi_{nuclear}$, components (see equation 2.2).

[1]By extending the methods of vector algebra from two and three dimensions to infinite dimensional spaces, it is possible to measure distances and angles within the infinite dimensional spaces. This concept is known as a Hilbert space.

$$\Psi_{total} = \psi_{electronic} \times \psi_{nuclear} \tag{2.2}$$

Without being able to separate the wave function into these two parts, the number of variables within the time independent Schrödinger equation would be unfeasibly large in terms of computational effort. The Born-Oppenheimer approximation relies on the colossal difference between the mass of a nucleus and that of an electron. Since the Coulombic potentials for the electronic and nuclear parts are of the same magnitude, the difference in mass leads to a massive difference in the velocities. This means that for the $\psi_{electronic}$ calculation the nuclei are fixed (they are treated as stationary due to their slow velocity relative to that of the electrons), while the electrons relax to an energy minimum. This generates a set of electronic energies as a function of the co-ordinates of the nuclei. This function can then be used as a potential in a time independent Schrödinger equation, $\psi_{nuclear}$, that contains only the nuclei.

2.1.3 Hartree and Hartree-Fock calculations

The Hartree-Fock methodology is a self-consistent iterative procedure to calculate the solution to the time-independent Schrödinger equation. The Hartree-Fock method is a reformulation of the Hartree method. The Hartree-Fock method makes a series of simplifications, the most significant being that the wave functions are assumed to be anti-symmetrised linear combinations of products of one-electron wave functions. The effects of electron correlation are completely ignored and the exchange energy resulting from the anti-symmetrisation of the wave function is treated exactly. The charge density, $\rho(\mathbf{r})$, is given in Equation 2.3, where ψ_i is the one-electron wave function.

$$\rho(\mathbf{r}) = \sum_i \psi_i^*(\mathbf{r})\psi_i(\mathbf{r}) \tag{2.3}$$

The Hartree-Fock equation is given in Equation 2.4. In this equation the electron-ion potential is represented by V_{e-ion}, and the exchange potential is

represented by V_X. The wave function and eigenvalues of the electronic state i are represented by ψ_i and ϵ_i respectively.

$$\left[-\frac{\hbar^2}{2m}\nabla_i^2 + V_{e-ion} + V_H + V_X\right]\psi_i = \epsilon_i\psi_i \tag{2.4}$$

Planck's constant is $\hbar$, while the Laplacian, ∇_i, represents the kinetic energy term. The remaining term is the Hartree potential, V_H, which is evaluated using:

$$V_H[\rho] = e^2 \int \frac{\rho(\mathbf{r}')}{\mid \mathbf{r} - \mathbf{r}' \mid} d\mathbf{r}' \tag{2.5}$$

The Hartree-Fock total-energy functional, E_{HF}, can then evaluated using:

$$E_{HF} = \sum_i \epsilon_i - \frac{1}{2}\int V_H[\rho]\rho(\mathbf{r})d^3\mathbf{r} - \frac{1}{2}\sum_i \psi_i^*(\mathbf{r})V_X\psi_i(\mathbf{r})d^3\mathbf{r} \tag{2.6}$$

The Hartree-Fock method has its limitations, namely that the evaluation of the exact exchange part can scale linearly or up to N^4 (where N is the number of electrons in the system), which is the reason why further methods, such as density functional theory have been developed.

2.1.4 Density functional theory

Density Functional Theory (DFT) [26] is an approach for the description of the ground state[2] properties of metals, semiconductors and insulators. It differs from the more classical methods such as Hartree-Fock theory, in that the main concept of DFT is to describe an interacting system of atoms via its density, rather than their many-body wave function. The density is simpler to deal with, compared to the many-body wave form, both in conceptual terms and practically. In fact this shift in approach means that for a system of N electrons in a solid, which obey the Pauli principle[3] and repulse each other via the Coulomb potential, the

[2]The ground state of a system is the lowest energy state for that system. Any state with an energy greater than the ground state is said to be an excited state.

[3]The Pauli exclusion principle states that no two identical fermions may occupy the same quantum state simultaneously.

basic system relies only on the three spatial co-ordinates (x, y, and z), instead of the 3N degrees of freedom for a system described via its many-body wave function.

In principle DFT gives a good description of ground state properties. The practical applications of DFT are based on approximations for the exchange-correlation potential. The exchange-correlation potential describes the effects of the Pauli principle and the coulomb potential beyond a pure electrostatic interaction of the electrons. It is not possible to solve the many-body problem exactly for solids, so it is not feasible to possess the exact exchange-correlation potential.

DFT relies on the Hohenberg-Kohn (HK) theorem [27], which established the existence of a one-to-one mapping between ground state electron density and the ground state many-body wave function. Additionally the HK theorem proves that the total electronic energy of the system is minimised by the ground state density. However, it should be noted that the HK theorem only holds for the ground state, and furthermore that while the one-to-one mapping does exist, no exact mapping is provided.

The HK theorem is summarized as follows:

i) The energy functional, $E[\rho]$, will be equal to the ground state energy functional, $E[\rho_0]$ (ρ_0 determines all ground state properties of the system), only if the system charge density, ρ, is equal to the ground state charge density, ρ_0.

ii) There exists a variational principle for the above energy density functional, E[ρ]. Namely if ρ is not the ground state density of the above system then, $E[\rho] > E[\rho_0]$.

These lead to the equation:

$$E[\rho] \geq E[\rho_0] \tag{2.7}$$

Now E[$\rho(\mathbf{r})$] can be split up as shown below:

$$E[\rho(\mathbf{r})] \equiv T(\rho) + \int \{V_{ext}(\mathbf{r}) + \frac{1}{2}V_H[\rho]\}\rho(\mathbf{r})d\mathbf{r} + E_{xc}[\rho(\mathbf{r})] \tag{2.8}$$

Where $T(\rho)$ is the kinetic energy of a system of independent particles with density $\rho(\mathbf{r})$ and V_{ext} is the external potential. In principle all parts of the above equation are known except the exchange-correlation functional, $E_{xc}[\rho(\mathbf{r})]$.

2.1.5 The Kohn-Sham energy functional

Kohn and Sham [26] showed that it is possible to replace the many-electron problem with a set of exactly equivalent self-consistent one-electron equations. The Kohn-Sham total-energy functional for a set of doubly occupied electronic states ψ_i can be written as follows:

$$\begin{aligned} E[\{\psi_i\}] = 2\sum_i \int \psi_i^* \left(-\frac{\hbar^2}{2m}\right) \nabla^2\psi_i d\mathbf{r} + \\ \int V_{e-ion}(r)\rho(\mathbf{r})d\mathbf{r} + \frac{e^2}{2}\int \frac{\rho(r)\rho(r')}{\mid r - r' \mid} d\mathbf{r}d\mathbf{r}' \\ + E_{xc}[\rho(\mathbf{r})] + E_{ion}[\{R_I\}] \end{aligned} \tag{2.9}$$

where E_{ion} is the Coulomb energy associated with interactions among ions at positions $\{R_I\}$, V_{e-ion} is the static total electron-ion potential, $E_{xc}[\rho(\mathbf{r})]$ is the exchange-correlation functional. The electronic density, $\rho(\mathbf{r})$, is evaluated as shown in Equation 2.10:

$$\rho(\mathbf{r}) = 2\sum_i \mid \psi_i(\mathbf{r}) \mid^2 \tag{2.10}$$

2.1.6 The Kohn-Sham equations

The ground state energy of the system of electrons with ions in positions $\{R_I\}$, which is what is required, is equal to the minimum of the Kohn-Sham energy functional. So the set of wave functions, ψ_i, that minimise the Kohn-Sham energy functional need to be found. They are given by the self-consistent solutions

to the Kohn-Sham equations [26]. The charge density, $\rho(\mathbf{r})$, can be written in terms of some trial single particle wave function, $\psi(\mathbf{r})$, as shown in Equation 2.11. This leads to the Kohn-Sham equation, which is given in Equation 2.12.

$$\rho(\mathbf{r}) = \sum_i \mid \psi_i(\mathbf{r}) \mid^2 \tag{2.11}$$

$$\left[-\frac{\hbar^2}{2m}\nabla^2 + V_{KS}(\mathbf{r})\right]\psi_i(\mathbf{r}) = \epsilon_i\psi_i(\mathbf{r}) \tag{2.12}$$

Where ψ_i is the wave function of electronic state i, and ϵ_i is the Kohn-Sham eigenvalue. The Kohn-Sham potential, V_{KS}, is then given as follows:

$$V_{KS} \equiv V_{KS}[\rho(\mathbf{r})] = V_{e-ion}(\mathbf{r}) + V_H[\rho(\mathbf{r})] + V_{xc}[\rho(\mathbf{r})] \tag{2.13}$$

Where the Hartree potential, V_H, is the classical Coulomb potential due to the electrons, and is given in Equation 2.14. The exchange-correlation potential, V_{xc}, is evaluated as shown in Equation 2.15.

$$V_H[\rho] = e^2 \int \frac{\rho(\mathbf{r}')}{\mid \mathbf{r} - \mathbf{r}' \mid} d^3\mathbf{r}' \tag{2.14}$$

$$V_{xc}[\rho] = \frac{\delta E_{xc}[\rho]}{\delta\rho} \tag{2.15}$$

2.1.7 Exchange-correlation functionals

The most common approximation to the exchange-correlation potential, is the local density approximation (LDA) [26]. This locally substitutes the exchange-correlation energy density of an inhomogeneous system with that of an electron gas evaluated at the local density. Since the exact value of $E_{xc}[\rho(\mathbf{r})]$ is unknown, an approximation to its value is required. This is achieved by first performing exact many-electron calculations on a system of interacting electrons with constant ρ; this system is commonly known as Jellium. The exchange-correlation density in the system, $e_{xc}(\rho)$, is then calculated. Using the LDA, the $E_{xc}[\rho(\mathbf{r})]$ can be expressed as follows:

$$E_{xc}^{LDA}[\rho(\mathbf{r})] = \int \rho(\mathbf{r}) e_{xc}(\rho) d\mathbf{r}. \tag{2.16}$$

The LDA works by dividing space into small elements and assuming that the exchange-correlation contribution in each small element is the same as for the Jellium system with the same ρ.

While many ground state properties such as the lattice constant and bulk moduli are adequately approximated by LDA, the dielectric constant is overestimated by between 10-40% with the LDA. Also if the density undergoes rapid changes, then the the LDA will fail since it approximates the energy of the true density by the energy of a local constant density. This can be avoided by considering the gradient of the electron density, by using the generalised gradient approximation (GGA) [28]. The GGA for the exchange-correlation functional is given in Equation 2.17.

$$E_{xc} = E_{xc}[\rho(\mathbf{r}), \nabla\rho(\mathbf{r})]. \tag{2.17}$$

By utilising the GGA there can be a significant improvement over results calculated using the LDA. However, as with the LDA, there are several different parameterisations of the GGA. Some of these are semi-empirical, in that experimental data (for example atomisation energies) is used in their derivation, while others are found entirely from first principles. Within our calculations (see Section 2.2), we have used the Perdew-Burke-Ernzerhof (PBE) parameterisation [29] of the GGA functional.

2.1.8 Modelling periodic systems

When mapping the many-body problem effectively into a single particle problem, there is still the issue of coping with the infinite number of non-interacting electrons moving in the static potential of an infinite number of ions. This issue can be split up into two problems to overcome:

i) For each of the infinite number of electrons in the system a wave function must be calculated.

ii) Each electronic wave function extends over the entire solid, thus the basis sets, which are required to expand over each wave function, are infinite.

The issues can be resolved by performing the calculations on periodic systems and by applying Bloch's theorem to the electronic wave functions.

Bloch's theorem

By using Bloch's theorem, the electronic wave function can be written as a product of a cell-periodic part and a wave-like part. The electronic wave function, $\psi_n(\mathbf{r})$, is expressed as follows:

$$\psi_n(\mathbf{r}) = e^{i\mathbf{k}.\mathbf{r}} f_n(\mathbf{r}) \tag{2.18}$$

Where the cell-periodic part is represented by the $f_n(\mathbf{r})$ term, and a wave-like part is represented by the $e^{i\mathbf{k}.\mathbf{r}}$ term.

When studying a perfect infinite solid, Bloch's theorem turns an integral over all space into an integral over a finite volume of space (the first Brillouin zone[4]). This integration over the first Brillouin zone can be approximated by a summation of k-points with appropriate weights.

2.1.9 Supercell geometry

Bloch's theorem can be applied to an infinite system, but only if we have a periodic system. The extent to which Bloch's theorem simplifies the calculation

[4]For the propagation of a wave through a crystal lattice, the frequency is a periodic function of wave vector $\mathbf{k}$. In order to simplify the treatment of wave motion in a crystal, a zone in $\mathbf{k}$-space is defined. This zone forms the fundamental periodic region, such that the frequency or energy for a $\mathbf{k}$ outside this region may be determined from one of those within it. This region is known as the first Brillouin zone.

is colossal, so even though the supercell which we use is not truly a periodic system, we continue to use Bloch's theorem. Furthermore, if you wanted to calculate the energy of an isolated defect in the supercell, in terms of practical solutions, there are only really two, *i.e.* creating the defect at the centre of a large cluster, or the use of periodic repeats of the defect. We use the concept of periodic repeats of the defect being studied within our work. The supercell for a point defect, in this case vacancy, is shown schematically in Figure 2.1.

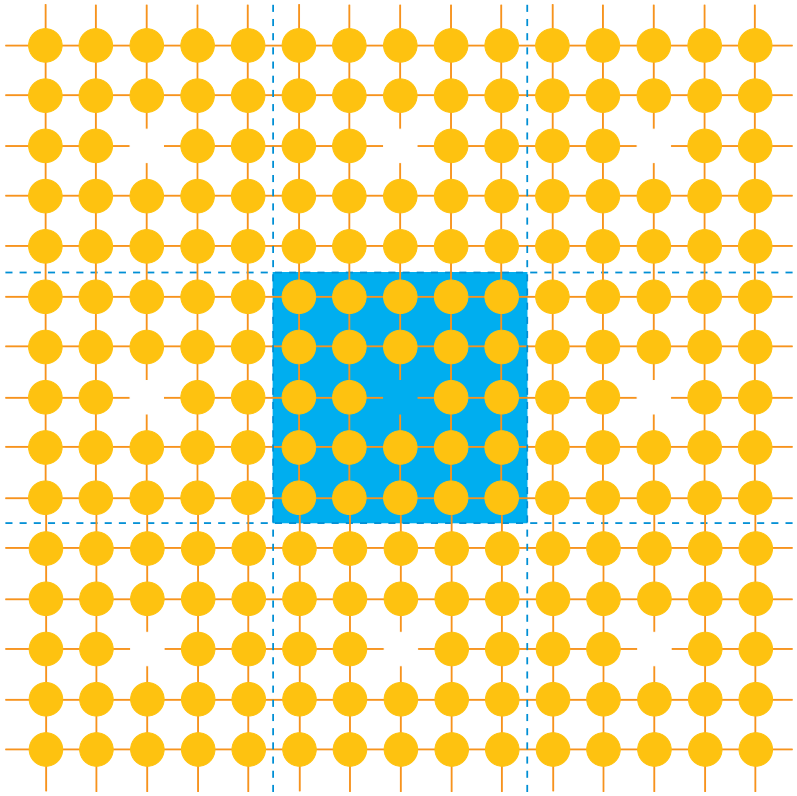

Figure 2.1: A simplified diagram showing the periodic geometry of a supercell. The shaded region in the centre represents the supercell, and the periodic repeats are the regions between the dashed lines. A vacancy has been introduced to the centre of the unit cell in order to illustrate the concept of repeated defects.

In order to reproduce the supercells, periodic boundary conditions are applied to the supercell. This means that the defect is repeated throughout the space. The supercell must have enough bulk solid within it in order to prevent defects in neighbouring cells interacting with each other. The level of interac-

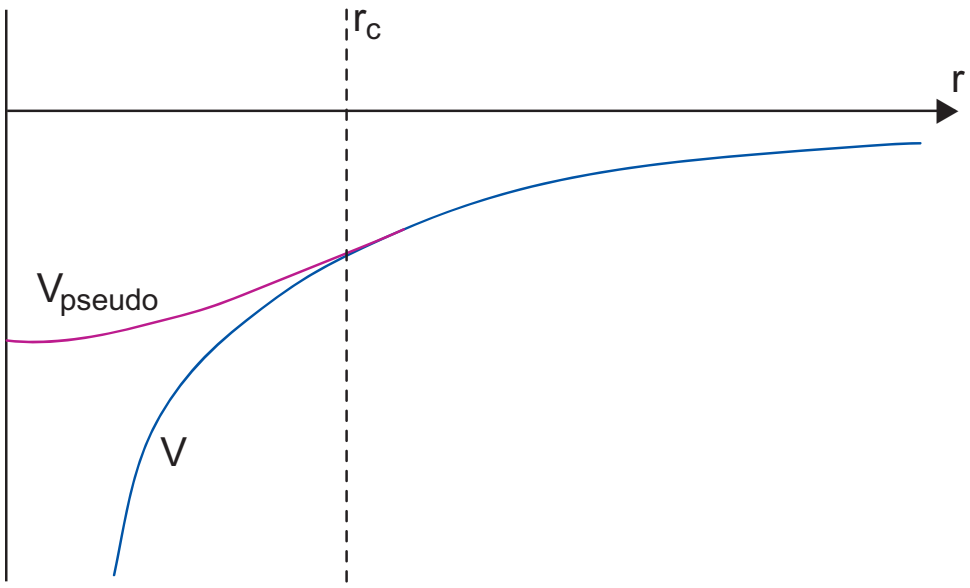

Figure 2.2: Schematic showing the relationship between a potential, V, and a corresponding pseudopotential, V_{pseudo}, either side of the cutoff radius, r_c.

tion between defects can be checked by increasing the volume of the supercell, in other words, adding more bulk solid around the defect. When the defect energy converges in the system then the system size is sufficient.

2.1.10 Pseudopotentials

The purpose of pseudopotentials is to attempt to replace the complex effects of the core electrons of an atom and its nucleus with a pseudopotential. This is done so that instead of the Coulombic potential term that is usually found in the Schrödinger equation, this is replaced with a modified potential term.

The reasoning behind replacing the core electrons is because it is a well established fact that most physical properties of solids are dependent on the valence electrons to a much greater degree than that of the tightly bound core electrons. In practice the core electrons and the strong nuclear potential are removed and a weaker pseudopotential is substituted in there place. This pseudopotential acts on a set of pseudo-wave functions instead of the true valence wave functions.

As can be seen in Figure 2.2, the potential is very steep (strong) within

the cutoff radius, r_c, which would lead to computational difficulties. For that reason the pseudopotential replaces this with a much simpler and weaker potential. Outside of the cutoff radius, the pseudopotential has been generated to be identical to the potential.

There are several methods of generating pseudopotentials. Pseudopotentials are not unique, but they must obey certain criteria. The core charge produced must be the same for both pseudo and atomic wave functions. This ensures that the pseudo-atom produces the same scattering properties as the ionic core. The pseudo-electron eigenvalues must be the same as the valence eigenvalues obtained from the atomic wave functions. Excited states may also be included (if appropriate), on inversion of the all electron Schrödinger equation for the atom.

Within our work we have used pseudopotentials of the type developed by Hartswigen, Goedecker and Hutter (HGH) [30]. The local part of the HGH pseudopotential is given in Equation 2.19 where the term erf represents the error function, and Z_{ion} is the total charge minus the charge contribution from the valence electrons:

$$\begin{aligned} V_{loc}(r) &= \frac{-Z_{ion}}{r}\,\mathrm{erf}\left(\frac{r}{\sqrt{2}r_{loc}}\right) + \exp\left[-\frac{1}{2}\left(\frac{r}{r_{loc}}\right)^2\right] \times \\ &\quad \left[C_1 + C_2\left(\frac{r}{r_{loc}}\right)^2 + C_3\left(\frac{r}{r_{loc}}\right)^4 + C_4\left(\frac{r}{r_{loc}}\right)^6\right] \end{aligned} \tag{2.19}$$

The C_n parameters are determined by minimising the differences between the eigenvalues and the charges within an atomic sphere for an all electron atom and a pseudo-atom. Within the local part of the pseudopotential, the same potential is used for all the angular momentum components of the wave function.

The non-local part of the HGH pseudopotential is given in Equation 2.20.

$$V_l(\mathbf{r},\mathbf{r}') = \sum_{i=1}^{3}\sum_{j=1}^{3}\sum_{m=-l}^{+l} Y_{l,m}(\mathbf{r}) p_i^l(r) h_{i,j}^l p_i^l(r') Y_{l,m}^*(\mathbf{r}') \tag{2.20}$$

The $Y_{l,m}$ terms are the spherical harmonics, where l is the angular momentum quantum number and m is the magnetic quantum number. The $p_i^l(r)$ terms are Gaussian type projectors. The non-local contribution to the psuedopotential is included in order to recover the correct scattering properties from the core.

2.1.11 Basis sets

A basis set is a set of functions that can be used to describe the wave functions of the electrons with the system being modelled. There are many implementations of DFT that use basis sets composed of plane waves. The plane wave basis sets have their advantages, such as they offer a stable and straightforward approach to obtaining complete convergence, and the atomic forces can be obtained with little additional computational effort. They, however, also possess significant disadvantages, primarily plane wave basis sets are wasteful of both computational time and memory, making them a poor choice for large systems [18]. Plane wave basis sets also fail to cope adequately with systems that contain a large amount of vacuum space. This vacuum is necessary to model systems such as our own accurately.

These limitations can be overcome by moving to a real-space localised basis set, which in our case means numerical, fixed energy, atomic-type orbitals. These have been shown to provide a good balance between speed and accuracy, especially when considering the larger unit cells. In order to generate the set of orbitals, a self-consistent spherical atomic calculation is performed, with the orbitals being forced to go to zero at a finite radius. This is equivalent to confining the atom within an infinite spherical square-well potential. The orbitals that comprise our basis sets have been smoothed in order to guarantee that the first and second derivatives are zero at the cutoff radius, r_c, of the orbital. This smoothing is performed by explicitly multiplying the orbitals by the smoothing function (see Equation 2.21).

$$S(r) = 1 - \exp\left[\frac{-(r - r_c)^2}{2\sigma^2}\right] \tag{2.21}$$

The values for the smoothing distance, σ, and the cutoff radius, r_c, can be determined by the comparison of differing values in order to find the optimum values for each atom type to be represented.

The complexity (and overall size) of the basis set that is used can vary greatly. The simplest type of basis set include only the minimal basis functions required to model the electrons on the atom species in question. This minimal basis set only consists of functions from the neutral atom. In nearly all cases though the minimal basis set is nowhere near complete enough in order to accurately model an atom in a molecule or solid. In order to increase the level of completeness of the basis set, further basis functions are added from charged atoms. A step up from the minimal basis set is a double numeric basis set with single polarisation (denoted as DNP). For the case of silicon our DNP basis set consists of 13 basis functions (s, p, $s*$, $p*$ and $d*$, where the $*$ denotes that the orbitals are from the 2+ charged state in this case). Previous to this work the most complete basis set that could be used within the code we use for our calculations (see Section 2.2), was the triple numeric with double polarisation (denoted as TNDP). For the case of silicon our TDNP basis set consists of 22 basis functions (s, p, $s*$, $p*$, $d*$, $s**$, $p**$ and $d**$, where the number of $*$'s denotes which charged state the orbital is from, the $**$ represents the 4+ charged state in this case). The most complete level of basis set that we use in this work is for nitrogen. This uses the triple numeric with double polarisation plus f-orbitals (denoted as TNDP+F). This basis set consists of 29 basis functions (s, p, $s*$, $p*$, $d*$, $s**$, $p**$, $d**$ and $f**$, where the $*$ and $**$ orbitals are from the 3+ and 5+ charged states respectively).

2.1.12 Binding energies

The most significant measure of system energies that we shall use throughout this work is the binding energy. The binding energy can be used when the interest is in combining two separate systems, for example the adsorption of a molecule (denoted as system A) to a surface (denoted as system B). Equation 2.22 demonstrates how to calculate the binding energy for a combined system of this type.

$$E_{\text{binding}} = E_{\text{combined system of A and B}} - E_{\text{A in isolation}} - E_{\text{B in isolation}} \tag{2.22}$$

The binding energy provides a measure of the required energy in order to separate the combined system into its isolated masses. Since energy would be required in order to separate the two masses, the sign of the binding energy is negative (if binding has taken place that is). When calculating binding energies for systems that atoms in close proximity of one another, overlap can occur between the basis functions on each atom and care must be taken not to introduce the basis set superposition error (BSSE)[5]. It has been shown [17] that by using basis sets of the TNDP level of completeness, it is possible to eliminate the BSSE, without the need to correct the results via an additional method, for example the Boys and Bernardi counterpoise method [31].

2.2 PLATO

All the calculations performed within this research have been performed using the PLATO (Package for Linear combination of Atomic Type Orbitals) software suite. PLATO was developed by Steven Kenny and Andrew Horsfield, and

[5]When performing calculations where atoms are close to one another, if the basis functions on the atoms are different (as is the case with atoms of different species) then this can lead to the different wave functions being expanded within each other, which leads to inconsistencies and artificially deep energy minima.

it implements DFT as the framework in order to solve the time-independent Schrödinger equation. PLATO uses a localised basis set which, as mentioned previously, takes advantage of our physical understanding of the calculation in order to minimise the computational cost of the calculations. This method maintains a high level of the quality and transferability of a plane wave basis set, but at a significantly reduced cost. However, this is system dependent as for some systems plane waves are more efficient, for example, close packed metal systems.

PLATO is used to evaluate the total energy of a system, E_{total}, given in Equation 2.23. The first term in Equation 2.23 is the single particle energy, the next three terms represent the double counting energy and the final term is the interaction between the ions.

$$\begin{aligned} E_{total} &= \sum_i f_i \epsilon_i - \frac{1}{2}\int V_H[\rho]\rho(\mathbf{r})d\mathbf{r} + E_{xc}[\rho(\mathbf{r})] - \\ &\int V_{xc}[\rho]\rho(\mathbf{r})d\mathbf{r} + \frac{1}{2}\sum_{I\neq J}\frac{Z_I Z_J}{|\mathbf{R}_I - \mathbf{R}_J|} \end{aligned} \tag{2.23}$$

The ϵ_i's in Equation 2.23 represent the eigenvalues of the Hamiltonian (given in Equation 2.24), and the f_i term represents the occupancy of the state i. The $\mathbf{R}_I$ and $\mathbf{R}_J$ terms represent the position vectors of atoms I and J respectively. In Equation 2.24 the kinetic energy operator is represented by the $\hat{T}$, and as previously stated, V_{e-ion}, represents the electron-ion potential which describes the potential between the electrons and nucleus. The Hartree potential, $V_H[\rho]$, is given in Equation 2.25, and the exchange-correlation potential, $V_{xc}[\rho]$, is given in Equation 2.26.

$$\hat{H} = \hat{T} + V_{e-Ion}(\mathbf{r}, \mathbf{r}') + V_H[\rho] + V_{xc}[\rho] \tag{2.24}$$

$$V_H[\rho] = \int \frac{\rho(\mathbf{r}')}{|\mathbf{r} - \mathbf{r}'|} d\mathbf{r}' \tag{2.25}$$

$$V_{xc}[\rho] = \frac{\delta E_{xc}[\rho(\mathbf{r})]}{\delta \rho} \tag{2.26}$$

Eigenstates, $|\psi_i\rangle$, are found by expanding in linear combinations of atomic like basis functions, $|\phi_{I\alpha}\rangle$, giving rise to Equation 2.27. The I and α terms correspond to the site and orbtial indices respectively.

$$|\psi_i\rangle = \sum_{I\alpha} C_{I\alpha}^{(i)} |\phi_{I\alpha}\rangle \tag{2.27}$$

By using Equation 2.27, we are able to reformulate the Schrödinger equation (see Equation 2.28) in to the form given in Equation 2.29.

$$\hat{H}|\psi_i\rangle = \epsilon_i |\psi_i\rangle \tag{2.28}$$

$$\sum_{I\alpha} C_{I\alpha}^{(i)} \hat{H} |\phi_{I\alpha}\rangle = \epsilon_i \sum_{I\alpha} C_{I\alpha}^{(i)} |\phi_{I\alpha}\rangle \tag{2.29}$$

We can move from Equation 2.29 to Equation 2.30, by multiplying both the left and right hand sides by $\phi_{J\beta}$ and integrating over all space, which leads to the formulation of the generalised eigenvalue problem. We can now define the overlap matrix elements (see Equation 2.30) and Hamiltonian matix elements (see Equation 2.31), accordingly.

$$S_{I\alpha,J\beta} = \int \phi_{I\alpha}(\mathbf{r}) \phi_{J\beta}(\mathbf{r}) d\mathbf{r} \tag{2.30}$$

$$\begin{aligned} H_{I\alpha,J\beta} \;=\; & \int \phi_{I\alpha}(\mathbf{r}) \hat{T} \phi_{J\beta}(\mathbf{r}) d\mathbf{r} + \\ & \int\int \phi_{I\alpha}(\mathbf{r}) V_{e-Ion}(\mathbf{r}, \mathbf{r}') \phi_{J\beta}(\mathbf{r}') d\mathbf{r} d\mathbf{r}' + \\ & \int \phi_{I\alpha}(\mathbf{r}) V_H[\rho(\mathbf{r})] \phi_{J\beta}(\mathbf{r}) d\mathbf{r} + \\ & \int \phi_{I\alpha}(\mathbf{r}) V_{xc}[\rho(\mathbf{r})] \phi_{J\beta}(\mathbf{r}) d\mathbf{r} \end{aligned} \tag{2.31}$$

If we look at the individual components of 2.31, then they can be dealt with as follows:

i) The first integral is the kinetic energy integral, and is composed purely of one and two centre integrals, which can be entirely treated using the Slater-Koster integrals [19]. These integrals are performed and stored as tables before PLATO is run. These two-centre integral tables are one dimensional, which means that the evaluation and computational speed of these tables is very fast compared to repeated "on the fly" calculations. These integral tables are based on rotations that are performed using the Slater-Koster tables. By using the Slater-Koster tables it is possible to represent any integral using only linear combinations of a set of fundamental integrals. This means that only the fundamental integrals need to be stored in the integral tables. The list of fundamental Slater-Koster integrals for orbitals, up to and including f-orbitals is given in Table 2.1. Further discussion on the implementation of the Slater-Koster routines within PLATO can be found in Chapter 3, where we discuss the alterations and additions made to PLATO, in order to accommodate f-orbitals and orbitals with greater angular momentum quantum numbers (l). Integral tables are created for overlap terms, the hopping terms, the local and non-local parts of the pseudopotential.

	s	p	d	f
s	$ss\sigma$	$sp\sigma$	$sd\sigma$	$sf\sigma$
p		$pp\sigma$, $pp\pi$	$pd\sigma$, $pd\pi$	$pf\sigma$, $pf\pi$
d			$dd\sigma$, $dd\pi$, $dd\delta$	$df\sigma$, $df\pi$, $df\delta$
f				$ff\sigma$, $ff\pi$, $ff\delta$, $ff\phi$

Table 2.1: The list of fundamental Slater-Koster integrals for orbitals with angular momentum quantum numbers, $l \leq 3$. The angular momentum, m, of each integral is denoted by either σ ($m = 0$), π ($m = \pm 1$), δ ($m = \pm 2$) or ϕ ($m = \pm 3$).

ii) The second (double) integral is the electron-ion integral. This is split up into local and non-local parts. The local part is added to the Hartree potential due to the neutral atom, this makes a short range potential with one and two centre parts (which are treated as above), the three centre part, however, is treated separately using a mesh as discussed in the subsequent steps. The non-local part can be treated at either a one centre, a two centre or a product of two centre integrals (all can be treated as outlined previously).

iii) The third integral, deals with the Hartree potential. In the second integral we dealt with the Hartree potential due to the neutral atom density, so all that remains to be dealt with is the Hartree potential due to the change in density on bonding, $V_H[\Delta\rho(\mathbf{r})]$. This is dealt with by using a mesh to perform integrals, and is calculated differently depending on the choice of mesh. The choices for the mesh within PLATO are an atom centred grid, or a uniform mesh. For the purpose of this research we have used the uniform mesh, as it is easy to solve Poisson's equation for the uniform mesh. For the uniform mesh you first compute $\Delta\rho(\mathbf{r})$ at each of the grid points in real space. Then we solved Poisson's equation to calculate $V_H[\Delta\rho(\mathbf{r})]$ via the method of Fast Fourier Transforms (FFT).

iv) The fourth integral is the exchange-correlation integral, and is dealt with in part by implementing one of the exchange-correlation functionals discussed in Sub-Section 2.1.7, and then a mesh is used to perform the required integrals. Unlike the calculation of $V_H[\Delta\rho(\mathbf{r})]$, the calculation of V_{xc} (and the neutral atom potential) is independent of the type of mesh used.

This means that the problem of finding the eigenstates is reduced to solving the generalised eigenvalue problem (see Equation 2.32).

$$\sum_{J\beta} H_{I\alpha,J\beta} C^{(i)}_{J\beta} = \epsilon_i \sum_{J\beta} S_{I\alpha,J\beta} C^{(i)}_{J\beta} \tag{2.32}$$

The basic flow of a relaxation calculation with PLATO is given in Figure 2.3. In essence the program consists of two loops, one nested within the other, where the inner loop is for the electronic convergence of the system. The inner loop is a self-consistent loop that runs until the difference between the densities of the current and previous iterations (defined as dRho within PLATO), is lower than the user defined tolerance (the variable ResidueTol within PLATO). The user sets ResidueTol to a value that assures that the self-consistent cycle reaches convergence. In practise often the user will start the calculation with a higher value for ResidueTol, which is then reduced over the course of the simulation.

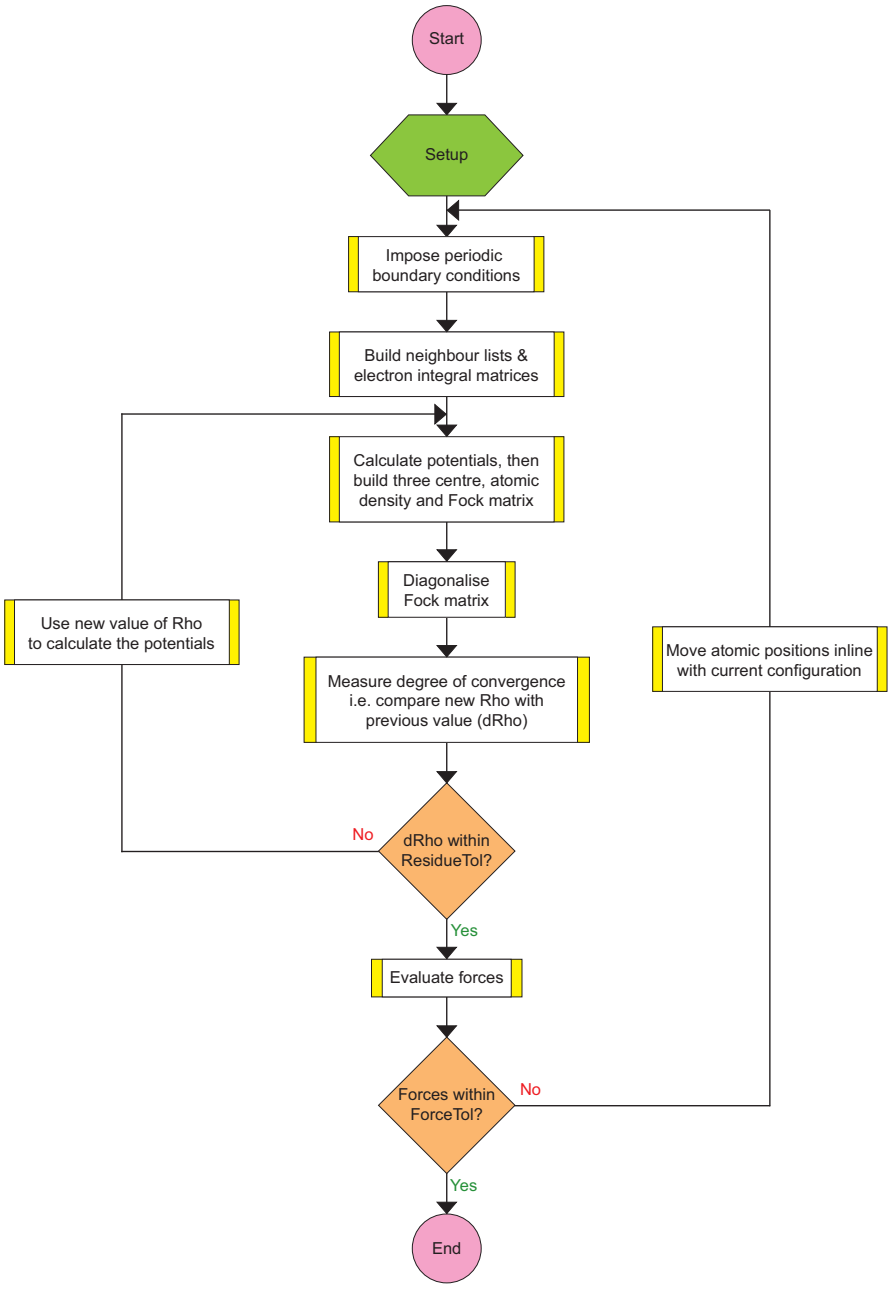

Figure 2.3: A flow chart that demonstrates a simplified routine for a relaxation performed within PLATO.

The second loop is concerned with the amount of force within the system. At the end of every self-consistent cycle the force in the system is calculated. This is then compared to the user set threshold (the variable ForceTol within PLATO) for the required level of convergence. If the system has a force greater than the

value for ForceTol, then the self-consistent loop will be started again, using the new atomic positions generated from the previous electronic convergence loop.

It is worth noting that all the calculations within PLATO revolve around the system density (it is after all a program that implements DFT). The program initially calculates the potentials, then diagonalises the Hamiltonian, and calculates the respective eigenvalues and eigenvectors. These eigenvalues and eigenvectors are then used to create the new density, which is then compared with the previous density at the end of the electronic convergence loop. Again this new density is used to generate the new potentials if the systems forces are not within the force tolerance at the end of the force convergence loop.

2.3 Bader analysis

To analyse the bonding and the charge transfer in the systems, we have used the algorithm devised by Sanville *et al.* [32], that implements Bader's principles from his atoms in molecules work [33]. Bader's approach characterises the chemical bonding of a system based on the topology of the quantum charge density, and it also allows for the calculation of specific physical properties for individual atoms. This allows a thorough analysis of some of the aspects of our calculations.

2.3.1 Bonding analysis

The method works by examining a pair of atoms, first finding the midpoint between the atoms and then calculating the Hessian of the electron density and the gradient at this point. Atoms that are chemically bonded are characterised by a saddle point in the electron density, so they possess one positive and two negative eigenvalues. The method then iteratively searches to find the minimum along the positive eigenvector, and the maxima along the two negative eigenvectors, until the gradient is zero. This method is then repeated for the entire system, in order to find all of these critical bonding points. Within Bader's principles, the presence of a bonding interaction is only signified by these critical

points.

The two negative eigenvalues describe the curvature of the bond perpendicular to the direction of the bond, as the ratio of the two negative eigenvalues provides a measure of the bond's characteristic. In particular it indicates how much p characteristic the bond possesses, which corresponds to an elongation of the circular shape of the perfect single bond (see Figure 2.4). As a reference we use the single and double bonds found in ethane and ethene, which have bond ratios of 1.00 and 1.27 respectively. Bonds between pairs of carbon atoms, which have ratios between these two values would be considered as having some measure of interaction between the p-orbitals of the constituent atoms.

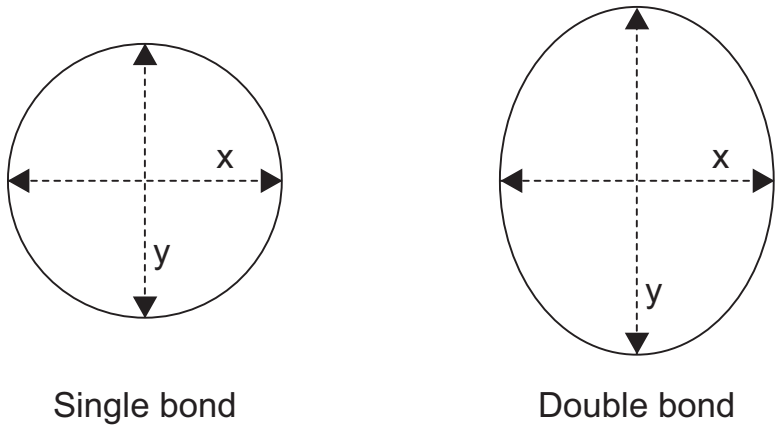

Figure 2.4: Schematic showing the how the difference in Bader bonding ratios affects the characteristic of the bond. As the ratio $\frac{y}{x}$ becomes greater than 1, the bond becomes more like a double bond than a single bond.

2.3.2 Charge analysis

Since atomic charge is not a quantum mechanical observable, we will use Bader charge analysis to determine the amount of charge on each atom in the system. This is achieved by splitting the cell into a group of subsystems, and calculating the charge contained within each subsystem. In most cases these subsystems, called Bader atoms, will contain one nucleus, however, some Bader atoms will not contain a nucleus. The volumes are defined by mapping out the surface of

zero charge density flux between Bader atoms. The surface of zero flux is defined in Equation 2.33, where $S(\mathbf{r_s})$ is the surface surrounding the Bader atom, and $\text{norm}(\mathbf{r_s})$ is a unit normal vector to that surface.

$$\nabla\rho(\mathbf{r_s}) \cdot \text{norm}(\mathbf{r_s}) = 0 \,\forall\, \mathbf{r_s} \,\text{on}\, S(\mathbf{r_s}) \tag{2.33}$$

Bader's method allows the charge on atoms to be calculated relatively independently of the basis set, for a given charge density, which is not the case with the often used Mulliken population analysis.

Chapter 3

Extension of orbital types within PLATO

3.1 Introduction

Previous work [18] has illustrated that the level of completeness of the basis set being used for a calculation can significantly affect the calculations overall accuracy. Previously within PLATO, it was possible to create basis sets that consisted of combinations of s, p and d-orbitals. This has proved to be more than sufficient for a large range of systems, however, for systems containing certain elements (for example nitrogen and iron) the results gained with basis sets only using s, p and d-orbitals were not good enough. For this reason it was decided that extending PLATO itself, in order to cope with not only f-orbitals but orbitals of even greater angular quantum numbers, would be the best course of action.

Within PLATO the overlaps between all orbitals and the interaction of the orbitals with some potentials are calculated using Slater-Koster integrals [19]. In this chapter we begin by exploring the principles behind Slater-Koster integrals, and then the methods implemented within PLATO for calculating these integrals. Previously PLATO implemented an analytic approach to calculating the Slater-Koster integrals, however a recursive approach was also investigated

and implemented (both of these methodologies are discussed in-depth). Furthermore, in line with creating a more flexible approach, we also changed how every part of PLATO (and the support program that we use to create basis set files) handled this new approach to the Slater-Koster integrals and their derivatives (which are required for the calculation of the interatomic forces between atoms). Implementing these flexible generic approaches within PLATO was a considerable task. While the recursive Slater-Koster routines required the majority of the actual computer code to be written, it was the generalisation of the remainder of PLATO (and its support program) that became the most complex and time consuming part of the whole issue.

3.2 Slater-Koster integrals

Before discussing the Slater-Koster integrals, we shall first introduce the concept of direction cosines; these are fundamental in the calculation of the Slater-Koster integrals. When defining a unit vector in Cartesian space, the unit vector's three scalar components can be referred to as direction cosines. The value of each component is equal to the cosine of the angle formed by the unit vector and its corresponding co-ordinate axis (as shown in Figure 3.1).

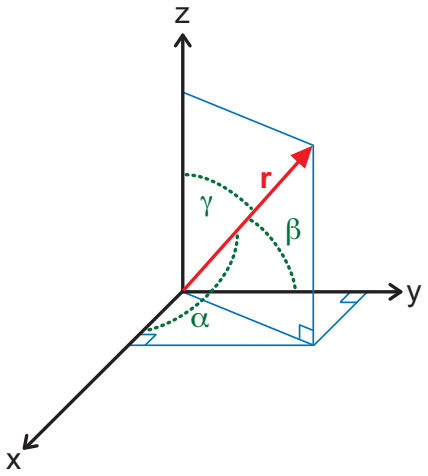

Figure 3.1: Schematic of the position vector, $\mathbf{r}$, and the angles α, β and γ, which are defined as the angles $\mathbf{r}$ makes with the x, y and z axes respectively.

In terms of the Slater-Koster integrals, these directional cosines are used to express the orientation of each of the component integrals. These direction cosines are defined as in Equations 3.1 through to 3.3.

$$l = \cos\alpha = \frac{x}{|\mathbf{r}|} \tag{3.1}$$

$$m = \cos\beta = \frac{y}{|\mathbf{r}|} \tag{3.2}$$

$$n = \cos\gamma = \frac{z}{|\mathbf{r}|} \tag{3.3}$$

Where the position vector, $\mathbf{r}$, is the vector between the two atoms (one at the origin, and the other one at position vector $\mathbf{r}$ from the origin) and is defined as:

$$\mathbf{r} = x\mathbf{i} + y\mathbf{j} + z\mathbf{k} \tag{3.4}$$

Within PLATO we use basis sets that consist of atomic-like orbitals. These orbitals consist of a radial function multiplied by a spherical harmonic. We then need to perform integrals which contain multiples of these functions. Slater-Koster rules take advantage of a certain degree of symmetry in order to write the integrals as a sum of one dimensional functions. The integrals depend on the vector, which is three dimensional, separating the two atoms, so this is quite an achievement. The spherical harmonic part is described as $Y_{l,m}$, where l is the quantum angular momentum index, and m is the quantum magnetic number. The atomic orbitals for a s-orbital (the spherical harmonic $Y_{0,0}$), and the three p-orbital states (corresponding to the spherical harmonics denoted by $Y_{1,-1}$, $Y_{1,0}$ and $Y_{1,1}$) are given in Figure 3.2.

As discussed in Chapter 2, in order to solve the generalised eigenvalue problem (see Equation 2.32), which is central to the operation of PLATO, the overlap and Hamiltonian matrix elements (given in Equations 2.30 and 2.31 respectively) must first be calculated. Both the overlap and Hamiltonian matrix elements consist of sums of integrals, for example the Hamiltonian matrix elements require

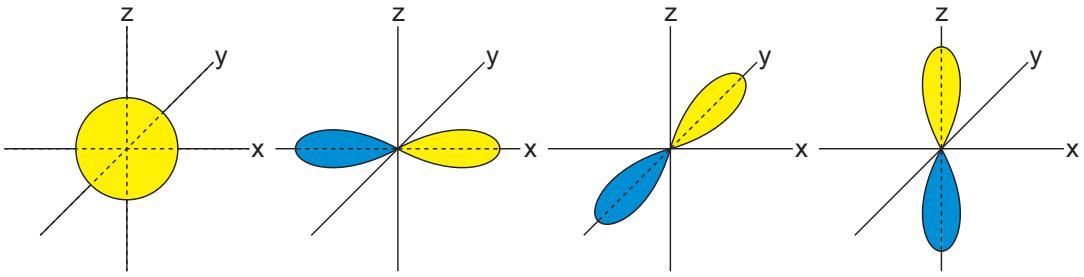

(a) s atomic orbital (b) p_x atomic orbital (c) p_y atomic orbital (d) p_z atomic orbital

Figure 3.2: Atomic orbitals for the orbital type s, and all three p states, p_x, p_y and p_z. These are only two dimensional representations while the orbitals are actually three dimensional (they are volumes). The yellow represents where the orbital's wave function is positive, and the blue represents where it is negative.

the calculation of the kinetic energy integral. As previously explained, evaluating the kinetic energy integral actually corresponds to using the Slater-Koster rules to solve a series of two atom configurations. The Slater-Koster rules describe the two atom configurations, as the spherical harmonics of each atom can be expressed as a combination of fundamental integrals and the radial parts can be expressed using directional cosines.

With two orbitals many of the possible integrals are zero, as the positive and negative contributions often cancel each other out. It is possible to express any integral in terms of only a few non-zero integrals; where the non-zero integrals are known as fundamental integrals. The fundamental integrals between s and p-orbitals are shown in Figure 3.3. The interaction between any arbitrary configuration of two orbitals can be expressed as a linear combination of directional cosines and the fundamental integrals. This is illustrated in Figure 3.4, which shows the interaction between a s-orbital and a p-orbital.

A comprehensive list of the Slater-Koster integrals for the s, p and d-orbitals is given in Table 3.1. There are no entries for the p-s, p-d and d-s combinations of orbitals as they are similar; actually they are equivalent if the signs for the Slater-Koster integrals are ignored, to the s-p, d-p and s-d combinations respec-

tively (as it does not matter which orbital is on which atom). From looking at Table 3.1 it is clear that as the bond vector between the two atoms varies, so does the contribution from each of the corresponding fundamental integrals.

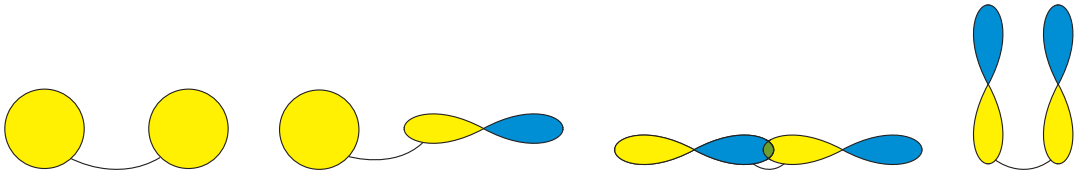

(a) $V_{ss\sigma}$ (b) $V_{sp\sigma}$ (c) $V_{pp\sigma}$ (d) $V_{pp\pi}$

Figure 3.3: The fundamental integrals between s and p-orbitals. The colouring scheme is the same as in Figure 3.2. If there is no angular momentum, $m = 0$, about the bond axis for the integral between two states it is denoted by σ, and for $m = \pm 1$ a π is used. For d and f-orbitals there are values of $m = \pm 2$ (for d-orbitals) and $m = \pm 3$ (for f-orbitals), which are labeled δ and ϕ respectively.

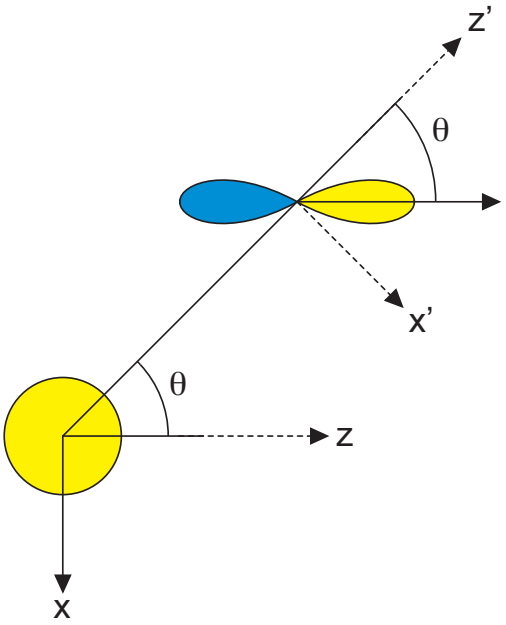

Figure 3.4: The interaction between a s-orbital on an atom at the origin, and a p_z-orbital on an atom where the bond axis is at an angle θ to the z-axis. As such this interaction can be represented by the integral, $\cos\theta\, V_{sp\sigma}$.

α	β	Slater-Koster integral
s	s	$V_{ss\sigma}$
s	p_x	$lV_{sp\sigma}$
s	p_y	$mV_{sp\sigma}$
s	p_z	$nV_{sp\sigma}$
p_x	p_x	$l^2V_{pp\sigma} + (1-l^2)V_{pp\pi}$
p_y	p_y	$m^2V_{pp\sigma} + (1-m^2)V_{pp\pi}$
p_z	p_z	$n^2V_{pp\sigma} + (1-n^2)V_{pp\pi}$
p_x	p_y	$lmV_{pp\sigma} - lmV_{pp\pi}$
p_x	p_z	$lnV_{pp\sigma} - lnV_{pp\pi}$
p_y	p_z	$mnV_{pp\sigma} - mnV_{pp\pi}$
s	d_{xy}	$\sqrt{3}lmV_{sd\sigma}$
s	d_{yz}	$\sqrt{3}mnV_{sd\sigma}$
s	$d_{3z^2-r^2}$	$[n^2 - \frac{1}{2}(l^2+m^2)]V_{sd\sigma}$
s	d_{zx}	$\sqrt{3}lnV_{sd\sigma}$
s	$d_{x^2-y^2}$	$\frac{1}{2}\sqrt{3}(l^2-m^2)V_{sd\sigma}$
d_{xy}	p_y	$\sqrt{3}lm^2V_{pd\sigma} + l(1-2m^2)V_{pd\pi}$
d_{yz}	p_y	$\sqrt{3}m^2nV_{pd\sigma} + n(1-2m^2)V_{pd\pi}$
$d_{3z^2-r^2}$	p_y	$m[n^2 - \frac{1}{2}(l^2+m^2)]V_{pd\sigma} - \sqrt{3}mn^2V_{pd\pi}$
d_{zx}	p_y	$\sqrt{3}lmnV_{pd\sigma} - 2lmnV_{pd\pi}$
$d_{x^2-y^2}$	p_y	$\frac{1}{2}\sqrt{3}m(l^2-m^2)V_{pd\sigma} + m(1+l^2+m^2)V_{pd\pi}$
d_{xy}	p_z	$\sqrt{3}lmnV_{pd\sigma} - 2lmnV_{pd\pi}$
d_{yz}	p_z	$\sqrt{3}mn^2V_{pd\sigma} + m(1-2n^2)V_{pd\pi}$
$d_{3z^2-r^2}$	p_z	$n[n^2 - \frac{1}{2}(l^2+m^2)]V_{pd\sigma} + \sqrt{3}n(l^2+m^2)V_{pd\pi}$
d_{zx}	p_z	$\sqrt{3}ln^2V_{pd\sigma} + l(1-2n^2)V_{pd\pi}$
$d_{x^2-y^2}$	p_z	$\frac{1}{2}\sqrt{3}n(l^2-m^2)V_{pd\sigma} - n(l^2-m^2)V_{pd\pi}$
d_{xy}	p_x	$\sqrt{3}l^2mV_{pd\sigma} + m(1-2l^2)V_{pd\pi}$
d_{yz}	p_x	$\sqrt{3}lmnV_{pd\sigma} - 2lmnV_{pd\pi}$
$d_{3z^2-r^2}$	p_x	$l[n^2 - \frac{1}{2}(l^2+m^2)]V_{pd\sigma} - \sqrt{3}ln^2V_{pd\pi}$

Continued on Next Page...

Table 3.1 – Continued

α	β	Slater-Koster integral
d_{zx}	p_x	$\sqrt{3}l^2nV_{pd\sigma} + n(1-2l^2)V_{pd\pi}$
$d_{x^2-y^2}$	p_x	$\frac{1}{2}\sqrt{3}l(l^2-m^2)V_{pd\sigma} + l(1-l^2+m^2)V_{pd\pi}$
d_{xy}	d_{xy}	$3l^2m^2V_{dd\sigma} + (l^2+m^2-4l^2m^2)V_{dd\pi} + (n^2+l^2m^2)V_{dd\delta}$
d_{xy}	d_{yz}	$3lm^2nV_{dd\sigma} + ln(1-4m^2)V_{dd\pi} + ln(m^2-1)V_{dd\delta}$
d_{xy}	$d_{3z^2-r^2}$	$\sqrt{3}lm[n^2-\frac{1}{2}(l^2+m^2)]V_{dd\sigma} - \sqrt{3}2lmn^2V_{dd\pi}$
		$+\frac{1}{2}\sqrt{3}lm(1+N^2)V_{dd\delta}$
d_{xy}	d_{zx}	$3l^2mnV_{dd\sigma} + mn(1-4l^2)V_{dd\pi} + mn(l^2-1)V_{dd\delta}$
d_{xy}	$d_{x^2-y^2}$	$\frac{3}{2}lm(l^2-m^2)V_{dd\sigma} + 2lm(m^2-l^2)V_{dd\pi} + \frac{1}{2}lm(l^2-m^2)V_{dd\delta}$
d_{yz}	d_{yz}	$3m^2n^2V_{dd\sigma} + (m^2+n^2-4m^2n^2)V_{dd\pi} + (l^2+m^2n^2)V_{dd\delta}$
d_{yz}	$d_{3z^2-r^2}$	$\sqrt{3}mn[n^2-\frac{1}{2}(l^2+m^2)]V_{dd\sigma} + \sqrt{3}mn(l^2+m^2-n^2)V_{dd\pi}$
		$-\frac{1}{2}\sqrt{3}mn(l^2+m^2)V_{dd\delta}$
d_{yz}	d_{zx}	$3lmn^2V_{dd\sigma} + lm(1-4n^2)V_{dd\pi} + lm(n^2)V_{dd\delta}$
d_{yz}	$d_{x^2-y^2}$	$\frac{3}{2}mn(l^2-m^2)V_{dd\sigma} - mn[1+2(l^2-m^2)]V_{dd\pi}$
		$+mn[1+\frac{1}{2}(l^2-m^2)]V_{dd\delta}$
$d_{3z^2-r^2}$	$d_{3z^2-r^2}$	$[n^2-\frac{1}{2}(l^2+m^2)]^2V_{dd\sigma} + 3n^2(l^2+m^2)V_{dd\pi}$
		$+\frac{3}{4}(l^2+m^2)^2V_{dd\delta}$
$d_{3z^2-r^2}$	d_{zx}	$\sqrt{3}ln[n^2-\frac{1}{2}(l^2+m^2)]V_{dd\sigma} + \sqrt{3}ln(l^2+m^2-n^2)V_{dd\pi}$
		$-\frac{1}{2}\sqrt{3}ln(l^2+m^2)V_{dd\delta}$
$d_{3z^2-r^2}$	$d_{x^2-y^2}$	$\frac{1}{2}\sqrt{3}(l^2-m^2)[n^2-\frac{1}{2}(l^2+m^2)]V_{dd\sigma} + \sqrt{3}n^2(m^2-l^2)V_{dd\pi}$
		$+\frac{1}{4}\sqrt{3}(n^2+1)(l^2-m^2)V_{dd\delta}$
d_{zx}	d_{zx}	$3l^2n^2V_{dd\sigma} + (l^2+n^2-4l^2n^2)V_{dd\pi} + (m^2+l^2n^2)V_{dd\delta}$
d_{zx}	$d_{x^2-y^2}$	$\frac{3}{2}ln(l^2-m^2)V_{dd\sigma} + ln[1-2(l^2-m^2)]V_{dd\pi}$
		$-ln[1-\frac{1}{2}(l^2-m^2)]V_{dd\delta}$
$d_{x^2-y^2}$	$d_{x^2-y^2}$	$\frac{3}{4}(l^2-m^2)^2V_{dd\sigma} + [l^2+m^2-(l^2-m^2)^2]V_{dd\pi}$
		$+[\frac{1}{4}(l^2-m^2)^2+n^2]V_{dd\delta}$

Table 3.1: The Slater-Koster table for all interactions between s, p and d-orbitals. These are given as a function of the direction cosines l, m and n (as the bond between the two atoms is along [l, m, n]), and the fundamental integrals.

3.2.1 Analytic approach

Previously PLATO implemented a hard-coded approach to calculating Slater-Koster integrals. This means that all of the relevant Slater-Koster integrals for s, p and d-orbitals (and the corresponding first derivatives) were analytically evaluated, simplified and then directly added to the PLATO code (this effectively means directly adding Table 3.1 to the PLATO code). This code would then have been optimised so that calculations would happen quickly. This type of approach does have the advantage of being fast, however, it does mean that it is only possible to evaluate integrals which have been explicitly defined within the code.

If one was to extend this approach towards f-orbitals then it would certainly be a formidable challenge. As Table 3.1 shows, the Slater-Koster integrals become more complex (and have more fundamental integrals) with increasing values of l. Previous attempts to publish Slater-Koster integrals for f-orbitals have been blighted by both the complexity of the simplifications required to manipulate the integrals in as simple a form as possible, and by human error (most often typing errors). As such, unlike s, p and d-orbitals, there is no definitive published list of Slater-Koster integrals for f-orbitals.

In order to implement an analytic approach for f-orbitals within PLATO, first a correct list of Slater-Koster integrals for them would be required. This could be generated using a recursive technique as outlined in the subsequent section. However, significant work would be required to simplify the resulting integrals as the final form generated by the recursive technique is far from optimal (in computational terms). Even when a list of Slater-Koster integrals for f-orbitals (which would include all s-f, p-f, d-f and f-f interactions) can be agreed upon, then actually adding these to the code would be a further large hurdle to overcome. From a programming point of view, implementing individual integrals could be potentially an error prone procedure that would be very

hard to validate and debug; this is because of the shear volume of code that would have to be written for the integrals in an analytic approach.

In addition to adding the Slater-Koster integrals for the f-orbitals, all the routines and data structures that use these integrals would need to be extended in order to accommodate the changes. The data structures within PLATO for the analytic approach were defined with σ, π and δ defining the size of the structures, so this would need to be changed add ϕ. The routines would need to be extended for ϕ parts as well, as all the σ, π and δ parts were individually dealt with. Finally, all the indexing for these routines and data structures would have to be altered, so that it would be in line with and able to access the new f-orbital parts.

The whole procedure of adding f-orbitals to the existing analytic approach, would be possible but it would be complicated. Furthermore, if in the future it was decided that to extend PLATO to deal with, for example g-orbitals, then this whole procedure would have to be repeated, and the level of complexity of doing so would increase significantly. The fundamental problem with hard-coding is that the approach lacks any flexibility, and this is the reason why the practise is frowned upon by the computing fraternity. For these reasons we chose to implement a recursive approach to calculating Slater-Koster integrals, which is discussed in the remainder of this Chapter.

3.2.2 Recursive approach

The following recursive approach to calculating the Slater-Koster integrals and their derivatives is the work of Podolskiy and Vogl [20] and Elena and Meister [21]. Consider two atoms at positions $\mathbf{R_1}$ and $\mathbf{R_2}$ respectively, that are characterised by the quantum numbers l_1, m_1 and l_2, m_2 respectively (these are the angular and magnetic quantum numbers, no other quantum numbers play a role in the following discussion). In the two-centre approximation all the Hamiltonian matrix elements depend only on the relative positions of the two atoms, and can be manipulated to depend only on the vector connecting $\mathbf{R_1}$ and $\mathbf{R_2}$.

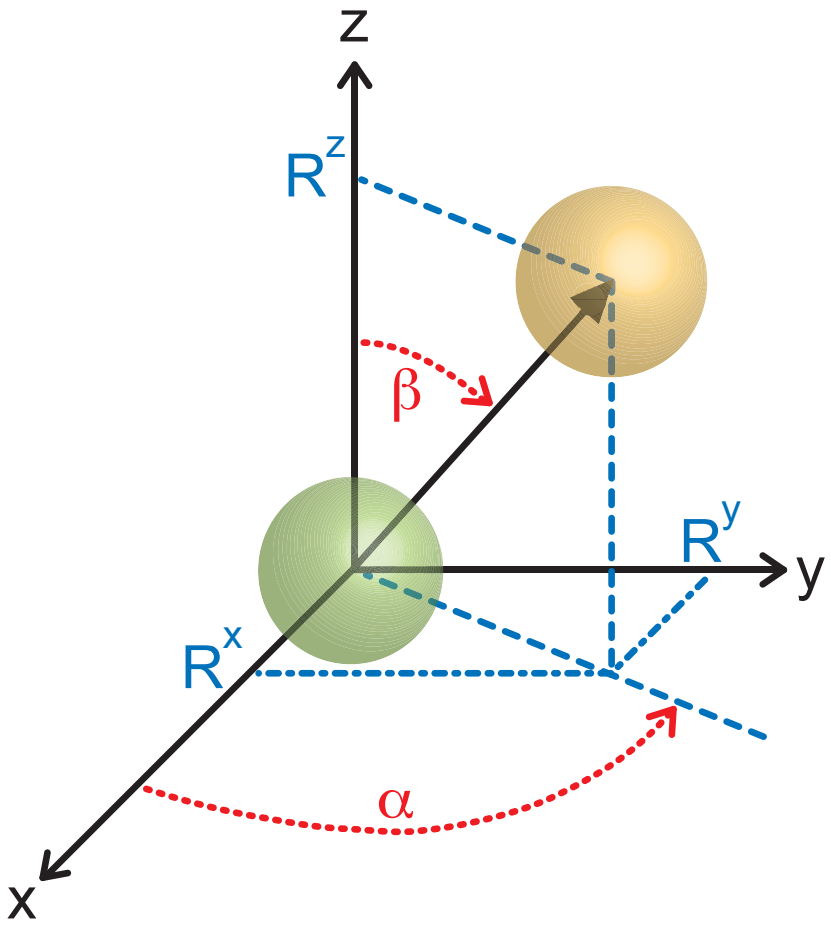

Figure 3.5: Defining the system of two atoms, one centred at the origin (0, 0, 0) and the second atom centred at (R^x, R^y, R^z). The two Euler angles of rotation, α and β, are illustrated here.

This enables the problem to be translated so that one of the atoms is positioned at the origin of the co-ordinate system being used (which is helpful). This gives the second atom the Cartesian co-ordinates, R^x, R^y, R^z. Two Euler angles of rotation, α and β, can then be introduced and defined as the angles of rotation in order to bring the z-axis and the xz plane into alignment with the connecting vector between two atoms. This system is illustrated in Figure 3.5.

The first rotation angle, α, is about the z-axis, from the positive x-axis to the connecting vector between the two atoms, thus $0 \leq \alpha < 2\pi$. The second rotation angle, β, is about the newly created y'-axis, following the rotation through α,

and it starts from the positive z-axis, so $0 \leq \beta \leq \pi$. The case were $(R^x)^2 + (R^y)^2 = 0$ is a unique case that is dealt with in a slightly different manner, as this gives β to be defined as either 0 or π, while α is completely undefined.

The Slater-Koster tables express a general matrix element between unrotated functions, in terms of the fundamental matrix elements (which are defined in a rotated frame[1]) and coefficients dependent on the angular momentum quantum numbers of the two states involved. The form of the general matrix element (the Slater-Koster integral) is given in Equation 3.5.

$$\begin{aligned}
&\langle l_1 m_1 | H | l_2 m_2 \rangle \, (\alpha, \beta, R) \\
&= \sum_{m'=1}^{l_<} \left[S^{l_1}_{m_1 m'}(\alpha,\beta) S^{l_2}_{m_2 m'}(\alpha,\beta) + T^{l_1}_{m_1 m'}(\alpha,\beta) S^{l_2}_{m_2 m'}(\alpha,\beta) \right] \times (l_1 l_2 | m' |)(R) \\
&\quad + 2 A_{m_1}(\alpha) A_{m_2}(\alpha) d^{l_1}_{|m_1|0}(\beta) d^{l_2}_{|m_2|0}(\beta) \times (l_1 l_2 0)(R)
\end{aligned} \tag{3.5}$$

The upper limit, $l_<$, for the summation in Equation 3.5, is given as the maximum value of the two angular momentum components l_1 and l_2. Also in Equation 3.5,an abbreviation (A_m) has been introduced to simplify proceedings, which is evaluated as shown in Equation 3.6.

$$A_m(\alpha) = \begin{cases} (-1)^m \left[\tau(m) \cos(|m|\alpha) + \tau(-m) \sin(|m|\alpha) \right] & \text{if } m \neq 0 \\ \frac{1}{\sqrt{2}} & \text{if } m = 0 \end{cases} \tag{3.6}$$

In Equation 3.6 a discrete Heaviside function, τ, has been introduced, which is defined in Equation 3.7:

$$\tau(m) = \begin{cases} 1 & \text{if } m \geq 0 \\ 0 & \text{if } m < 0 \end{cases} \tag{3.7}$$

[1]If we define a spherical harmonic in the unrotated co-ordinates then we have $Y_{lm}(\theta, \varphi)$, where θ is measured from the positive z-axis and φ is measured from the positive x-axis. Then a spherical harmonic defined in the rotated frame, corresponds to $Y^{\xi}_{lm}(\theta', \varphi')$, where θ' is measured from the positive $\overrightarrow{\xi}$-axis, and φ' is measured from the new x'-axis.

Two further abbreviations ($S^l_{mm'}$ and $T^l_{mm'}$) were also introduced into Equation 3.5, and these are evaluated in Equations 3.8 and 3.9 respectively.

$$S^l_{mm'} = A_m \left[(-1)^{m'} d^l_{|m|m'} + d^l_{|m|-m'} \right] \tag{3.8}$$

$$T^l_{mm'} = B_m (1 - \delta_{m0}) \left[(-1)^{m'} d^l_{|m|m'} - d^l_{|m|-m'} \right] \tag{3.9}$$

In Equation 3.9, the δ_{m0} is a Kronecker delta[2]. A further abbreviation (B_m) has been introduced to simplify proceedings, which is evaluated as shown in Equation 3.10.

$$B_m(\alpha) = \begin{cases} (-1)^m \left[\tau(-m)\cos(|m|\alpha) - \tau(m)\sin(|m|\alpha) \right] & \text{if } m \neq 0 \\ 0 & \text{if } m = 0 \end{cases} \tag{3.10}$$

The Wigner function, $d^l_{mm'}$, which is used in Equations 3.8 and 3.9, is given explicitly in Equation 3.11. In this equation the upper limit, $k_<$, for the summation is given as the maximum value of $(l - m)$ and $(l - m')$. The starting value for the summation, $k_>$, is given as the maximum of either 0 or $(-m - m')$.

$$\begin{aligned} d^l_{mm'}(\beta) = {} & 2^{-l}(-1)^{l-m'} \left[(l+m)!(l-m)!(l+m')!(l-m')! \right]^{\frac{1}{2}} \\ & \times \sum_{k=k_>}^{k_<} \frac{(-1)^k (1-\cos\beta)^{l-k-(m+m')/2} (1+\cos\beta)^{k+(m+m')/2}}{k!(l-m-k)!(l-m'-k)!(m+m'+k)!} \end{aligned} \tag{3.11}$$

This recursive approach has also been extended to calculate the first and second derivatives of the matrix elements [21], and as such we have included in PLATO this approach for the calculation of the first derivatives.

[2]The Kronecker delta, δ_{m0}, is a function of two variables, in this case m and 0. The function is equal to 1 if the two variables are equal, and 0 if they are not.

3.3 Implementing recursive Slater-Koster routines within PLATO

In Figure 3.6 the general approach for the first task (programming the recursive Slater-Koster routines) is shown. Initially, as with most programming projects, a pseudocode implementation was conceived. This served the purpose of not only familiarising ourselves with the generic recursive approach, but as we chose to actually implement it within the mathematical software Maple, it actually provided a working model that was used at a later stage to aid with debugging the version within PLATO.

The next step (still within Figure 3.6) shows the task of building these routines (both for the Slater-Koster integrals and their first derivatives) within PLATO; this required knowledge of how PLATO actually operates, how and where variables are stored, and many other factors. The tasks of debugging and testing our implementation of the generic recursive approach were complex due to both the sheer number of integrals that get calculated in even just setting up a calculation in PLATO (in the region of hundreds of thousands, if not millions), and difficulties in tracking errors in such a large piece of the code (isolating errors also became a problem due the large number of integrals being calculated). At that point it was possible to check the results for the s, p, and d-orbitals, as the new results could always be compared with those found by the analytic routines, however, the f-orbitals were a different matter entirely.

With the f-orbitals the main issue became one of a general lack of reference points, as the only real way of checking integral values was by checking individual values against those provided by the Maple implementation. This complicated proceedings as there was now a reliance on the accuracy of the Maple implementation (so errors in both became hard to identify and solve), and checking individual integrals is far from efficient.

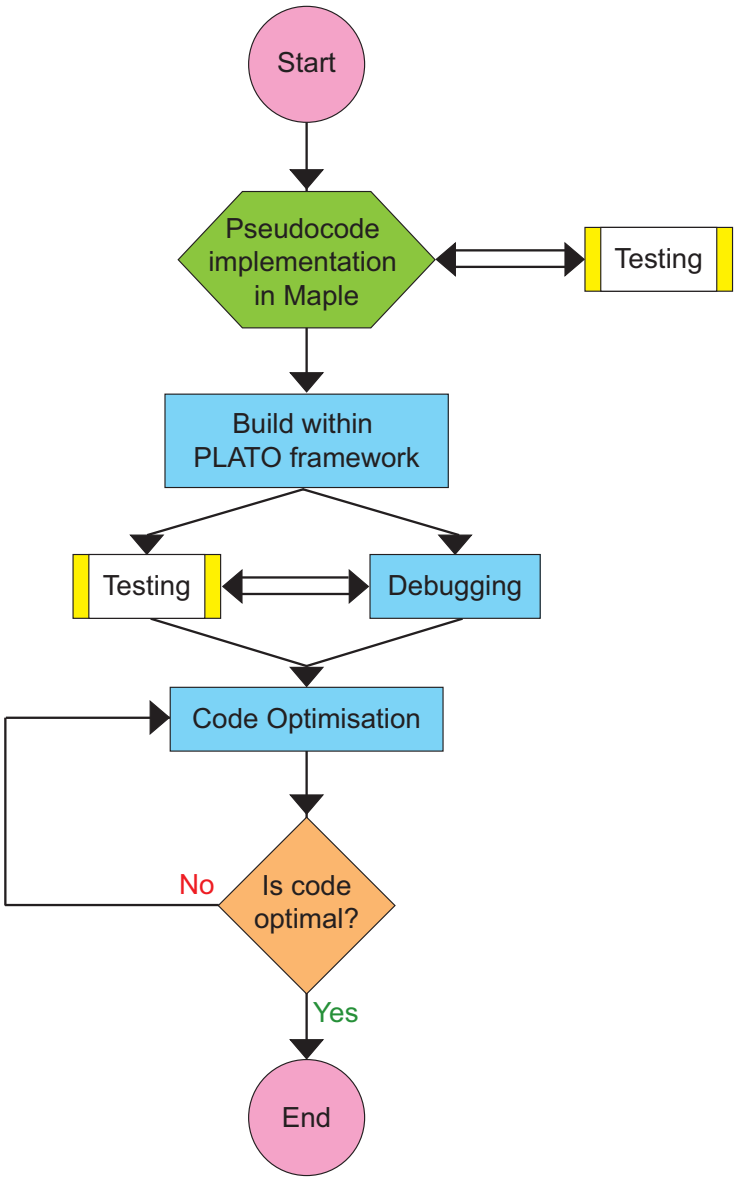

Figure 3.6: A flow chart for implementation of the recursive Slater-Koster routines for both the integrals and the first derivatives within PLATO.

The final few steps in Figure 3.6 deal with the optimisation, for speed, of our recursive Slater-Koster routines. As previously mentioned the amount of times these routines are called within PLATO is huge, and as such the operation of PLATO in general can be crippled by inefficient coding. Almost as much time was spent on optimising the Slater-Koster routines as actually writing, testing and debugging them. This is dealt with in-depth in Sub-Section 3.3.1.

The recursive approach means that there is not the need to code explicitly in any Slater-Koster integrals. This gives the program great flexibility, and the scope to go beyond f-orbitals if required. This approach, however, did require though that all parts of PLATO related to Slater-Koster integrals had to be flexible, as if any one part remained hardcoded then that would nullify the work on the rest of the code and would severely limit future development. The generalisation of PLATO is the focus of Section 3.4.

3.3.1 Code optimisation

Once we were satisfied that our implementation of the recursive routines was technically correct, we then had to focus on how the code was actually written and executed. The Slater-Koster routines in PLATO are essentially a small (but vital) part of a very much larger program. What we could not accept was any significant impact on run-time to be brought about by the new recursive routines. On initial testing the new recursive routines increased overall simulation times by around 300%, compared to the analytic routines. This created an unacceptable bottleneck within PLATO.

The main reason for this bottleneck was a lack of experience, on my part, of writing compact code that minimises system resources. Some of the significant changes that were made to our original implementation of the recursive Slater-Koster routines are outlined below:

Calls to system functions are computationally expensive, and should be reduced at all costs. A good example of this is the calls to the square root function (called sqrt) in C (PLATO was written in this programming language). Instead of calculating square roots of integers every time that a square root is required, the code was altered so that it initially works out all the square roots that it will require, and then evaluates and stores them so that they are accessible to all subroutines within the larger Slater-Koster routine (in a global array). This might only seem like a small change, but instead of 100,000's of calls to the sqrt function there will now be somewhere in the region of 10. Another solution to

this problem could have been to simply create a fixed data structure (a hard-coded array) with square roots already evaluated stored in it. This however would go against the flexible methodology we introduced throughout PLATO.

Calling any routine, no matter how simple, is computationally expensive. As shown above with the system function sqrt, calling the same function repeatedly can significantly affect performance. This also applies to user created routines. In the first implementation of the Slater-Koster routines within PLATO all of the different parts of the methodology (so each of the Equations from 3.5 to 3.11) had it's own separate subroutine within the main Slater-Koster routine. So for the routine based for $S^l_{mm'}$ (see Equation 3.8) would have in turn called the routines related to A_m (see Equation 3.6) and $d^l_{mm'}$ (see Figure 3.11). Therefore if we now focus on the routine for the function A_m, this routine is called numerous times within a single call to the main Slater-Koster routine; hence instead of calling it multiple times, it is called once and then the result is stored in a way that is accessible to the main Slater-Koster routine, and all of its subroutines (in a global array again). Furthermore, within each call to the main Slater-Koster routine, the A_m routine can only have two different inputs, m_1 and m_2 (corresponding to the magnetic quantum numbers of the two atoms concerned). Since there is the distinct possibility that some of the function calls and mathematical evaluations within the A_m routine could be identical for both m_1 and m_2 (obviously this depends on values of m_1 and m_2), both A_{m_1} and A_{m_2} are calculated within the same subroutine.

By combining routines it is possible to reduce total execution time of the routines. When there are two very similar routines, that at times perform identical calculations, by merging these routines together it is possible to reduce computational cost. A good example of how these types of changes can affect things is the difference in the handling of the A_m and B_m in the initial Slater-Koster recursive implementation and the final one. Looking at the two Equations involved (Equations 3.6 and 3.10), it is clear that there are similarities between the two functions. For example the cosine and sine evaluations in the two equations

are identical, so by merging the two A_m and B_m routines, each cosine and sine only needs to be calculated once compared to twice if the A_m and B_m functions were dealt with separately. Again changes of this ilk can result in significant savings in terms of the all important computational effort. Similar changes were also made to the implementation of the $S^l_{mm'}$ and $T^l_{mm'}$ (Equations 3.8 and 3.9 respectively).

Where at all possible we have tried to eliminate needless function calls entirely. There are many times within the recursive implementation that it is required to evaluate $(-1)^m$, where $m \geq 0$, but instead of using the power function (called pow in C) to evaluate this, it is possible to take advantage of the fact that the result is always going to be $\pm$ 1, depending on the value of m. So instead of using the pow function to evaluate this, we have used a simple logical statement (in this case an 'if' statement) to determine the result, based solely on the input (m); this is less computationally expensive than calling the pow function. An extension of this principle can be found in the main Slater-Koster routine, where a series of calls to the pow function were once required. After the initial few terms in the sequence are evaluated using calls to the costly pow function, subsequent calls to the pow function are avoided as the remaining required terms are calculated recursively, using the initial few terms.

PLATO has been written so that it can be run on a large range of systems, so it was a high priority that this system independence was retained in the latest incarnation of PLATO. Due to the range of systems and compilers that are used, this became somewhat difficult. Some compilers interpret the syntax and semantics of the language in slightly different ways, for example, a declared but unassigned variable can be subject to different treatment depending on the compiler used. In the end the best approach became to test exhaustively on the different systems at our disposal, and to be as strictly correct in the syntax and semantics used as possible, in order to achieve system independence.

3.3.2 Evaluation

In order to check our implementation of the recursive method for calculating Slater-Koster integrals, and to assess the success (relative to the previous analytic method) of our optimisation efforts, we ran a series of tests. The systems that were used to assess this new version of PLATO are outlined as follows, with a static relaxation being performed for each of them:

1. A pure iron system, consisting of a 16 atom supercell, with one atom removed to create a vacancy (so 15 iron atoms in total). A TNDP basis set was used for this calculation.

2. A strontium titanate 1×1 strontium-oxide terminated surface. The supercell consisted of 17 atoms (4 strontium atoms, 3 titanium atoms and 10 oxygen atoms). Again a TNDP basis set was used for the calculation.

3. A buckminsterfullerene in isolation, C_{60}. Where, obviously, the supercell consisted of 60 carbon atoms. A DNP basis set was used in this calculation.

It was felt that these three systems would give a broad enough test for the changes to PLATO's code. The fullerene gives a good idea of how smaller basis sets would be affected, and was also a test of small isolated systems. The $SrTiO_3$ surface would test how the program copes with multiple atom species, and because of the periodic boundary conditions, the system is effectively a series of slabs, which again was another type of system covered. The iron system not only gave a different test because it is a defect calculation, but it is also a bulk calculation (within periodic boundary conditions), and the iron atoms posses spin (a complication which further tests the alterations). The simulations for both the iron and $SrTiO_3$ systems were calculated with TNDP basis sets that represent the previous highest level of basis set completeness possible.

The calculations for the outlined systems were performed using both the recursive and analytic routines, and the timings for the calculations are given in Figure 3.7. The total energy results for each pair of calculations were identical

(PLATO outputs energies to seven decimal places), which was slightly surprising as we did expect a few minor differences. The reason for that expectation is that the number of operations required to calculate an integral via the recursive method is significantly higher compared to the analytic method, so expecting rounding errors would not be unreasonable.

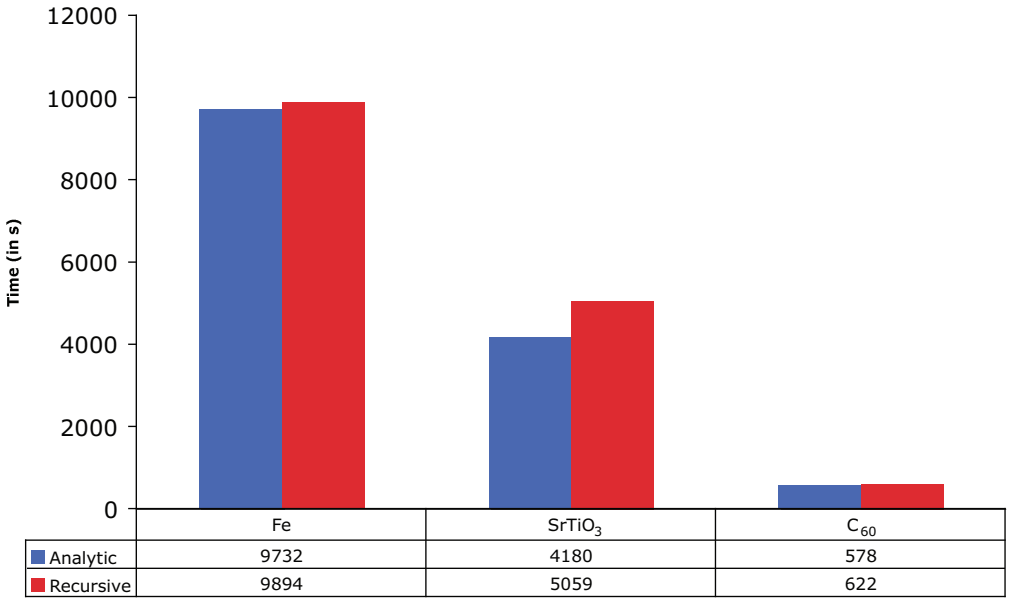

	Fe	$SrTiO_3$	C_{60}
Analytic	9732	4180	578
Recursive	9894	5059	622

Figure 3.7: Comparison of simulation times for the chosen test systems. Calculations were performed using both the analytic and recursive Slater-Koster routines.

As can be seen in Figure 3.7, the differences, in terms of simulation times, between the recursive and analytic Slater-Koster routines are not significant. The iron and fullerene systems had increases of 2% and 8% respectively. The reason why the fullerene suffered from a greater increase, could be due to the balance between the integral mesh and the Slater-Koster routines. In a more complex system such as the iron one (which has more basis functions), the computing cost of the recursive method is absorbed more in the general calculation (the calculation cost of the Slater-Koster integrals becomes less significant). The strontium titanate system is also complex, but the increase in simulation time

is even greater in this system, 21% in this case. Here the calculation suffers due to the higher number of atom species, as this means a greater number of Slater-Koster integrals are required for the calculation, thus the difference becomes more pronounced.

The general trend demonstrated in Figure 3.7 is that the recursive Slater-Koster method is slower than the analytic method. As explained, the recursive method contains many more calculations than it's analytic counterpart, many of which are function calls, and all of which equate to greater computational times; this is despite a considerable effort in optimising the recursive routines. This increase could be avoided if the f-orbitals were included in the analytic method, however as previously mentioned, this would be massively time consuming and very complicated to test and debug.

For those reasons we settled on a compromise. By default PLATO will only use the recursive method if the calculation requires it, in other words, if the basis set consists of orbitals other than the s, p and d-orbital types. We have included an option within PLATO that will force the calculation to use the recursive method for all Slater-Koster integrals. This can be achieved by setting the value for the relevant variable (called SKFlag) in the PLATO input file to 1 from the default 0. If the variable, SKFlag, is unspecified in the PLATO input file, then the recursive method will only be used if required (*i.e.* the default configuration).

3.4 Generalisation of PLATO

The second task (implementing the generic approach throughout the whole of PLATO) is outlined in Figure 3.8. One of the main differences to the first task is that the changes were no longer localised to the main PLATO program (called TB2), but one of the support programs also needed alterations. This program is called TBInt, and it generates the integral tables that are stored in a file format prior to PLATO calculations in order to reduce significantly

the computational effort (as outlined in Chapter 2). This further complicated things, as is illustrated by both the complexity of Figure 3.8 compared to Figure 3.6 and the inclusion of feedback loops within the latter.

Often at times the development of the TBInt and PLATO took on more of a parallel approach compared to the serial approach shown in Figure 3.8. Some of the changes made were of fundamental importance to the operation of both programs. In fact the formatting and contents of some of the file-based integral tables have been altered. As such new testing routines were created and added to the already significant number found within the PLATO program.

The code optimisation parts of this second task were less intense than for the previous task, mostly because the amount of new code was minimal (this task consisted of mostly simplifying existing code and implementing smaller recursive routines). Overall the changes in the second task were significantly more widespread than in the first task, and while the changes fundamentally altered how parts of the program are called and how the data is internally stored, the actual operation of the code for the most part remained unchanged.

The debugging parts, however, were much more complicated in this second task; the main reason for this is that often it was difficult to pinpoint what and where the problem was. Often it was an issue trying to tell if the problem was with the TBInt program or with TB2. As outlined while discussing the first task, error checking the f-orbitals was not easy due to the lack of a reference point.

The main problem with generalising PLATO (and TBInt) was actually, on paper at least, quite simple. The indexing of the new flexible arrays (which replaced the previous hardcoded ones) was hampered by differences in how the orbitals are ordered by different parts of the program. This ordering of the orbitals issue meant that the same l and m values would correspond to different orbitals in different parts of the program. The ordering for the recursive Slater-Koster method is given in Table 3.2. In the end this issue was resolved by using only the recursive Slater-Koster method in TBInt (unlike PLATO, there is no

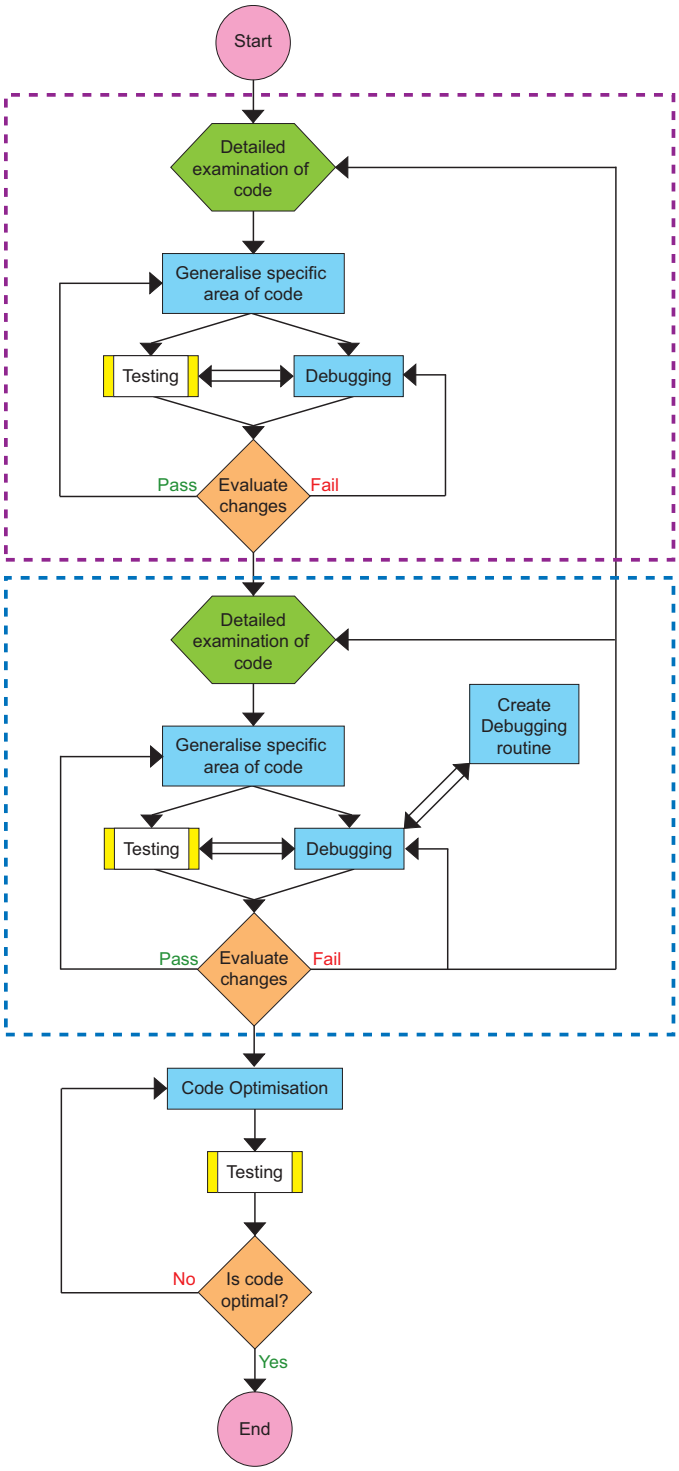

Figure 3.8: A flow chart for implementation of the generalisation of PLATO. The parts within the purple dashed line deal with the program, TBInt, and the parts within the blue dashed line deal with the changes made to PLATO itself.

option to switch between analytic and recursive methods), thus maintaining consistency. The recursive Slater-Koster routine within PLATO re-orders the s, p and d-orbitals according to the order used in the rest of the program.

l	m	Orbital
0	0	s
1	-1	p_y
1	0	p_z
1	1	p_x
2	-2	d_{xy}
2	-1	d_{yz}
2	0	$d_{3z^2-r^2}$
2	1	d_{zx}
2	2	$d_{x^2-y^2}$

Table 3.2: Ordering for orbitals within the recursive Slater-Koster method. This is subtly different than in the other routines within PLATO.

In general the actual changes made to the programs reduced the actual quantity of code, and instead of specific code for each σ, π and δ part, we implemented a loop that would work for all values of l. Where needed, small recursive routines were added to the code replacing the rigid hardcoded parts. As with any programming project of this magnitude, all the changes to both programs have been extensively documented and justified.

3.5 Testing

With the significant changes made to both PLATO and TBInt, testing was vital, especially as after testing the altered version would be rolled out for other users. We started with smaller systems and gradually increased system complexity, and tested a wider range of system types. This was to make sure all changes

were correct and to help catch any mistakes or omissions. The testing was also of interest as it could give an insight into the potential gain in terms of computational accuracy that could be achieved by including f-orbitals in basis sets.

3.5.1 Testing with silver systems

We started by looking at silver basis sets and simple pure silver systems. To begin with new basis sets had to be created. This task had to be carried out for all the basis sets as the fundamental changes we had made to the basis set files meant that previous basis set files would not work. We have used the standard basis set types, single numeric (SN), double numeric polarization (DNP) and triple numeric double polarization (TNDP); and these basis sets consist of the following orbitals, sd (SN), $sds^*p^*d^*$ (DNP) and $sds^*p^*d^*s^{**}p^{**}d^{**}$ (TNDP). For each of these three basis sets we have created another basis set that contains the same orbitals, however, with the addition of a f^{**}-orbital. For the orbitals in these silver basis sets, the 2+ and 4+ charged states were used for the * and ** orbitals respectively. This results in six different basis sets for investigation.

We have used these six basis sets to calculate the bulk properties of silver, the results of which are presented in Table 3.3. As expected the energy per atom becomes lower as the number of orbitals in the basis set is increased. The most significant thing about the results is that for the smaller basis sets, the SN and to a lesser extent the DNP, there appears to be a noticeable improvement in bulk properties if f-orbitals are included. The difference when at the TNDP level of basis sets, seems to be very small in this case.

Following on from the bulk properties calculations we performed some calculations on two atom silver dimers. Within these calculations the dimer has been placed in isolation, and as such periodic boundary conditions have not been applied. The cell size used was 20 Å, and the two silver atoms were placed 3 Å apart. This large cell should ensure that all interactions are kept within the cell (the basis set cut off is 8 Å).

Basis set orbitals	a (in Å)	B (in MBar)	Energy per atom (in eV)
sd	4.29	0.78	-1007.88
sdf^{**}	4.19	0.88	-1008.13
$sds^{*}p^{*}d^{*}$	4.23	0.78	-1008.52
$sds^{*}p^{*}d^{*}f^{**}$	4.21	0.79	-1008.57
$sds^{*}p^{*}d^{*}s^{**}p^{**}d^{**}$	4.16	0.88	-1008.70
$sds^{*}p^{*}d^{*}s^{**}p^{**}d^{**}f^{**}$	4.16	0.88	-1008.73
Plane wave [34]	4.17	0.87	N/A

Table 3.3: Ag basis sets bulk properties, showing the lattice constant a, the bulk modulus B, and the energy per atom, for all the basis sets outlined. These are compared to values calculated with a plane wave basis.

Basis set orbitals	Internal energy (in eV)	Simulation time (in Secs)
sd	-2007.24	24
sdf^{**}	-2007.25	37
$sds^{*}p^{*}d^{*}$	-2007.34	40
$sds^{*}p^{*}d^{*}f^{**}$	-2007.36	57
$sds^{*}p^{*}d^{*}s^{**}p^{**}d^{**}$	-2007.37	51
$sds^{*}p^{*}d^{*}s^{**}p^{**}d^{**}f^{**}$	-2007.39	63

Table 3.4: Ag dimer single point calculations, giving both the internal system energy, in eV, and the time required for PLATO to perform the simulation, in seconds. The calculations were all performed on the same computer in an effort to reduce any inherent bias.

Basis set orbitals	Internal energy (in eV)	Simulation time (in Mins)
sd	-2007.60	19.9
sdf^{**}	-2007.63	39.6
$sds^{*}p^{*}d^{*}$	-2007.76	63.0
$sds^{*}p^{*}d^{*}f^{**}$	-2007.79	59.9
$sds^{*}p^{*}d^{*}s^{**}p^{**}d^{**}$	-2007.85	64.7
$sds^{*}p^{*}d^{*}s^{**}p^{**}d^{**}f^{**}$	-2007.89	54.4

Table 3.5: Ag dimer static relaxation calculations, giving both the internal system energy, in eV, and the time required for PLATO to perform the relaxation, in minutes. The calculations were all performed on the same computer in an effort to reduce any inherent bias.

The results from these calculations are given in Table 3.4. It is clear that the internal energy becomes lower as more basis set functions are included. The interesting trend seen from these results is that the simulation timings show that the cost (in terms of simulation time) is not perhaps as justified in terms of calculational improvement as hoped (a greater improvement in calculated energies had been hoped for, especially because of the extra computational time required). It is possible that this could be due to the simplicity of the system in question.

We have then repeated the calculations on the same dimer systems, however, this time a static relaxation has been performed. The results for these calculations are presented in Table 3.5.

As Table 3.5 shows, the improvement in terms of internal energies with increasing numbers of basis functions is again demonstrated here. This time however, the improvements of adding f-orbitals to the basis sets are more noteworthy, especially the difference in simulation times when looking at the SN, DNP and TNDP basis sets and the f-orbital counterparts. The sdf^{**} simulation time is nearly twice that of the sd time, which given that it has more than twice

as many basis functions is not surprising. The other basis sets are interesting as the simulation times actually reduce on the inclusion of the f-orbitals. The reason for these reductions in simulation time, is that the f-orbitals provide a more complete description of the interactions, which actually affects the number of iterations PLATO performed in order to reach convergence. It should be noted that this improvement occurs despite the fact the f-orbitals have to use the slightly slower recursive Slater-Koster method.

3.5.2 Testing with silicon systems

The next atom species we decided to test was silicon. Again we created the same series of basis sets as we did for silver systems; when doing so we created each basis set at three different cut off radii, these distances being 6, 7 and 8 Bohr radii. We calculated bulk silicon properties for all these basis sets, and chose the most suitable cut off radius for each basis set group based on these results. The final selection of basis sets and the calculated bulk properties are given in Table 3.6.

Basis set orbitals	a (in Å)	B (in MBar)	Energy per atom (in eV)
sp	5.42	1.09	-106.80
spf^{**}	5.53	0.81	-107.20
$sps^{*}p^{*}d^{*}$	5.41	0.90	-107.68
$sps^{*}p^{*}d^{*}f^{**}$	5.40	0.93	-107.76
$sps^{*}p^{*}d^{*}s^{**}p^{**}d^{**}$	5.39	0.94	-107.79
$sps^{*}p^{*}d^{*}s^{**}p^{**}d^{**}f^{**}$	5.39	0.93	-107.82
Plane wave [18]	5.39	0.96	-107.86

Table 3.6: Silicon basis sets bulk properties. We tested all basis sets at three cutoffs 6, 7, and 8 Bohr radii. The following are the best results; the cutoff of 7 Bohr radii gave the best results for all the basis sets, with the exception of the sp basis set where the cutoff of 6 Bohr radii proved the most suitable. These are compared to values calculated with a plane wave basis.

As can be seen from Table 3.6, the bulk properties of the basis sets improve as the number of orbitals included increases. This is more noticible when looking at the energies per atom, which is shown to get closer to the plane wave calculations [18] with each addition to the basis set. Following this initial work, we performed calculations on a perfect silicon bulk system of 64 atoms. A vacancy defect was then created in the middle of the supercell, leaving 63 atoms, and we then performed calculations on these new systems. The defect formation energies were then calculated and the results are given in Table 3.7.

Basis set orbitals	Vacancy formation energy (in eV)
sp	4.77
spf^{**}	3.08
$sps^{*}p^{*}d^{*}$	3.67
$sps^{*}p^{*}d^{*}f^{**}$	3.76
$sps^{*}p^{*}d^{*}s^{**}p^{**}d^{**}$	3.76
$sps^{*}p^{*}d^{*}s^{**}p^{**}d^{**}f^{**}$	3.75
Plane Wave [18]	3.79

Table 3.7: Silicon vacancy formation energies. Total energy calculations were performed for both the perfect and defect systems, in order to calculate the formation energies. These are compared to a value calculated with a plane wave basis.

Table 3.7 shows some initial oscillation, in terms of vacancy formation energies, for the less complete basis sets; this settles down at the DNP level of basis sets, and the difference between the final two basis sets is minimal. Following on from the vacancy calculations we decided to investigate another type of defect, namely interstitials. We have looked at the tetrahedral and hexagonal interstitials using the same 64 atom system as for the vacancy calculations (in the interstitial systems this increases to 65 atoms); the results are given for the tetrahedral and hexagonal formation energies in Tables 3.8 and 3.9 respectively.

Basis set orbitals	Interstitial formation energy (in eV)
sp	6.61
spf^{**}	6.23
$sps^{*}p^{*}d^{*}$	3.28
$sps^{*}p^{*}d^{*}f^{**}$	3.29
$sps^{*}p^{*}d^{*}s^{**}p^{**}d^{**}$	3.29
$sps^{*}p^{*}d^{*}s^{**}p^{**}d^{**}f^{**}$	3.26
Plane waves [35]	4.07

Table 3.8: Silicon defect formation energies for the tetrahedral interstitial. Total energy calculations were performed for both the perfect and defect systems, in order to calculate the formation energies. These are compared to a value calculated with a plane wave basis.

Basis set orbitals	Interstitial formation energy (in eV)
sp	6.25
spf^{**}	5.78
$sps^{*}p^{*}d^{*}$	3.30
$sps^{*}p^{*}d^{*}f^{**}$	3.29
$sps^{*}p^{*}d^{*}s^{**}p^{**}d^{**}$	3.30
$sps^{*}p^{*}d^{*}s^{**}p^{**}d^{**}f^{**}$	3.26
DFT 217 atom cell [36]	2.87
Plane waves [35]	3.80

Table 3.9: Silicon defect formation energies for the hexagonal interstitial. Total energy calculations were performed for both the perfect and defect systems, in order to calculate the formation energies. These are compared to a value calculated with a larger system size and a value calculated with a plane wave basis.

The results shown in Tables 3.8 and 3.9 demonstrate again that as the num-

ber of basis set functions are increased the interstitial formation energies become smaller. Comparing both sets of results with the corresponding plane waves values [35], there is an increase in formation energies from our results to the plane wave results. The result in Table 3.9 for the larger system size [36] shows a decrease in formation energy from our results. The study by Goedecker *et al.* [36] believed that results from systems of the size that we have employed would not be fully converged, and the study by Leung *et al.* [35] believed that DFT calculations using the LDA (as we have in our calculations) would underestimate the formation energies. While these are both valid points, the sole purpose of our calculations was to assess the impact of including f-orbitals in our basis sets, so the absolute accuracy of these calculations was not the most important thing at stake.

In terms of the general improvement observed in silicon calculations, within PLATO, for the inclusion of f-orbitals, as with silver systems, is minimal. As such the decision on the inclusion of f-orbitals would have to be carefully considered, with perhaps only calculations where the overall accuracy is vital being worthwhile candidates for these larger basis sets.

3.5.3 Testing with nitrogen systems

We decided to look at the nitrogen basis sets, as a decision would be needed in order to investigate endohedral fullerenes in which nitrogen would be the endohedral species. The series of basis sets investigated here are different than previously investigated for silver and silicon. The reason for this is that we were concerned about the extra computational cost that could be incurred by including f-orbitals. As before a variety of basis set cut off radii were explored, this time however a basis set with mixed cut offs was also looked at. For these mixed basis sets, the *sp* orbitals had a cut off of 7 bohr radii, and all remaining orbitals had a cut off of 6 bohr radii. These basis sets were then used to calculate the length of the dimer bond in the N_2 nitrogen molecule; and the results are presented in Table 3.10.

	Cut off 6.5	Cut off 7	Cut off mixed
Basis set orbitals	Length (in Å)	Length (in Å)	Length (in Å)
sp	1.28	1.30	N/A
$sps^*p^*d^*$	1.12	1.12	N/A
$sps^*p^*s^{**}p^{**}$	1.13	1.13	N/A
$sps^*p^*s^{**}p^{**}d^{**}$	1.12	1.12	N/A
$sps^*p^*d^*s^{**}p^{**}$	1.12	1.12	N/A
$sps^*p^*d^*s^{**}p^{**}d^{**}$	1.11	1.11	1.11
$sps^*p^*d^*s^{**}p^{**}d^{**}f^{**}$	1.11	1.11	1.10

Table 3.10: The calculated values for the lengths, in Å, of the Nitrogen N_2 dimer bond. These results are from relaxation calculations performed with PLATO.

The results from Table 3.10 again show the trend illustrated in the previous results, where the increase of basis set orbitals increases the accuracy of the result. When the results from Table 3.10 are compared with the value of the N_2 dimer bond length calculated directly from the pseudopotential [30], of 1.10 Å, it is clear that the most complete basis set (the one including the f-orbitals) is the closest to this pseudopotential result.

3.6 Conclusions

We have investigated how to expand the amount of orbitals permitted within a calculation performed with PLATO; from this we decided upon a recursive method for calculating the Slater-Koster integrals, and their first derivatives, and a generalisation of how PLATO handles the associated structures and routines. The additions and alterations to PLATO were then carried out, and tested extensively in a proper and robust manner. Various small systems were then studied in order to ascertain both the potential gain in accuracy, and the cost in terms of computational effort, of including f-orbitals within a basis set.

It has been shown that at times the gains in accuracy are modest, and that the computational times can be negatively affected. When performing static relaxations, however, the effect of including f-orbitals can be a benefit to both accuracy and computational effort (time).

Chapter 4

Fullerenes on silicon surfaces

4.1 Introduction to fullerenes

The fullerene[1] allotrope of carbon was discovered by Kroto *et al.* [1], as a by-product of vapourisation, by laser irradiation, of graphite. In order to describe the structure for this super stable cluster of 60 carbon atoms (for it was the C_{60} molecule that was the first observed fullerene) a truncated icosahedron was suggested. This structure consists of 20 hexagonal faces and 12 pentagonal faces. The C_{60} molecule, which is the most common of all fullerene molecules, is often compared to the analogue of a traditional 32 panel football where the number and positioning of the hexagons and pentagons are identical. The C_{60} and a 32 panel football are shown in Figure 4.1. The C_{60} molecule was named buckminsterfullerene, after Richard Buckminster Fuller, a world renowned architect whose famous geodesic dome structures demonstrated a startling similarity to the newly discovered carbon molecule. The discovery of the fullerene molecules led to Kroto, Curl and Smalley being awarded the Nobel Prize for Chemistry in 1996.

Each fullerene, from the smallest (the C_{20}) to the largest (fullerenes have been observed with in excess of 100 constituent carbon atoms), will possess exactly

[1]The general structure of a fullerene is a convex closed polyhedron whose faces are pentagons and hexagons.

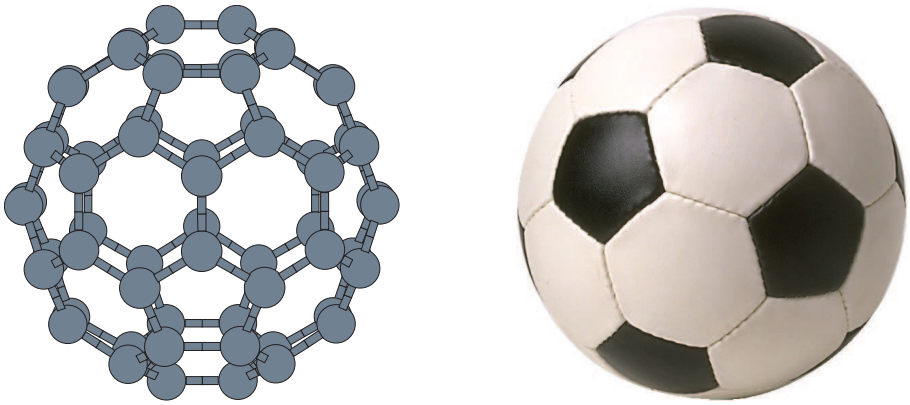

(a) C_{60} molecule (b) Traditional 32 panel football

Figure 4.1: Representations of the buckminsterfullerene, C_{60}, and the common analog of a traditional 32 panel football. If an atom was placed at each of the 60 vertices of the football, then the resulting structure would in fact be the buckminsterfullerene.

12 pentagonal faces. It is these pentagons that supply the fullerene cage with its distinctive curvature, as without the presence of pentagons the hexagons would most likely form into a planar sheet (called graphene). While the pentagons are vital for the structure of the fullerene, they do bring with them an associated amount of strain energy. The positioning of the 12 pentagonal faces within the fullerene structure gives rise to a great amount of variation. The most stable fullerene structures are the ones that obey the isolated pentagon rule [37], for example, for 60 carbon atoms there are 1812 distinct ways (with the constraint that each vertex must have three faces) of arranging the carbon atoms within the fullerene, however, the only one that obeys the isolated pentagon rule is the C_{60} form shown in Figure 4.1.

4.1.1 The isolated pentagon rule

The isolated pentagon rule (IPR) is associated with the stability of a fullerene. The IPR states that the most stable fullerenes will be those where each pentagon is completely surrounded by hexagons (i.e. no pentagonal faces share an edge).

Placing pentagons close to one another is likely to lead to an increase in strain energy, especially localised on the carbon atoms that would be forced to be part of two or more pentagons.

The IPR is established both experimentally and theoretically, as all of the most common fullerenes obey this rule. However, that does not mean that fullerenes which ignore the IPR do not exist, as fullerenes exist in a variety of sizes, the smallest being C_{20}. The smallest fullerene that obeys the IPR is in fact the buckminsterfullerene, something that is not thought to be a coincidence, as it is the most frequently observed fullerene in experimental terms.

Kroto [38], who was among those who first discovered the molecule, argued that the strain for an isolated pentagon would be lower than two pentagons sharing an edge, and that the strain for three pentagons meeting at a vertex would be higher than both, and the strain would be even greater for a grouping of four pentagons.

4.2 Silicon surfaces

The main focus of our research (as shall be discussed in Chapters 5 and 6) is the interaction between single, multiple and endohedral variants of fullerenes, and the Si (100) surface, which is the chosen substrate. The bulk arrangement of silicon atoms is a diamond structure. However, in order to create a surface that the fullerenes can bond with this bulk periodicity must be broken. This means cutting the bulk silicon, which leaves the topmost atoms (now the surface atoms) with dangling bonds. These dangling bonds can cause instability with the surface atoms, so the surface atoms need to move around in order to remove this instability, and as a consequence lower the free energy of the system.

Following from previous computational studies [2, 14, 15, 16, 17] we have explored two surface reconstructions, and the schematics of the reconstructions, and energies per atom for these reconstructions are given in Figure 4.2 and Table 4.1 respectively. In the previous study [24] surface energies were calculated using

PLATO, and the results are shown in Table 4.1, where the most energetically favourable reconstruction is marginally the 2×2 tilted dimer reconstruction. For this reason this is the surface reconstruction that we have chosen to use for our calculations, however, the vast majority of other studies (including those discussed in Section 4.5) use the 2×1 tilted dimer reconstruction.

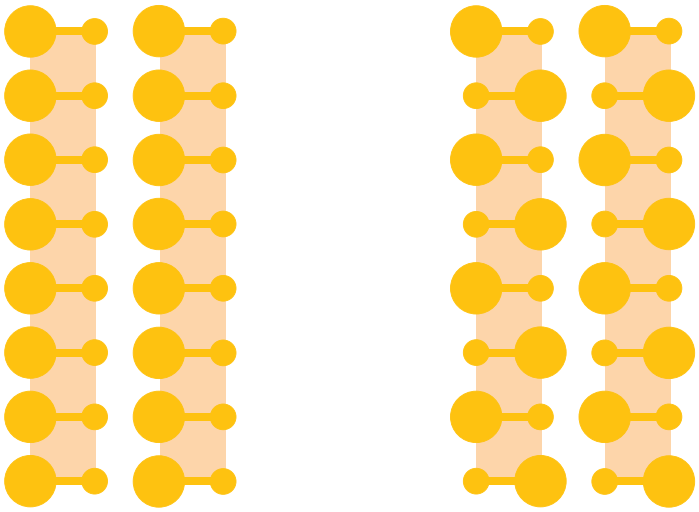

(a) 2×1 tilted dimer reconstruction

(b) 2×2 tilted dimer reconstruction

Figure 4.2: Schematic illustrations of the 2×1 and 2×2 tilted dimer reconstructions. Each diagram shows two dimer rows, with the row shown in pale orange. The atoms that are part of the surface dimers in the reconstruction are shown in yellow. The size of the circle used to represent the individual silicon atoms is indicative of the atoms' relative height, so the smaller circles represent atoms that are lower than the larger circles (atoms).

Surface Reconstruction	Surface energy (in Jm^{-2})
2×1 tilted dimer	0.121
2×2 tilted dimer	0.118

Table 4.1: The surface energies, in Jm^{-2}, for the two surfaces considered, the 2×1 and 2×2 tilted dimer reconstructions. These results are from the study by Frangou

When studying the adsorption of single C_{60} fullerenes on the Si (100) surface, most computational studies (including our own) utilise a near identical supercell of 128 atoms to represent the silicon surface. This relates to six layers of silicon atoms consisting of 96 atoms, and a final layer of 32 terminating hydrogen atoms. The bottom two layers of silicon atoms are always fixed in bulk positions, in order to approximate a larger bulk region. The hydrogen atoms are typically fixed in either relaxed positions or they are placed half-way along the Si-Si bonds that would exist if there was another layer of silicon atoms.

4.3 Fullerene orientations

Before looking at individual studies it is logical to first illustrate the different types of C_{60} bonding configurations to the Si (100) surface. The r1 grouping of configurations (see Figure 4.3) correspond to having the fullerene molecule positioned above the dimer row, and centred over a single silicon dimer.

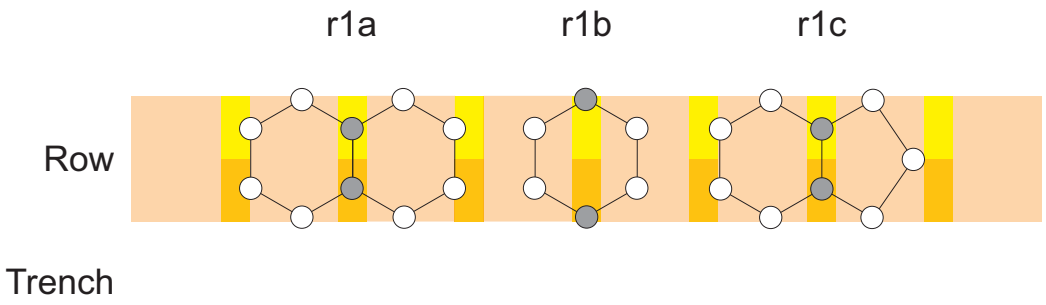

Figure 4.3: Pictured above are the three r1 configurations. The pale orange strips represent the dimer rows. The silicon dimers with which the cage bonds are represented by the yellow and orange bars; the yellow part represents one silicon atom of the pair, and the orange part represents the other silicon atom. The white region between the dimer rows represents the trench. Carbon atoms are depicted as white circles, with the exception of those which bond with the silicon surface which are depicted as grey circles.

The r2 grouping of configurations (see Figure 4.4) correspond to having the fullerene molecule positioned above the dimer row, and centred between two silicon dimers.

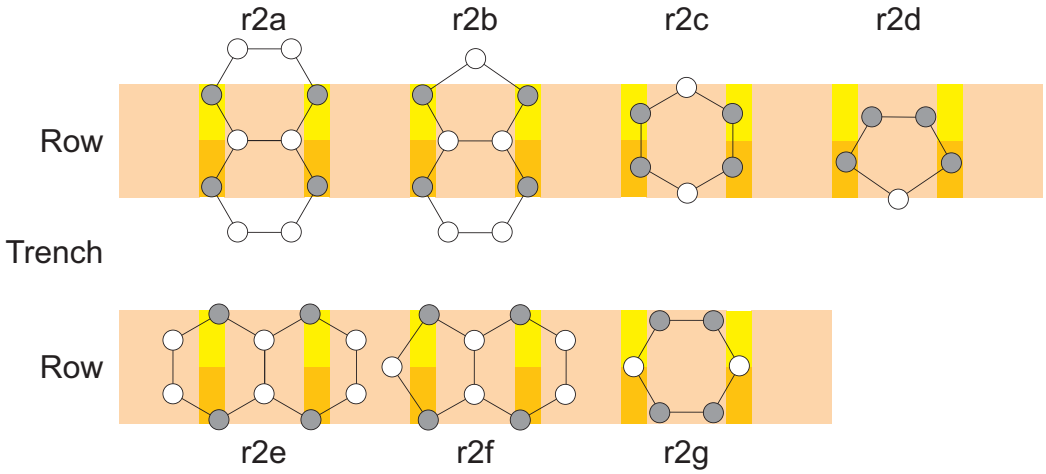

Figure 4.4: Pictured above are all the r2 configurations that have been investigated in this study. The colour scheme is the same as used in Fig. 4.3.

The t2 grouping of configurations (see Figure 4.5) correspond to having the fullerene molecule positioned above the trench (between the two dimer rows),

and centred between two silicon dimers (one from each dimer row).

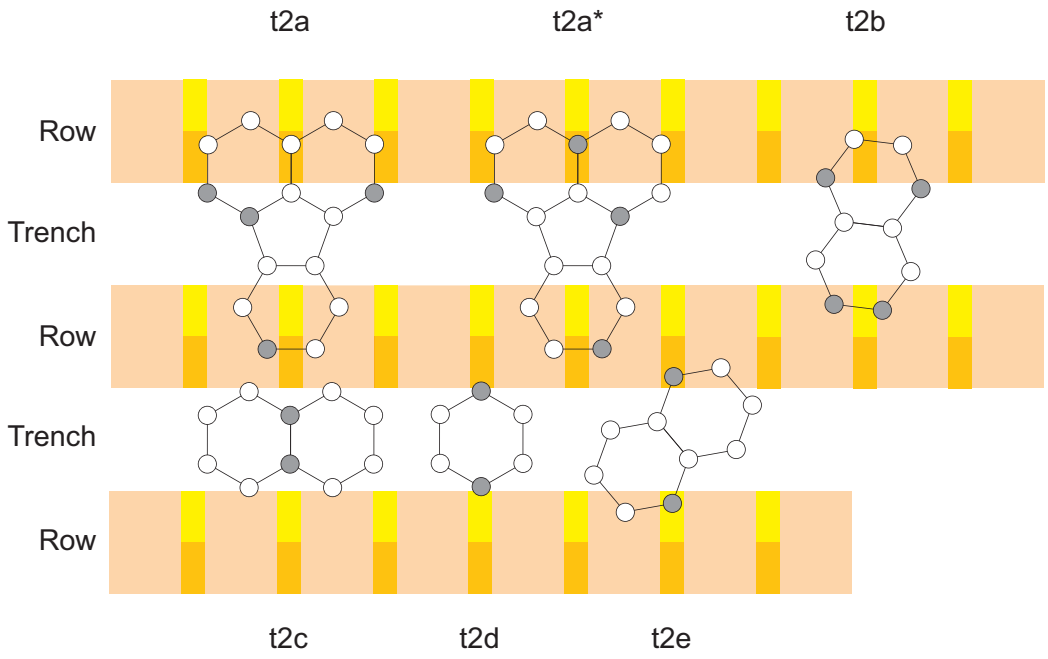

Figure 4.5: Pictured above are all the t2 configurations. The colour scheme is the same as used in Fig. 4.3.

The t4 grouping of configurations (see Figure 4.6) correspond to having the fullerene molecule positioned above the trench (between the two dimer rows), and centred between four silicon dimers (two from each dimer row).

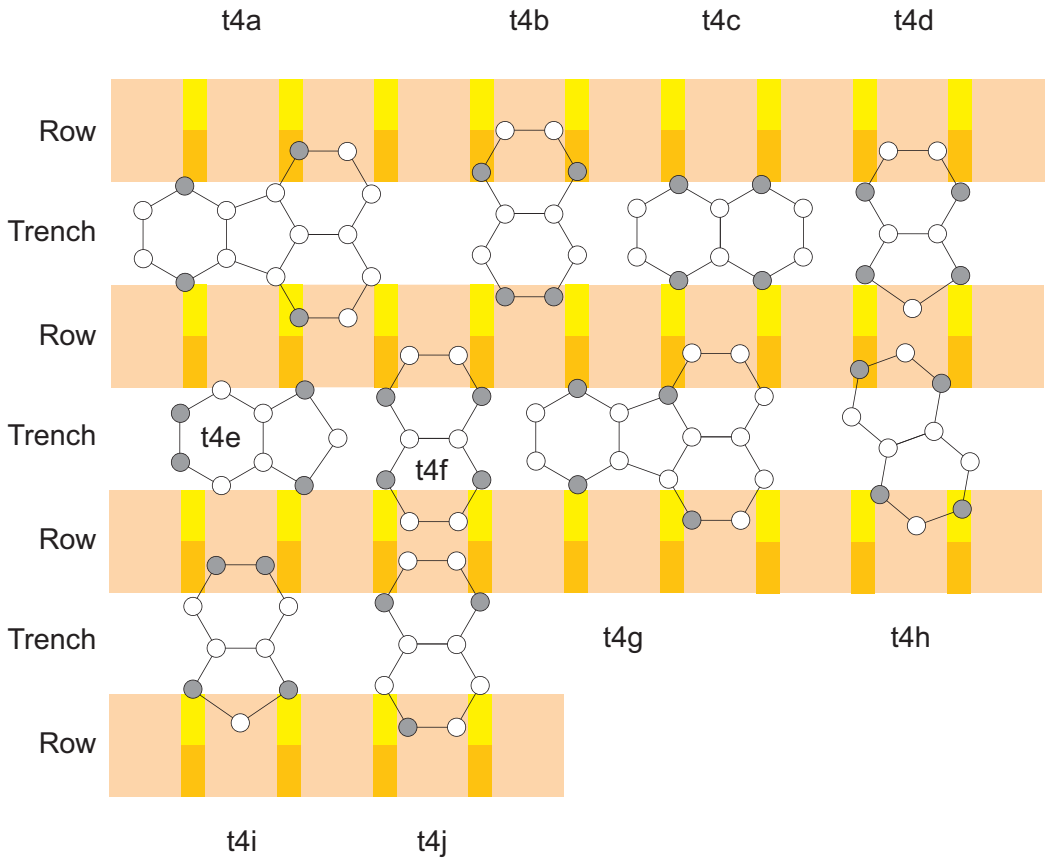

Figure 4.6: Pictured above are all the t4 configurations, some of which have been investigated in this study. The colour scheme is the same as used in Fig. 4.3.

All of the computational studies outlined in Section 4.5 implement selections of the above configurations, and this is also the case for the experimental studies outlined in Section 4.4 that make use of computational elements within the studies.

4.4 Previous experimental studies

Presented in this section are a selection of experimental studies that dealt with fullerenes, the manipulation of fullerenes, the creation of endohedrally doped nitrogen fullerenes, and the potential quantum computing applications of endohedral fullerenes.

4.4.1 C_{60}: Buckminsterfullerene

This study by Kroto *et al.* [1] is the most famous work on fullerenes, mainly because this is the study that actually discovered them. During experiments aimed at understanding the mechanisms by which long-chain carbon molecules are formed in interstellar space and circumstellar shells, a stable cluster of 60 carbon atoms was first observed. This was produced by vapourising graphite via laser irradiation. The study used a focussed pulsed laser to vapourise the carbon species from the surface of a solid disk of graphite into a high density helium flow.

The familiar truncated icosahedron shape was suggested for this new structure, as discussed in Section 4.1. The C_{60} molecule was shown to have all valences satisfied by two single bonds and one double bond, and this study suggested that the C_{60} molecule appeared to be aromatic[2]. The authors believed that the buckminsterfullerene was the only likely 60 carbon atom structure that would satisfy all valences.

In order to detect the C_{60} molecule the carbon structures were expanded in a supersonic molecular beam, the molecules were then photo-ionised using an excimer laser, and the fullerenes were detected by utilising time-of-flight spectrometry. Similar studies of carbon vapourisation had previously found clusters of up to 190 carbon atoms in size, and for clusters of greater than 40 constituent carbon atoms, only clusters consisting of even numbers of atoms were observed. The C_{60} molecule was consistantly the most frequently observed of all the fullerenes, in fact under optimum conditions, the C_{60} molecule was $\sim$ 40 times more prevalent than any other cluster.

The clustering conditions were outlined as first varying the delay between firing of the vapourisation laser and the helium pulse, and secondly increasing the time between vapourisation and expansion. These conditions were explained

[2]An aromatic structure is a ring-like structure that exhibits a stronger stabilisation than would be expected from the individual bonds formed. This is usually attributed to the circular nature, which allows the electrons to freely cycle around the structure.

by noting that in the laser vapourisation, fragments were torn from the surface as pieces of the planar graphite structure (the previously mentioned graphene, which is composed of fused six membered rings). When these pieces (the hot ring clusters) were left in contact with high density helium, the clusters equilibrated by two and three body collisions towards the most stable species (the C_{60}).

The study found the diameter of the C_{60} to be ~ 7 Å, which would provide an inner cavity capable of holding a variety of atoms. It was predicted that if a large scale synthetic process for creating the C_{60} molecules could be established, then the chemical and practical value of fullerenes could be extremely high. There are several important ramifications that follow from the suggested truncated icosahedron structure being correct, these are:

i) The stability of the molecule, even when formed under the most violent conditions, would suggest that these molecules may be widely distributed in the universe.

ii) As such these molecules may be a major constituent part of circumstellar shells with high carbon content.

4.4.2 Manipulation of C_{60} on a Si surface

This study, by Beton *et al.* [22], investigated the manipulation of C_{60} on a silicon surface via a STM. Previously studies had successfully manipulated adsorbate molecules across metallic substrates in low temperature environments [39]. Being able to extend this technique to include semiconductor surfaces and higher temperature environments was very desirable, in the hope that it could lead to the fabrication of a more diverse range of nanostructures. In this study the manipulation of C_{60} molecules via STM in order to form simple patterns was performed at room temperature on a Si (111) surface, which had undergone a 7×7 surface reconstrucion.

All the experiments were performed in an ultra high vacuum (UHV) environment. The 5 mm by 3 mm piece of Si (111) wafer was loaded into the

UHV system, outgassed at $\sim$ 800°C overnight, then heated to $\sim$ 1200°C for 60 seconds, annealed at $\sim$ 800°C for 3 minutes, and then slowly cooled. This procedure resulted in a 7×7 surface reconstruction with a low density of defects. Submonolayers of C_{60} were then sublimed[3] onto the sample: this was performed at room temperature. The final sample was transferred to the STM (which was also housed in a UHV chamber). The STM used electro-chemically etched tungsten tips, which were cleaned in UHV via electron beam heating. Under the STM it was possible to distinguish both the surface reconstruction and indivdual fullerenes.

Previously it had been demonstrated that moving the C_{60} molecules by performing a STM scan with the tip held close to the silicon surface and the feedback loop (which maintains a constant tunnel current) effectively turned off, was possible [40]. This study was unable to replicate these results without an unacceptably high rate of tip crashes. So, in order to achieve this study's objectives, the tip was moved in the following way (see Figure 4.7); first the tip was moved close to the surface by reducing the voltage (the sample was negative with respect to the tip), and then the current was increased. The tip was swept across the surface while maintaining the feedback loop. Tip retraction was achieved by adjusting the voltage and current values to those used for normal scanning purposes. The tip was then moved back to the original position while under feedback control.

This procedure was repeated across a number of parallel lines, separated by $\sim$ 0.6 nm, with the aim being to move the C_{60} molecules in the direction of the tip's movement. It often took many repeats of this sweeping procedure in order to move the molecule, and even when the molecule was moved, many times it would be displaced by a smaller distance (1 to 5 nm) than the tip displacement (greater than 6 nm). The success of the sweeping process was highly dependent on the tip used. Generally those tips with higher imaging resolution would

[3]Sublimation of an element or compound is the phase transition between the solid phase to the gas phase, without the intermediate liquid phase.

(a) STM tip moved closer to the surface to induce C_{60} movement

(b) STM tip removed and reset, in order to repeat tip sweeping movement

Figure 4.7: A schematic illustration of the process used to manipulate individual C_{60} molecules (shown in grey), on the silicon surface (illustrated as a yellow bar). In both of the diagrams, the initial tip positions are shown in pale blue, and final tip positions are shown in dark blue.

disrupt the silicon surface itself (by removing silicon adatoms), and fail to move the C_{60} molecules. Some tips were more successful than others, and this success rate varied over the tips' useful lifetime. Six out of the eight tips used in the study were successful in moving the C_{60} molecule.

In order to demonstrate the ability to manipulate C_{60} molecules, 12 C_{60} molecules were manoeuvred in order to create a crude "s" shape on the silicon surface. To achieve this took 40 movements of the C_{60} molecules (from the initial quasi-random positions), these movements in turn took $\sim$ 150 repeats of the sweeping procedure, and the total experiment took about four hours to perform; after which the silicon surface remained intact without any significant disruption.

Previous studies had shown serveral bonding configurations for the C_{60} on the Si (111) 7×7 surface, and for those configurations that some charge transfer did occur [41]. These experimental results illustrated that, while the interaction between the C_{60} molecule and the Si (111) surface was strong enough to stop

the molecules diffusing across the surface at room temperature, the bonding was weak enough in order to allow forced movement of the C_{60} molecule without significantly disrupting the surface. During the manipulation the C_{60} molecules were moving to favoured adsorption sites for that particular surface, and the molecules final orientation after movement was close to these low adsorption sites.

4.4.3 Bond breaking coupled with translation in rolling of covalently bound molecules

In this study, by Keeling *et al.* [12], both experimental work and *ab-initio* DFT calculations were performed in order to provide insight into the mechanisms involved in manipulating covalently bound C_{60} molecules on a Si (100) 2×1 surface. Previous work had shown that via STM tip manipulation, attractive, repulsive and sliding modes of lateral translation were possible [42]. These studies were performed with weakly bound adsorbates at low temperature conditions. At room temperature, however, many adsorbates are more strongly bound and the mechanisms of manipulation, particulary the role of bond breaking, had not been explored. This study aimed to rectify that by showing that the sequential breaking and reforming of the covalent bonds could result in the movement of the molecule, where rotation and translation result in a rolling motion.

For the experimental work the Si (100) 2×1 surface was prepared under UHV conditions, by annealing (1200°C for one minute) a 4 mm by 7 mm wafer. Submonolayer coverages of C_{60} were then deposited by sublimation. The STM was operated at room temperature within a UHV environment. The electrochemically etched tungsten tips were cleaned by electron beam heating, and used for both imaging and manipulation. From the STM imaging it was possible to see that the C_{60} molecules had chemisorbed at the centre of the trench, through the formation of C-Si covalent bonds (which was confirmed by *ab-initio* calculations).

The C_{60} was then manipulated along the trench via repulsive manipulation, as shown in Figure 4.8. This was achieved by positioning the tip above the trench, close to, but not directly above the target C_{60}. The tip was then lowered, by adjusting the tip current and sample voltage. The tip was then moved along the trench in increments, towards the fullerene molecule. As with previous studies the feedback control of the STM tip was maintained during manipulation.

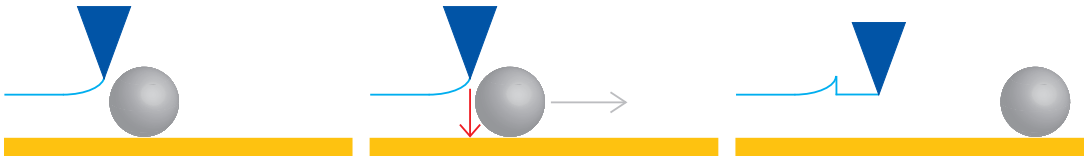

(a) STM tip approaching C_{60} on the surface.

(b) STM tip lowered towards surface, resulting in the C_{60} being repelled.

(c) STM tip continues moving towards the now displaced C_{60} molecule.

Figure 4.8: A schematic illustration of the repulsive manipulation of a C_{60} molecule (coloured in grey) along a silicon surface (shown as a yellow bar), via STM. The trace of the tip is shown as the pale blue tail following the tip (in dark blue).

The tip height was recorded during this procedure and was shown to demonstrate the molecular rolling characteristic (the tip trajectory showed a long range periodicity). For example, in one of the tip trajectories where the molecule was displaced over ~ 100 Å, the tip height, as a function of distance along the surface, had a periodicity equal to $4a_0$ (where a_0 is the lateral separation of the silicon dimers). Another tip trajectory again showed the $4a_0$ periodicity, however, some variation was noted with a periodicity of $3a_0$.

This periodic tip height variation indicated that the molecule moved through as many as four translational steps, each of a single lattice constant, before returning to an equivalent configuration to the intial one; this indicated a common mechanism responsible for lateral translation and the change in adsorption configurations. The study attributed this to a sequence of different C_{60} con-

figurations, and proposed a model for the rolling motion based on two of the four C-Si bonds acting as a pivot around which the fullerene rotates, as shown in Figure 4.9. This mechanism, in which a displacement of a_0 is accompanied with a change in orientation, had the fullerene starting in a four dimer site. As the molecule would be displaced from left to right, the leftmost two bonds were broken while the rightmost two bonds remained intact (acting as the pivot over which the molecule rolls). Two new bonds were formed between the fullerene and the surface, these were to the right of the pivoting bonds, which now became the leftmost bonds. This process would minimise the number of broken bonds during manipulation.

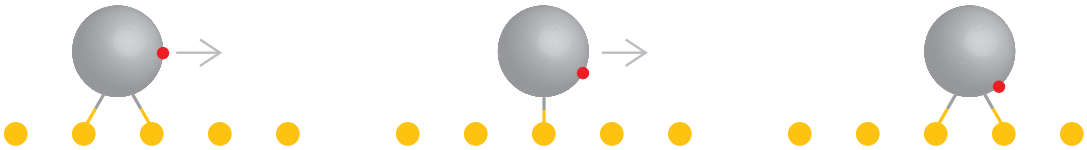

(a) The C_{60} in the initial t4 configuration

(b) The C_{60} in the pivot position

(c) The C_{60} in the final t4 configuration

Figure 4.9: Schematic illustration of the rolling mechanism for C_{60} manipulation. The fullerene is shown in grey, and the top level of atoms of the silicon surface are shown in yellow. The red dot C_{60} represents the carbon atom that is manipulated in the *ab-initio* calculations in order to induce movement. This is a 2 dimensional representation, so only the bonds on the nearest dimer row are present.

In order to test the proposed mechanism, in particular the coupling of rotation and translation of the molecule, extensive *ab-initio* calculations were performed. These were performed with the SIESTA package, using the same methodology as Hobbs *et al.* [15] (which will be discussed in Sub-Section 4.5.3). The work focused on the most stable configuration (the t4c configuration), and used a constrained minimisation technique to move the molecule along the trench. To do this, a single atom of the fullerene cage was constrained in terms of the atoms x-co-ordinate, while the atom was still free in both the y and z

directions (this is showed symbolically in Figure 4.9). The constrained atom was displaced by 0.05 Å in the direction of the molecule's intended movement, serving to move the molecule in small steps along the trench (after repeating the proccess many times).

The *ab-initio* calculations showed that as the molecule was displaced, the left-most two bonds were stretched, and the binding energy was also reduced. This bond stretching continued until the those bonds were broken. The molecule then adopted an intermediate state, where the C_{60} and the surface only possessed two C-Si bonds. This configuration was highly unstable to any lateral displacement, and the molecule subsequently underwent a transition to a new configuration (forming two new C-Si bonds with previously unbonded atoms). This new configuration that the C_{60} molecule positioned itself in was the t4g.

This process, of coupled translation and rotation, was continued in order to confirm that during a translational step of a_0 the molecule pivots over two unbroken bonds, where the pivot determines the possible transitions between configurations. They found for the intitial t4c configuration a sequence was observed as follows: t4c $\rightarrow$ t4g $\rightarrow$ t4b $\rightarrow$ t4g* $\rightarrow$ t4c (where t4g* represents a 180° rotation of t4g). This sequence had a periodicity of $4a_0$, as it corresponds to four translation steps and a 180° rotation of the molecule. Many other configurations and sequences that satisfied both the bond pivoting and a periodocity of $4a_0$ were found, however, no sequence with the periodocity of $3a_0$ was found.

It was proposed that the $3a_0$ sequence was a variation of the $4a_0$ sequence, in which an alternative configuration occured at one of the translational steps. In one of the examples it was noted that this alternative configuration was equivalent to two cage rotations; while another suggested possibility included the breaking of not two, but three or four C-Si bonds. It was concluded that the motion induced by the STM for the covalently bonded fullerenes was controlled by the bond breaking, which lead to a complex sequence of coupled rotational and translational dynamics.

4.4.4 Buckminsterfullerene C_{60}: a chemical Faraday cage for atomic nitrogen

This study, by Pietzak *et al.* [23], explored a new method for the efficient production of $N@C_{60}$, and the consequences of adding an exohedral atom to the $N@C_{60}$. Previous experimental work had showed that electropositive metal [43, 44] and noble gas atoms [45] could be encapsulated within the confines of a C_{60} fullerene, and a prior study [46] had explored a rather inefficient method of generating $N@C_{60}$. This method involved bombarding (from the side) of fullerenes, during deposition on a substrate, with low energy nitrogen atoms; however, both the implantation success rate and the quantity of $N@C_{60}$ produced were low.

The new method, which proved to be both simple and inexpensive, and only required basic laboratory equipment, produced the C_{60} and $N@C_{60}$ mixture in large quantities. In order to form the energetic nitrogen ions a glow discharge reactor was used. The experimental apparatus consisted of a quartz tube with two electrodes, which was continuely flushed with nitrogen gas (N_2). In the central part of the tube, which was surrounded by a furnace, a quantity of C_{60} powder was deposited. During operation, the glow discharge was on while the C_{60} molecules were sublimed and condensed on the water cooled cathode. This method produced 10 to 50 mg of soluble material, a mix of C_{60} and $N@C_{60}$ (albeit as only a fraction of the total material produced), after several hours of operation.

Using electron paramagnetic resonance (EPR) spectra analysis on $N@C_{60}$, there was sufficient evidence that the endohedral nitrogen atom was in the $S = \frac{3}{2}$ state, and that no charge transfer had occured. The absence of an electric field gradient indicated that the endohedral atom was located at the centre of the C_{60}. As part of this study, it was intended to investigate how the EPR features of the endohedral nitrogen atom would be affected by a distortion in the C_{60} cage. To achieve a controlled distortion of the cage, an exohedral atom

was added to the fullerene cage. This was only possible if the $N@C_{60}$ survived the reaction and initial conditions required for the addition of the exohedral atom, with the retention of the endohedral nitrogen atoms isolated nature being paramount.

In order to test this $N@C_{60}(COOEt)_2$ was created, for which they had a reliable production method, with good yields. It was shown that this addition to the fullerene cage caused a compression in one axis, and an elongation in the two remaining axes, which resulted in a droplet-like distortion of the fullerene cage. The EPR spectra analysis on $N@C_{60}(COOEt)_2$ provided some interesting results. Firstly, the reactivity of the $N@C_{60}$ and C_{60} molecules (in the context of attempting to create $N@C_{60}(COOEt)_2$) were the same, which demonstrated a lack of a significant interaction between the fullerene cage and the endohedral atom. Secondly, while in solution, the EPR spectrum of $N@C_{60}(COOEt)_2$ and the $N@C_{60}$ were similar, however for the $N@C_{60}(COOEt)_2$ in the solid, some new features appeared. The existing three lines in the EPR spectrum became broader, and there was an addition of at least four new lines. These additional lines were due to a fine structure, resulting from the interactions of the three unpaired electrons of the endohedral nitrogen atom. This fine structure was caused by the distortion of the fullerene cage, as the distortion resulted in the three *p*-orbitals of the nitrogen atom no longer being degenerate (which the study confirmed via semi-empirical quantum mechanical calculations).

In conclusion the study showed that the $N@C_{60}$ could be used as a probe to monitor the reaction from the addition of an exohedral atom. The endohedral nitrogen atom, which while usually extremely reactive towards covalent bond formation, did not undergo any chemical reaction with the fullerene cage. In addition it was shown that the endohedral nitrogen atom was prevented from undergoing a chemical reaction with the external environment. *Ab-initio* molecular orbital calculations showed that for both $N@C_{60}$ and $N@C_{60}(COOEt)_2$, there was no charge transfer between the endohedral nitrogen atom and the fullerene cage, and that the spin remained located only on the nitrogen atom. The study

also showed that the most energetically favourable situation for the endohedral nitrogen atom was to stay in the centre of the cage, and to avoid any chemical reaction.

4.4.5 Architectures for a Spin Quantum Computer Based on Endohedral Fullerenes

This study by Harneit *et al.* [5], discusses concepts for the construction of a quantum computer utilising the spin properties of endohedral fullerenes. Several experimental studies have demonstrated the feasibility of using endohedral fullerenes in such a device [47, 48], but were limited to a small number of qubits [49]. Indeed the scalability of the proposed quantum architectures of this type is still a major issue. The two most popular concepts (the first by Kane [50], and the second by Loss and DiVincenzo [51]) to solve the scalabilty problem are both based on an electric field controlling the exchange interaction between the electron spins of the endohedral atoms, which is easier said than done.

The endohedral species discussed were nitrogen and phosphorus, as both possess a total electron spin S = $\frac{3}{2}$. The four possible electron spin values, m_s = -$\frac{3}{2}$, -$\frac{1}{2}$, $\frac{1}{2}$ and $\frac{3}{2}$, give rise to four equidistant energy levels. The total spin system of the endohedral atom also contains the nuclear spin. The hyperfine interaction between the electron and nuclear spin splits every electron spin level into multiple sub-levels. There is no distortion or transfer of the electron spin density from the endohedral atom to the fullerene cage itself.

The endohedral atoms electron spin has a long lifetime, which is important for its potential application as a qubit for quantum computation. The spin-spin relaxation mechanism is, in the main, due to incoherent dipolar interactions with the electron spins of other endohedral fullerenes, meaning that this interaction could be controlled via careful architectural design. The spin-spin coupling between adjacent endohedrals depends only on the magnetic dipole interaction, as the exchange interaction between adjacent endohedrals, either by direct or

indirect (via the substrate) contact, is neglible. The nuclear spin system had been studied in less detail, as the only molecule studied (due to the difficulty in creating the others) is $^{14}N@C_{60}$, which has a low nuclear magnetic resonance sensitivity.

The ability to couple the endohedral spin system to external fields could lead to coupling control and the ability to read-out the qubit. One of the positive points to the concept put forward by Kane [50], is that it is a system of entirely local addressing, where the read-out is made possible by an external field. In general, the desire is to have an external field that is capable of controlling some parameter of the endohedral atom's spin Hamiltonian. This coupling to the external field must must not disturb the fragile spin system of the endohedral atom, so the field's strength would have to be carefully controlled. Experimental and computational studies [52] have shown that the electron system of the fullerene cage completely shields the endohedral atom from the electric field. So far the only effect that can possibly be controlled is the fine structure splitting of the electron spin resonance that is seen with distorted fullerene cages [53].

In order to actually build a molecular spin quantum register a chemical approach was favoured rather than a physical one. This is because of the relatively low thermal stability of the endohedral C_{60} molecules [54]; as for temperatures above $\sim 100°C$ the endohedral atom will start to form bonds with the fullerene cage, but being as this is below the sublimation temperature for fullerenes, physical structuring methods were impossible. Several chemical approaches to engineer molecular structures involving fullerenes have been developed, and as endohedral fullerenes are stable under chemical reactions (as long as these do not involve high temperatures) it was hoped that these approaches could be extended to produce the spin quantum register. The register could be a simple linear chain or a more complex chain involving multiple endohedral species at predetermined places throughout the chain.

The actual operation of the quantum register is also discussed, with the study assuming a perfect fullerene cage and the electron spin on the endohedral atom

as $S = \frac{1}{2}$. The local addressing of the register, consisting of identical endohedral fullerenes, could be achieved by applying a magnetic field gradient along the chain. Utilising only the electron spins does achieve the aim of a quantum register, however, the number of possible operations could be increased by using the nuclear spins as well. The nuclear spins could be used as a quantum memory, as the coherence time for the nuclear spins is longer than the electron spins, leaving the electron spins to be used as a working register only. This scheme has the added advantage, in that the dipolar interaction between electron spins could be decoupled, as long as the quantum information is stored in the nuclear spins. To achieve this a way of swapping information between the electron and nuclear spins is suggested. The method for reading out the information encoded in an endohedral atoms spin is lacking, as while methods have been proposed, experimentally the results have not been forthcoming.

The requirements of Quantum Cellular Automation (QCA) operation [55, 56], which requires neither local addressing nor interaction switching, could be met by the construction of spin pairs (AB-AB-...) or triplets (ABC-ABC-...). Using only spin pair chains would require four spins to encode one qubit, where as for the case of triplets, each spin corresponds to one qubit. In order to implement the QCA approach with endohedral fullerenes, the nuclear spins would have to be used as the qubits, and the electron spins as the bus between qubits.

The quantum register operation model developed within this study, requires several issues to be addressed experimentally before its physical realisation can be achieved. To begin with, the nuclear spin relaxation times require confirmation, and the proposed swapping operation between nuclear and electron spins was untested. The actual construction of the molecular spin quantum register had not been verified experimentally, and the distinct lack of the crucial single spin read out method remained to be resolved.

4.5 Previous computational studies

The following selection of computational studies explore the fullerene configurations outlined in Section 4.3, and provide a basis for our own research.

4.5.1 The structure of C_{60} and endohedral C_{60} on the Si (100) surface

The study, by Godwin *et al.* [2], of the adsorption of fullerenes on the Si (100) surface was performed using PLATO. The simulation cell created to represent the silicon surface in this study is the same as outlined in Section 4.2; the reconstruction implemented for the silicon dimers on the surface was the 2×1 reconstruction. This study employed basis sets that were of the DNP standard of basis set completedness.

The study looked at seven trench configurations, where the fullerene was centred between four silicon dimers. The first four of these configurations correspond to the t4a, t4b, t4c and t4d configurations outlined in Figure 4.6. These four configurations were stable after relaxation. The remaining three configurations were unstable, and during each simulation the fullerene would realign itself into one of the four configurations already outlined. The binding energies found for the four stable configurations were as follows: t4a = -5.7 eV, t4b = -5.3 eV, t4c = -5.0 eV and t4d = -4.9 eV.

The results showed that the charge transfer to the carbon atoms, that make up the C-Si bonds between the fullerene and the silicon surface, was ~ 0.1 of an electron. The length of these C-Si bonds were shown to all be between 1.95 Å and 1.98 Å, with the exception of the t4d configuration, where one of the C-Si bonds was found to be 2.03 Å, and another one of the bonds was 2.18 Å. The fact that these were from the t4d configuration was unsurprising as that was the least energetically favourable of all the stable configurations. The carbon atoms that formed C-Si bonds were originally all double bonded to one of their neighbours in the fullerene. The bond lengths for the C-C bonds that make up

the fullerene itself, all fell between 1.39 Å and 1.44 Å, where they were denoted as either single or double bonds respectively. These were different to the bond lengths found for pure single and double C-C bonds, so this indicated that some partial delocalisation had occured.

The study briefly looked at endohedral fullerenes, by studying the $N@C_{60}$ in the t4c configuration. The nitrogen atom was initially placed off-centre in the fullerene cage, and after relaxation the nitrogen atom was positioned slightly below the centre of mass of the relaxed fullerene cage. The endohedral nitrogen atom was found to be stable, with the spin decoupled from both the fullerene cage and the silicon surface, it also showed no sign of bonding with the fullerene cage.

4.5.2 Bonding sites and structure of C_{60} on the Si (100) surface

This study, by Godwin *et al.* [14], used the same methodology and basis sets as their previous study (as discussed in Sub-Section 4.5.1). Many other aspects of these studies are similar, with the charge transfers and bond lengths of the C-Si bonds found to be almost identical to those observed in the previous study. The main difference in this study was that a much greater range of fullerene configurations were explored; these configurations were grouped into four types according to the intial placement of the fullerene. When the fullerene was above the trench it was centred between either two or four dimers, corresponding to the t2 and t4 groups of configurations respectively. For the fullerene above the dimer row, the fullerene was centred between either one or two dimers, corresponding to the r1 and r2 groups of configurations.

Starting with the r1 configurations, three stable configurations were found, as shown in Figure 4.3. In all of these only two C-Si bonds were formed. The r1 configurations were shown to be unfavourable, in terms of binding energies, when compared to most of their r2 counterparts. The C-Si bond lengths, however,

were of a similar value.

This work found seven stable r2 configurations, all of which are shown in Figure 4.4. The r2e, r2f and r2g configurations are 90° rotations of the r2a, r2b and r2c configurations respectively. The C-C rebonding in these rotated configurations was found to be equivalent to the original configurations. The C-C bonds in the rotated configurations were, however, found to be weaker, making the rotated configurations less energetically favourable than the original ones. The average bond lengths for the C-Si bonds were found to be longer in the r2 configurations when compared to the t4 configurations.

This study found three stable configurations for the t2 configuration group, which are shown in Figure 4.5. The t2a configuration was found to bond to one dimer on one row, and three dimers on the other row, forming four C-Si bonds in total. This configuration in particular underwent significant and complex internal rebonding in order to form the C-Si bonds. The t2b configuration bonded to two dimers on one row, and one dimer on the other. This led to two carbon atoms bonding with the silicon atom, which resulted in longer and weaker C-Si bonds being formed. As with the t2a configuration, the internal rebonding in this configuration was quite complex, due to this odd arrangement. The third configuration, the t2c, was the only one that bonded to two dimers (one on each row), and such was found to be the least favourable in terms of binding energies (the t2a was the most favourable and the t2b fell in between the two).

For the t4 group of configurations they explored the t4a, t4b, t4c and t4d configurations, as shown in Figure 4.6. The major reason why these configurations were believed to be the most favourable, was because of the four strong C-Si bonds that were formed. The length and strength of these C-Si bonds was shown to be dependent on the level of internal rebonding within the fullerene. Again the t4d configuration was shown to be the least favourable of the t4 group of configurations, which in this study was attributed to the fact that it possessed the highest level of internal fullerene rebonding.

The row configurations were found to be less favourable than the trench configurations, which was attributed to the geometry of the system. The Si-Si dimer length is $\sim$ 2.16 Å, and the distance between adjacent dimers along the row is $\sim$ 3.84 Å. The distance across the trench between dimers on different rows, however, is $\sim$ 5.53 Å, which leads to more favourable C-Si bond angles when the fullerene is above the trench. The strains on the C-C and Si-Si bonds are much greater when the fullerene is above the dimer row, compared to the trench.

The study concluded that for the majority of configurations, the adhesion of the C_{60} molecule onto the Si (100) surface followed these two rules:

i) Sites where four C-Si bonds can be formed are more stable than those with only two C-Si bonds.

ii) The simpler the bond rearrangement within the C_{60} molecule, the more stable the resulting structure.

4.5.3 Adsorption of C_{60} on the Si (001) surface calculated within the generalized gradient approximation

This study, by Hobbs *et al.* [15], was performed by utilising the SIESTA DFT system, which is similar to PLATO. The simulation cell used was again the one outlined in Section 4.2, and the basis sets employed could be compared to the DNP basis sets within PLATO. Some of the configurations were also explored using the VASP program, which employs plane waves for basis sets instead of the linear combinations of atomic type orbitals basis sets used in both PLATO and SIESTA.

Initially the study explored different types of silicon surface reconstructions (the 2×1, 2×2 and 4×2 reconstructions). The 4×2 reconstruction was found to be slightly more favourable (by $\sim$ 0.03 eV) than the 2×2 reconstruction. With the VASP calculations this slight difference became negligible; the differences were found to be less than the overall precision of the DFT calculations, so it

became impossible to distinguish the 4×2 and 2×2 surface reconstructions in terms of system favourability. The 2×1 surface reconstruction was found to be the least favourable of the three (by both VASP and SIESTA calculations), however, this was the surface reconstruction chosen to be used for the calculations involving the adsorption of the fullerene molecules.

The r2a, t2c, t4a and t4b configurations, shown in Figures 4.4, 4.5 and 4.6 respectively, were studied within this work. Both the LDA and GGA exchange-correlation functionals were implemented within this study, and the results were found to be comparable to that of Godwin *et al.* [14]: for example, the C-Si bond lengths were within 3% of the other study. The minor differences were explained as being due to the slight differences with the basis sets and pseudopotentials used by the two studies.

In this study [15], the bottom half of the fullerene cage was found to have changed in terms of the actual C-C bond lengths, however, this change was never by more than 0.05 Å. In general, the results from this study were very similar to those of Godwin *et al.*, with the only real difference being the swapping of the t4a and t4b configurations in terms of binding energy favourability. The GGA was found to give smaller binding energies than the LDA. This was predicted as the LDA had been shown in the past to overestimate the binding energies. What was not predicted, was that the switch from LDA to GGA would also affect the ordering of the configurations in terms of system favourability.

4.5.4 An *ab-initio* study of C_{60} adsorption on the Si (001) surface

As with their study the previous year (as discussed in Sub-Section 4.5.3), this study by Hobbs *et al.* [16], again utilised SIESTA calculations and some medium precision VASP calculations. For the SIESTA calculations both the GGA and LDA energy functionals were implemented, and for VASP the GGA was used. The same silicon surface cell was used again (outlined in Section 4.2), with the

vacuum gap between the top of the fullerene and the bottom of the periodic surface repeat being $\sim$ 10 Å. Again, basis sets similar to the DNP basis sets in PLATO were employed, however, the Boys-Bernardi counterpoise method was employed in order to calculate the BSSE (as discussed in Chapter 2), and this correction was applied to the results.

The 4×2 and 2×1 silicon surface reconstructions were investigated, and it was found that the surface dimers could easily change orientation with an energy barrier of $\sim$ 0.1 eV. In order to explore the rebonding that took place within the fullerene cage upon adsorption to the silicon surface, the differences in charge densities were studied.

The configurations within the r1 and t2 groups (see Figures 4.3 and 4.5 respectively) were classed as metastable states. This was justified as these configurations possessed the smallest adsorption energies, and because creating the r1 and t2 configurations required precise placement of the fullerene, as anything else and the r1 and t2 configurations relaxed into the r2 and t4 configurations respectively. The calculations performed for the r1 and t2 configurations reflect this assumption, as these were only partially relaxed, as they would become unstable, and relax into the r2 and t4 configurations. The study was unable to recreate the t2a and t2b configurations due to their metastable nature, however, three new configurations were identified, namely the t2a*, t2d and t2e configurations. These metastable configurations were believed to represent intermediate configurations during molecular diffusion and manipulation.

As with previous studies the r2 (see Figure 4.4) and t4 (see Figure 4.6) groupings were found to be the most energetically favourable; these all formed three or four C-Si bonds, and were stable even if a minor displacement from their relaxed positions was induced. This study introduced six new t4 configurations, (t4e, t4f, t4g, t4h, t4i and t4j). The t4j configuration was the only t4 configuration that did not form four C-Si bonds with the surface, as it only formed three. This was thought to be due to the orientation of the surface dimers. The study found that it was possible to create stable configurations for the other t4 con-

figurations, where the orientation of one or more of the surface dimers had been flipped. This flipping of dimers would lead to the molecule being separated from the dimer by a sufficient distance so that no C-Si bond would be formed. While the resulting configuration may have been stable, it was unlikey to correspond to a local energy minimum.

The calculated binding energies were $\sim$ 1 to 1.5 eV lower with the GGA when compared to the LDA. The BSSE correction was found to further lower binding energies by an average of $\sim$ 1 eV. The authors believed that these BSSE corrected calculations from SIESTA provided quite reliable adsorption energies. The study was unable to precisely estimate the formation energy of individual C-Si bonds, as this depended very much on the initial level of bonding within the cage (that bonded with the surface), and the rebonding that took place within the cage upon adsorption to the surface. The GGA was found to lead to an increase in the bond length of the C-Si bonds by $\sim$ 0.04 Å when compared to the LDA. The rebonding within the C_{60} cage was believed to cost a significant amount of energy, and as such would have a large impact on the molecules binding energy.

4.5.5 Adsorption of C_{82} on Si (100)

In this study, by Frangou *et al.* [17], PLATO was used in order to perform the calculations, and both the GGA and LDA energy functionals were implemented. For carbon and silicon, basis sets of the TNDP level were employed. It was shown that the shift from DNP to TNDP basis sets could be very successful in eliminating the BSSE. The TNDP basis set results were comparable with those calculated with the DNP basis sets that had the BSSE correction applied. The TNDP results were more tightly bound, which corresponds with the possible over-correction of the counterpoise method. Bader bonding and charge analysis techniques were employed in order to study the systems.

The C_{60} systems utilised the conventional simulation cell (see Section 4.2) using a 2×1 surface reconstruction, except for a few cases where a 2×2 tilted

dimer reconstruction was implemented. These simulation cells contained almost twice the amount of vacuum ($\sim$ 19 Å) than previous studies [16]. For the C_{82}, an extended simulation cell was utilised in order to reduce the chance of periodic repeats interacting with one another. All the r2 and seven of the t4 configurations shown in Figures 4.4 and 4.6 were explored. The remaining t4 configurations (t4e, t4f and t4j) were not investigated.

There are nine isomers of C_{82} that obey the IPR, and as previous studies had shown the third isomer to be the most stable, this was the one the study focused on. The C_{82} molecule does not possess the symmetric bonding of the C_{60} molecule, so a greater variation in the bond energies and orders was found, and the distinction between the single and double bonds was almost non-existent. The only similarity, in terms of internal bonding, between the C_{82} and C_{60} was that the pentagons tended to be surrounded by bonds that were closer to single bonds. The C_{82}, because of its less uniform cage structure compared to the C_{60}, possesses unique regions of cage structure. The choice of bonding site on the fullerene was shown to have a large effect on the curvature of the cage in the bonding region. The study distinguised bonding regions by the quantity of pentagons within them.

The binding energies for the C_{82} were shown to be, in general, smaller than those for the C_{60}, implying that the C_{82} molecule interacts less strongly with the surface. The surrounding topology, however, was shown to affect the binding energies, although this was demonstrated to be inconsistent. Bader bond analysis showed a trend between the level of fullerene cage rebonding in the C_{82} molecule, and the strength of the interaction between the fullerene and the surface, which was consistent with the C_{60} results. There were some slight differences in the r2 and t4 configurations for the C_{82} molecule, such as the r2f configuration which only formed three C-Si bonds, and for the t4c configuration only two C-Si bonds were formed.

Using Bader charge analysis, a greater charge transfer was observed from the silicon atoms to the carbon atoms involved in the surface bonding, which was

typically found to be between 0.3 and 0.5 electrons (previously, results using Mulliken charge analysis showed a transfer of at most 0.1 electrons [2]). Unlike the C_{60} molecule, the C_{82} molecule was found to favour positioning above the dimer row, rather than the trench.

4.6 Conclusions

In this chapter, a wide selection of both computational and experimental previous studies have been reviewed. Through the computational studies it is possible to see the field of interest develop in terms of a few initial fullerene configurations, then broaden, where a much wider assortment of configurations were discovered and explored; and finally the interest narrowed and focussed on the most important configurations in much greater detail. The computational studies all took their cues from experimental studies, but the computational work allows for a much more precise experiment to be performed, beyond the current level of physical experiments.

The experimental studies discussed here deal with some topics that are sometimes taken for granted by researchers who exclusively perform computational work; for example, the actual creation of both fullerene and endohedral fullerene molecules. The experimental studies, while lacking the precision of their computational counterparts, have a great advantage in that performing operations such as fullerene manipulation, can be achieved experimentally in only a few mintues, and with relative ease. To replicate these manipulations within a computational study would require significant computational effort. The study by Keeling *et al.* [12], which was explored in Sub-Section 4.4.3, combined both experimental and computational work, with the findings from each supporting and validating the other approach. This study demonstrates the roles that both types of work can play, and how both experimental and computational studies can act together, complementing each other to give a fuller scientific understanding.

Chapter 5

C60 and N@C60 on Si surface

5.1 Introduction

The adsorption of the C_{60} molecule onto the Si (100) surface has been extensively studied with DFT [2, 14, 15, 16] . As the computing power available to these studies has increased, so has the completeness of the descriptions used for the atoms within the systems. These studies have found four groups of configurations for the C_{60} molecule upon the silicon surface (for further information on these see Chapter 4). The groupings are above the dimer trench, bonded to either two or four dimers (denoted as t2 and t4 respectively), and above the dimer row, bonded to either one or two dimers (denoted as r1 and r2 respectively). The most stable of the groups have been shown to be the r2 and t4 configurations, which are the focus of the work presented here.

Here we re-examine the r2 and t4 configurations, with a view to determining the effect on the endohedral nitrogen atom due to its placement within the C_{60} molecule on the Si (100) surface, and the effect on the C_{60} and the molecules bonding to the Si (100) surface due to the inclusion of the endohedral nitrogen atom. We compare our results for the adsorption of the C_{60} molecule onto the Si (100) surface, and then proceed to confirm that the effects on both the endohedral nitrogen atom and the C_{60} molecule are minimal.

5.2 Methodology

We have employed the DFT [27, 26] code PLATO [18] (as discussed in Chapter 2), which utilises a localised orbital basis set, for all our calculations. Within our calculations we have used the Perdew-Burke-Ernzerhof GGA [29] for the exchange-correlation potential, as the LDA has been shown to give binding energies that are unrealistically strong (it overbinds) for systems such as the ones studied here. The electron-ion interactions were modelled using pseudopotentials of the type described in [30].

5.2.1 Simulation surface

In order to describe the system of an isolated fullerene (or endohedral fullerene) on the Si (100) surface, we first had to create a silicon surface. The surface we have used consists of six layers of silicon atoms, with the surface layer being represented by two rows of four dimers. We have chosen a 2×2 tilted dimer reconstruction, as this has been shown to be energetically most favourable within our approach [15]. The bottom two layers of silicon are pinned in their respective bulk positions, and the bottom layer's dangling bonds are saturated with hydrogen atoms (which in turn have been pinned in their own relaxed positions). The simulation surface used for these calculations is given in Figure 5.1.

Periodic boundary conditions have been imposed in all directions, with a large vacuum gap included above the silicon surface, to ensure a sufficient gap (greater than 19 Å at all times) between the top of the fullerene cage and the bottom of the surface for the periodic repeat, so as to minimise the interaction between the two. Due to the size of the system, all the calculations have been carried out using just the Γ-point for k-point sampling.

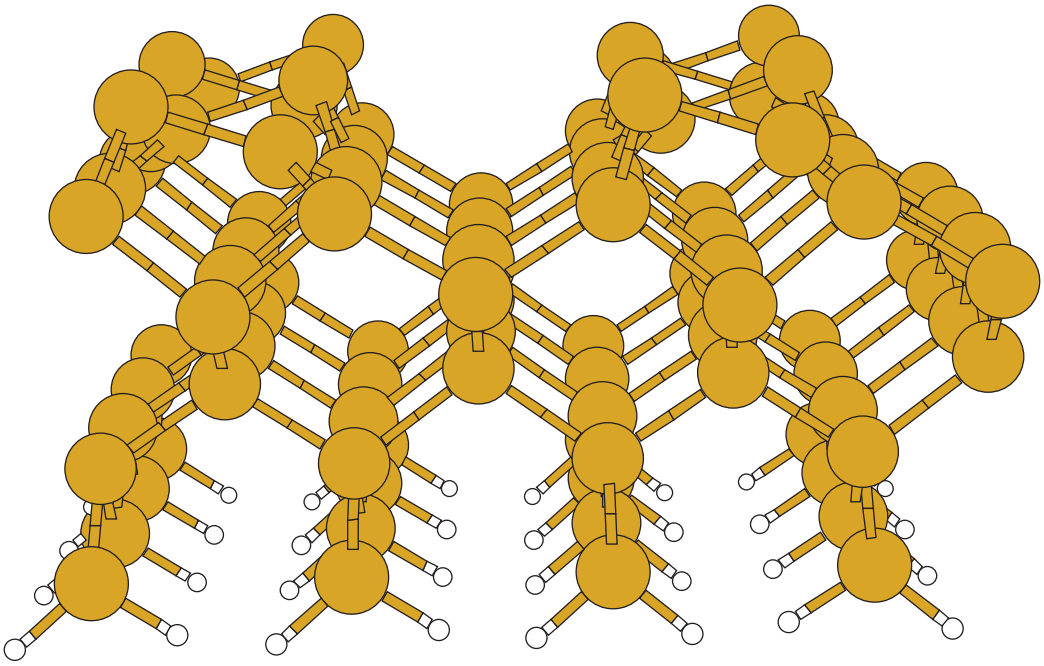

Figure 5.1: The 2×2 surface reconstruction of the simulation cell used in these calculations. The yellow circles represent the Si atoms (96 in total), and the white circles represent the H atoms (32 in total). The total number of atoms in the surface is 128.

5.2.2 Basis sets

In order to describe the differing atom species present in our simulation cell, we have created a series of basis sets that vary greatly in complexity. The simplest is our description of the hydrogen atoms, which we describe with a single s function. This is because the only purpose of the hydrogen atoms in our simulation cell is to saturate the dangling bonds from the final silicon layer, so a more complete description is not necessary. The silicon and carbon basis sets consist of three sets of s, three sets of p and two sets of d functions, which accounts for 22 basis functions per carbon and silicon atom. We denote these basis sets as triple numeric with double polarisation (TNDP). Using basis sets of the TNDP level of completeness has been shown [17] to reduce the basis set superposition error (BSSE), without the need to correct the results via the Boys

and Bernardi counterpoise method [31].

The endohedral nitrogen atoms contained within the fullerene cages, are described with three sets of s, three sets of p, two sets of d and one set of f functions, accounting for 29 basis functions per atom. We have denotated this basis set as TNDP+F. With the increasing number of basis functions there is of course an increased computational cost associated with the calculations. In order to accommodate the use of f-orbital functions within PLATO, we have implemented the generic Slater-Koster routines detailed in [20, 21] (and outlined in Chapter 3). This recursive approach allows us to employ basis sets containing basis functions with any angular component.

5.2.3 Binding energies

The commonly used measure of assessing the favourability of a specific orientation of the fullerene cage on the silicon surface, is the binding energy between the fullerene cage and the silicon surface. This is calculated as the difference between the sum of the energies of the relaxed components and the energy of the relaxed combined system (see Equation 5.1):

$$E_{\text{binding}} = E_{\text{fullerene on surface}} - E_{\text{isolated fullerene}} - E_{\text{isolated surface}} \tag{5.1}$$

The binding energies from our calculations not only allow comparison between our work and previous studies, but provide a measure of difference between the fullerene and the endohedral fullerene configurations.

5.2.4 Bader analysis

To analyse the bonding and the charge transfer in the systems, we have used the algorithm devised by Sanville *et al.* [32], that implements Bader's principles from his atoms in molecules work [33]. As previously discussed in Chapter 2, the ratio of the two negative eigenvalues provides a measure of the bond's characteristic. In particular it indicates how much p characteristic the bond possesses (which

corresponds to an elongation of the circular shape of the perfect single bond). As a reference we use the single and double bonds found in ethane and ethene, which have bond ratios of 1.00 and 1.27 respectively. Bonds which have ratios between the two values are considered as having some interaction between the p-orbitals of the constituent atoms. For the isolated C_{60} we see two distinct bond types that fall between these perfect bond ratios. The weaker type of bonds are found around the pentagons, and have a ratio of ~ 1.13 and the stronger type of bonds, which are the bonds shared by hexagons, have a ratio of ~ 1.19. Bader's method also allows the charge on atoms to be calculated, independent of the basis set, for a given charge density, which is not the case with the often used Mulliken population analysis.

5.3 Results

Previous studies [2, 14, 15, 16] involving the adsorption of fullerene molecules onto silicon substrates have identified four groups of configurations that the cage can take upon the surface. In this research we focused on the two of these groups that produced the most stable structures. These are those with the cage above the dimer row, centred between two dimers (r2), and with the cage above the dimer trench, bonded to four dimers (t4). We replicated all of the structures identified in [14] and the more stable structures identified in [16]. Examples of the r2a and t4c configurations of the C_{60} and the $N@C_{60}$ on the simulation surface are given in Figures 5.2 and 5.3 respectively.

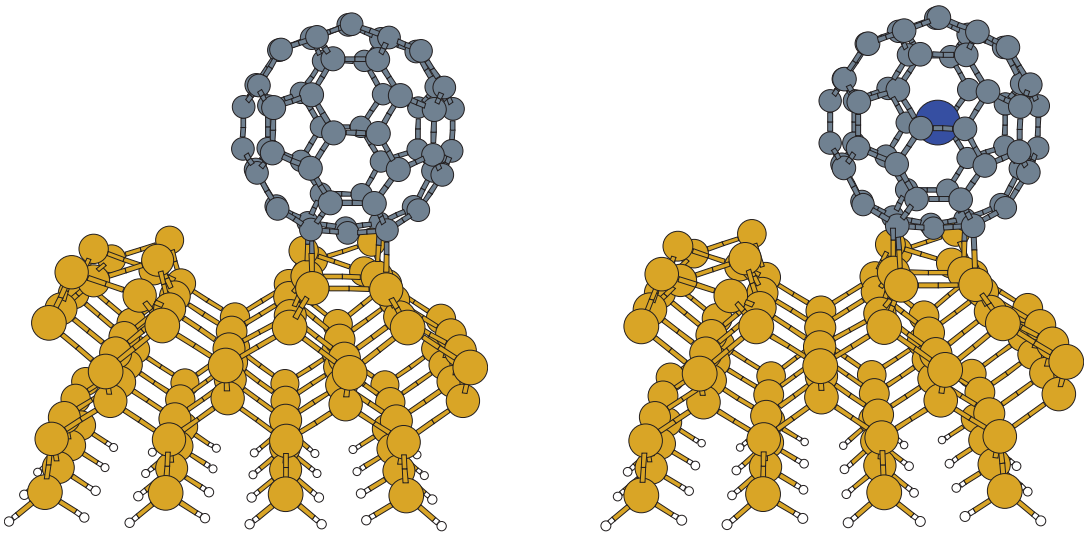

(a) C_{60} (b) $N@C_{60}$

Figure 5.2: An example of the r2a configuration for both the C_{60} and the $N@C_{60}$. Note how the two dimers that form the C-Si bonds are almost flat, and have lost the alternating tilting nature of their neighbours.

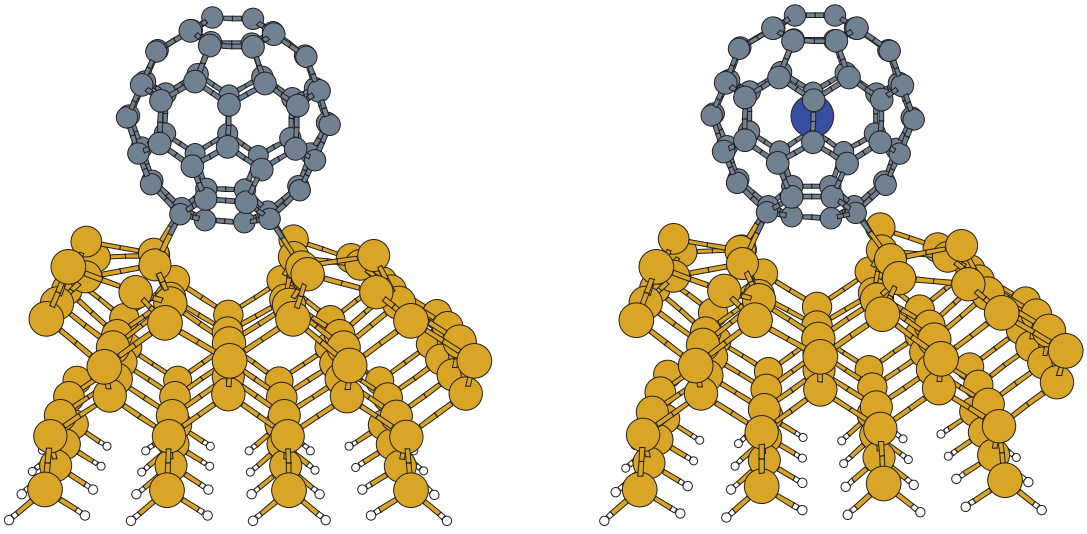

(a) C_{60} (b) $N@C_{60}$

Figure 5.3: The t4a configuration for both the C_{60} and the $N@C_{60}$. Note how the dimers on the silicon surface differ from those in the isolated surface (see Figure 5.1), due to the adsorption of the fullerene.

5.3.1 Binding energies

The results we have produced for the adsorption of the C_{60} on the Si (100) surface are given in Table 5.1; they show a good level of agreement with previous studies.

Config.	SIESTA [16]	VASP [16]	Godwin [14]	Frangou [17]	C60	N@C60
r2a	-2.58	-2.78	-4.83	-3.02	-3.23	-3.19
r2b	-2.49	N/A	-4.33	-2.72	-3.01	-3.08
r2c	-2.00	N/A	-4.15	-2.85*	-2.82	-2.92
r2d	-0.87	N/A	-2.69	-1.29	-1.52	-1.56
r2e	-1.68	N/A	-3.94	-2.16	-2.21	-2.28
r2f	-2.19	N/A	-4.10	-2.32	-2.60	-2.66
r2g	-1.10	N/A	-3.13	-1.42	-1.89	-2.11
t4a	-2.16	-2.45	-5.71	-2.77	-2.84	-2.90
t4b	-2.53	N/A	-5.31	-3.15*	-3.14	-3.18
t4c	-2.63	-2.75	-4.96	-3.02*	-3.14	-3.19
t4d	-1.96	N/A	-4.85	-2.32	-2.40	-2.64
t4g	-2.53	-2.74	N/A	-2.78*	-2.77	-2.82
t4h	-1.94	N/A	N/A	-1.87*	-2.52	-2.55
t4i	-1.83	N/A	N/A	-2.45*	-2.41	-2.49

Table 5.1: Binding energies of the isolated C_{60} and N@C_{60} molecules on the Si (100) surface in eV. For comparison, the results of previous calculations are given. The results from the SIESTA program used a basis set equivalent to our DNP basis sets, however, they include the Boys-Bernardi correction (as discussed in Chapter 2) to correct for the basis superposition error associated with basis sets of this level of completeness. Both Godwin and Frangou used PLATO, with basis sets of DNP and TNDP used respectively. The results marked by a * indicate that the 2×2 surface reconstruction was used, otherwise the 2×1 surface reconstruction was used. Our results, the C_{60} and N@C_{60} columns, all use the 2×2 surface.

There are some subtle differences, for example our r2 configurations are in

general more favourable than previously shown. We attribute this to two factors; the first relates to the differences between the surface reconstructions used, and the second being the ease at which the fullerene forms stable bonds with the silicon surface. In general the binding energy is more favourable when the two dimers directly underneath the fullerene molecule (the dimers that the fullerene bonds to) are flat (i.e. as the angle of the tilted dimer reconstruction tends to zero). For the r2d configuration we produced a range of relaxed systems, all using the 2×2 surface reconstruction, that differed only in the measure of flatness of the dimers with which the cage bonds. In this case a difference of $\sim$ 0.03 Å in the amount of dimer flatness, accounted for a difference of $\sim$ 0.3 eV. Considerable efforts have been taken to ensure that the dimers are as flat as possible in the r2 configurations. The 2×2 surface reconstruction appears to be much more likely to naturally relax into this type of dimer configuration than the 2×1 surface reconstruction, as shown in Figure 5.4. This leads to the second factor, which is the existence of many metastable states for the C_{60} molecule on the Si (100) within any one configuration. Thus, it is very difficult to determine with any degree of certainty the global minimum.

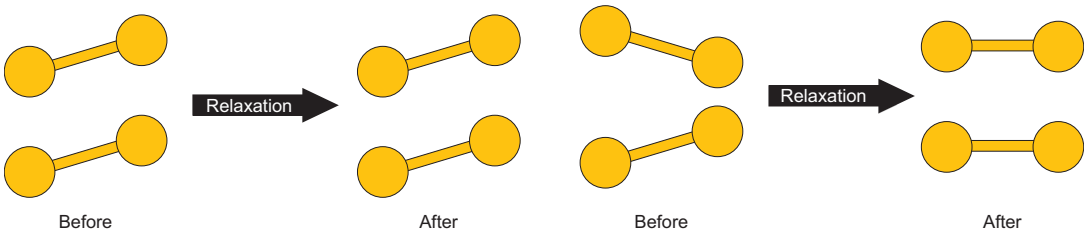

(a) 2×1 surface (b) 2×2 surface

Figure 5.4: Schematics showing the two dimers that form the fullerene bonding site, before and after system relaxation. These correspond to the r2 group of configurations only.

The final relaxed configurations for the adsorption of the C_{60} molecule on the Si (100) surface were used for the initial atom positions in the N@C_{60} calculations. The nitrogen atom was added into the fullerene cage at the centre of

mass for the fullerene. The endohedral systems were then relaxed in the same manner, and the binding energies calculated are also presented in Table 5.1. The total energy of the isolated $N@C_{60}$ is substituted in Equation 5.1 instead of the energy for the isolated C_{60}. As Table 5.1 demonstrates there is very little change in the binding energies between the C_{60} and $N@C_{60}$ systems for all of the configurations investigated. In general, the $N@C_{60}$ configurations are marginally more favourable than their C_{60} counterparts. There are two outlying results, those for the r2g and t4d configurations, which we shall directly address in the subsequent discussion, explaining these results in the context of subtle differences within other system properties. As a whole we believe our results are consistent with the consensus that the endohedral nitrogen is almost perfectly isolated within the fullerene cage.

5.3.2 Hierarchies

If we compare the hierarchies of the most favourable configurations from this work with that of previous studies there is a good level of agreement, see Table 5.2. The less stable configurations are those most closely in agreement between the studies. Our results show a slight skew in favourability towards the r2 configurations, as explained previously; however, in general these differences are minor. The subtle differences between the hierarchies of our C_{60} and $N@C_{60}$ work illustrates the small, but varying differences, between the systems as discussed later.

Rank	SIESTA [16]	Frangou [17]	C60	N@C60
1	t4c	t4b	r2a	r2a / t4c
2	r2a	t4c / r2a	t4b / t4c	r2a / t4c
3	t4b / t4g	t4c / r2a	t4b / t4c	t4b
4	t4b / t4g	r2c	r2b	r2b
5	r2b	t4g	t4a	r2c
6	r2f	t4a	r2c	t4a
7	t4a	r2b	t4g	t4g
8	r2c	t4i	r2f	r2f
9	t4d	t4d / r2f	t4h	t4d
10	t4h	t4d / r2f	t4i	t4h
11	t4i	r2e	t4d	t4i
12	r2e	t4h	r2e	r2e
13	r2g	r2g	r2g	r2g
14	r2d	r2d	r2d	r2d

Table 5.2: The fourteen configurations investigated here are placed in the table above in descending order of stability.

5.3.3 Nitrogen spin

A good measure to determine how well the endohedral nitrogen atom is isolated, is to observe the change in spin on the nitrogen atom. This is acheived by comparison of the spin on the nitrogen atom in each of the endohedral configurations with the spin on the nitrogen atom in the isolated $N@C_{60}$. We have calculated the spin using two different schemes, the Mulliken spin and the Bader spin, see Table 5.3. The Mulliken spin analysis for the nitrogen atom in an isolated $N@C_{60}$ gives a spin value of 1.48. With the exception of the r2g configuration, which gives a spin value of 1.38, all the spin values for the adsorbed configurations range from 1.44 to 1.47, which represents a very small change in the level

of electron spin.

With the Bader analysis the picture is a little different, as we see greater variation in the spin values. The spin on the nitrogen atom in the isolated $N@C_{60}$, using Bader analysis, has a value of 1.43, and the spin values for the adsorbed fullerene systems range from 1.33 to 1.43. In context of only the r2 configurations, the r2g configuration remains an outlier. There is, however, much greater variation within the t4 configurations than was present in the Mulliken analysis. There appears to be no direct correlation between change in spin and the change in binding energy between the C_{60} and $N@C_{60}$ configurations. In both the Mulliken spin and the Bader spin the maximum difference between the isolated case and any of the endohedral configurations is ~ 0.1, which is well within reasonable expectations for an isolated endohedral species.

Config.	Mulliken Spin	Bader Spin
r2a	1.46	1.42
r2b	1.46	1.42
r2c	1.44	1.40
r2d	1.47	1.41
r2e	1.45	1.42
r2f	1.46	1.42
r2g	1.38	1.35
t4a	1.46	1.33
t4b	1.47	1.43
t4c	1.46	1.43
t4d	1.47	1.43
t4g	1.46	1.34
t4h	1.45	1.36
t4i	1.44	1.33
Isolated N@C60	1.48	1.43

Table 5.3: Analysis of the spin on the endohedral nitrogen atom. The pairs of results are from the same system with only the spin calculation method differing.

5.3.4 Charge transfer to Nitrogen atom

When studying the charge on the nitrogen atom in the $N@C_{60}$ configurations, see Table 5.4, it is clear that there is very little charge transfer between the nitrogen atom and the fullerene cage. In the main the charge transfer to the nitrogen atom is less than 0.1 of an electron, with only a couple of outlier cases, the largest being ~ 0.28 of an electron. There does not appear to be a direct relationship between charge transfer and system favourability, however again we find the r2g configuration amongst the outliers. We believe that the larger shift in the r2g binding energy for the $N@C_{60}$ from the C_{60}, when compared to the

other configurations, is the result of the greater charge transfer to the C_{60} cage containing the endohedral nitrogen atom.

Config.	Total charge on N Atom
r2a	-0.01
r2b	-0.02
r2c	-0.08
r2d	0.06
r2e	-0.05
r2f	-0.01
r2g	-0.17
t4a	0.28
t4b	-0.03
t4c	-0.04
t4d	-0.02
t4g	0.26
t4h	0.16
t4i	0.21
Isolated N@C60	0.07

Table 5.4: Bader charge analysis of the charge on the endohedral nitrogen atom, in the various endohedral fullerene configurations.

5.3.5 Nitrogen displacement within the fullerene cage

A previous study [2] of endohedral fullerenes that used nitrogen as the endohedral species, found the nitrogen atom in its final relaxed position to be a little below the centre of the fullerene cage. This calculation was performed for the t4c configuration. A further difference between their calculation and our own is that we differ on the initial placement of the nitrogen atom. In their calculations it was placed off-centre, whereas as previously stated, in our calculations

we have initially placed the nitrogen atom at the centre of mass for the fullerene cage. This minor difference aside, for the t4c configuration we also found that the largest displacement for the nitrogen atom would be in the negative z-axis (i.e. the nitrogen atom moves towards the surface).

As Table 5.5 shows, there appears to be little in the way of correlation between the magnitude and direction of the displacement of the nitrogen atom, and the binding energy of the $N@C_{60}$ or the spin lost on the nitrogen atom. The magnitude of all the displacements are small, with all being ≤ 0.1 Å, the only exception being the t4b configuration with a displacement ~ 0.3 Å. In fact, by visually analysing the configurations, it is only the t4b configuration (which has not only the largest displacement magnitude, but the displacement is almost all in the one axis), in which the nitrogen displacement is noticeable.

Config.	X-axis	Y-axis	Z-axis	Magnitude
r2a	0.07	-0.09	-0.01	0.12
r2b	-0.06	0.10	0.00	0.12
r2c	-0.14	0.18	0.01	0.12
r2d	0.04	-0.01	-0.08	0.09
r2e	-0.10	0.01	0.04	0.11
r2f	-0.07	-0.08	-0.01	0.10
r2g	-0.01	0.10	-0.01	0.10
t4a	0.02	-0.01	-0.01	0.02
t4b	-0.06	-0.09	-0.29	0.31
t4c	-0.01	0.10	-0.12	0.16
t4d	-0.01	-0.00	0.09	0.09
t4g	0.07	-0.03	-0.01	0.08
t4h	-0.00	0.00	-0.06	0.06
t4i	0.01	-0.00	-0.01	0.01

Table 5.5: Displacements of the endohedral nitrogen atom, from the centre of mass of the relaxed fullerene cage. All results are given in Å.

5.3.6 C-Si bonding

When comparing the lengths of the carbon-silicon bonds that are formed between the fullerene cage and the silicon surface, see Table 5.6, there is good agreement to be found between not only the C_{60} and $N@C_{60}$ results, but those results found by Godwin *et al.* [14]. There appears to be no pattern concerning differences in bond length between the C_{60} and $N@C_{60}$ systems of the same configuration. It is when examining the carbon-silicon bonds that we are able to explain the increase in binding energies found between the $N@C_{60}$ t4d, and the C_{60} t4d configurations. The $N@C_{60}$ t4d configuration is a metastable minimum, with shorter carbon-silicon bond lengths than those found in the C_{60} t4d configuration. It is only the presence of the endohedral nitrogen atom that provides this stability, as the removal of the nitrogen atom leads to the fullerene and surface relaxing into the form found for the C_{60} t4d configuration. This is the only case where the presence of an endohedral nitrogen atom has affected bonding, and is a direct product of the unfavourabilty of the 2×2 surface reconstruction for the t4d configuration, especially for this small cell size. This unfavourability is demonstrated in Figure 5.5, where the final relaxed structures of the t4d fullerene configuration are shown for both the 2×1 surface reconstruction and the 2×2 surface reconstruction.

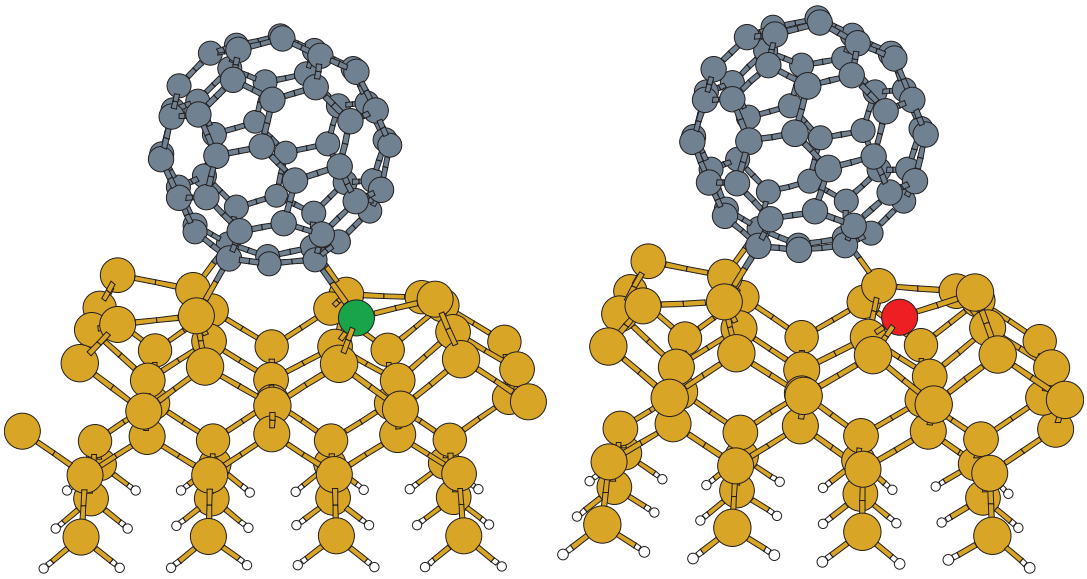

(a) 2×1 surface (b) 2×2 surface

Figure 5.5: Visualisations of final relaxed configurations for the t4d configuration. The red and green atoms highlight the silicon atom in the C-Si bond that is affected by the surface reconstruction used. In order to give a clear view of the relevant C-Si bonding, portions of the surface have been removed.

All previous studies for this configuration predict that one of the four C-Si bonds will be much longer than the other three. The silicon atom which is part of this bond is coloured green in the 2×1 surface, and has a length $\sim$ 2.4 Å. However with the 2×2 surface this weak bond is not strong enough to overcome the silicon surfaces attempt to revert to the 2×2 reconstruction. This silicon atom is coloured red, and the length of the C-Si bond in this case is $\sim$ 2.7 Å. The energy barrier for a dimer to flip its orientation is $\sim$ 0.1 eV, so even if you try and force the orientation of a dimer, the dimer will just re-orientate itself, as it wants to be. In the N@C_{60} t4d configuration the length of this longer bond is reduced slightly, which may contribute to the change in the binding energies between this case and its C_{60} t4d counterpart.

For the remainder of the configurations the range of bond lengths is greater in our results (1.93 to 2.19 Å) compared to those presented elsewhere (1.96 to

2.19 Å), however, this difference is minimal. The more favourable binding energy (compared to other results), as shown in Table 5.1, for the r2a configuration may be explained by the fact that it has a much lower average carbon-silicon bond length. In general, however, the carbon-silicon bond length does not seem to have a direct relationship with binding energy.

Config.	Godwin [14]	$\bar{x}$	C60	$\bar{x}$	N@C60	$\bar{x}$
r2a	1.96, 1.97, 1.98, 1.98	1.97	1.93, 1.93, 1.94, 1.94	1.94	1.93, 1.94, 1.94, 1.94	1.94
r2b	1.97, 1.98, 2.02, 2.02	2.00	1.95, 1.97, 2.04, 2.11	2.02	1.95, 1.97, 2.03, 2.11	2.02
r2c	2.01, 2.02, 2.03, 2.07	2.03	2.00, 2.02, 2.05, 2.08	2.04	2.00, 2.03, 2.05, 2.08	2.04
r2d	2.00, 2.01, 2.01, 2.02	2.01	1.99, 2.01, 2.02, 2.04	2.01	1.99, 2.01, 2.01, 2.03	2.01
r2e	1.99, 1.99, 1.99, 1.99	1.99	1.95, 1.96, 1.97, 1.98	1.96	1.95, 1.96, 1.98, 1.98	1.97
r2f	1.97, 1.99, 2.02, 2.04	2.01	1.94, 1.96, 1.97, 2.14	2.00	1.95, 1.96, 1.97, 2.15	2.01
r2g	2.03, 2.03, 2.03, 2.07	2.04	2.03, 2.05, 2.05, 2.07	2.05	2.01, 2.03, 2.04, 2.06	2.04
t4a	1.93, 1.94, 1.95, 1.98	1.95	1.95, 1.95, 1.96, 1.99	1.96	1.95, 1.95, 1.96, 1.99	1.96
t4b	1.95, 1.96, 1.98, 1.98	1.97	1.95, 1.96, 1.98, 1.99	1.97	1.96, 1.96, 1.98, 1.99	1.97
t4c	1.96, 1.96, 1.96, 1.98	1.97	1.99, 2.00, 2.01, 2.01	2.00	1.99, 2.00, 2.01, 2.02	2.01
t4d	1.97, 1.97, 2.03, 2.19	2.04	1.96, 1.98, 2.01, 2.73	2.17	1.96, 1.97, 2.02, 2.70	2.16
t4g	N/A	N/A	1.92, 1.95, 2.00, 2.06	1.98	1.92, 1.95, 2.00, 2.06	1.98
t4h	N/A	N/A	2.00, 2.03, 2.06, 2.24	2.08	2.00, 2.03, 2.06, 2.25	2.08
t4i	N/A	N/A	2.01, 2.03, 2.04, 2.15	2.06	2.01, 2.03, 2.04, 2.15	2.06

Table 5.6: Bond lengths and average bond lengths of the C-Si bonds formed, for the orientations of C_{60}, N@C_{60} and the Si surface, all results are given in Å.

5.3.7 Internal fullerene rebonding

We have used Bader bonding analysis in order to investigate the bond ratios within the fullerene cage. We used this approach for both all the C_{60} configurations and their N@C_{60} counterparts, and the analysis of these is given subsequently. We looked at the rebonding that took place in the bottom part of the fullerene cage (the area which bonded with the surface), as this is where the majority of change should be located. For the sake of simplicity, the analysis is split up into four types of configuration, depending on the nature of the cage immediately around the bonding region.

Type 1

The type 1 configurations have two adjacent hexagons in the immediate vicinity of the cage's bonding region with the surface. The three configurations that have the symmetrical middle placement of bonding atoms, the r2a (see Figure 5.6(a)), r2e (see Figure 5.6(b)) and t4c (see Figure 5.6(d)), all show similar patterns of localised rebonding. Primarily the weakening of the stronger (double) bonds around the bonding atoms, the less significant (in terms of magnitude) weakening of the weaker (single) bonds around the bonding atoms, and the very significant strengthening of the highlighted bonds.

The t4b configuration (see Figure 5.6(c)) shows a slight deviation from the rebonding pattern shown in the previous configurations, which corresponds to the difference in bonding atoms between the two configurations. This causes a larger quantity of rebonding to take place in the upper hexagon. This effect is even more pronounced in the t4h configuration (see Figure 5.6(e)), where the non-symmetrical configuration of bonding atoms, changes the rebonding arrangement even further. As seen in the t4b case the movement of bonding atoms away from the middle positions (found in the r2a, r2e and t4c cases) causes a significant change in the rebonding around these atoms.

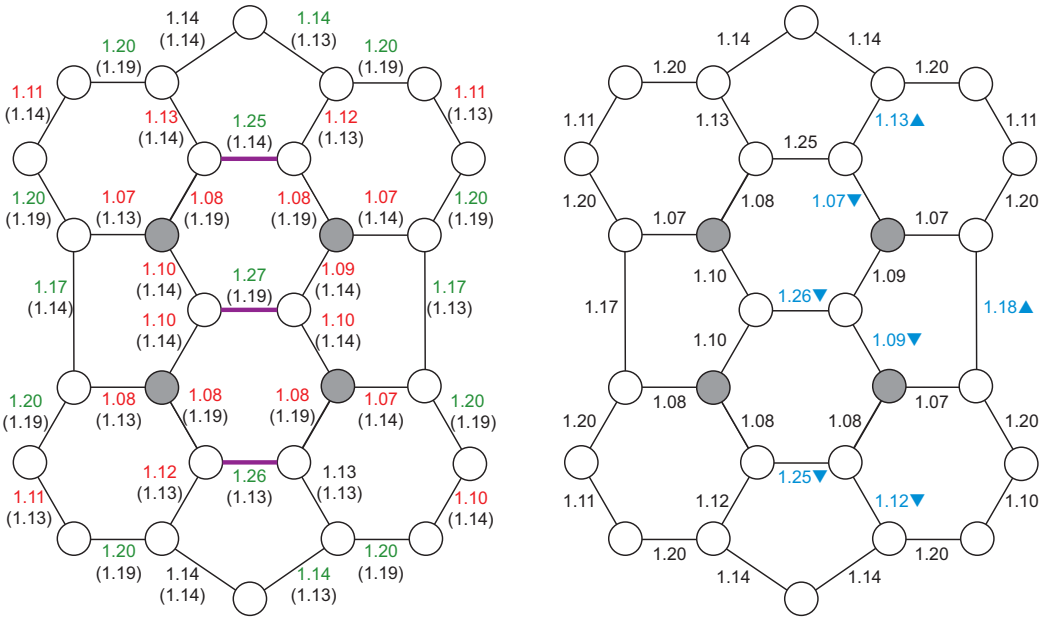
1.14 (1.14)
1.14 (1.13)
1.20 (1.19)
1.20 (1.19)
1.11 (1.14)
1.11 (1.13)
1.13 (1.14)
1.25 (1.14)
1.12 (1.13)
1.20 (1.19)
1.07 (1.13)
1.08 (1.19)
1.08 (1.19)
1.07 (1.14)
1.20 (1.19)
1.17 (1.14)
1.10 (1.14)
1.27 (1.19)
1.09 (1.14)
1.17 (1.13)
1.10 (1.14)
1.10 (1.14)
1.20 (1.19)
1.08 (1.13)
1.08 (1.19)
1.08 (1.19)
1.07 (1.14)
1.20 (1.19)
1.12 (1.13)
1.26 (1.13)
1.13 (1.13)
1.11 (1.13)
1.10 (1.14)
1.20 (1.19)
1.14 (1.14)
1.14 (1.13)
1.20 (1.19)
1.14
1.14
1.20
1.20
1.11
1.13
1.13▲
1.11
1.25
1.20
1.07
1.08
1.07▼
1.07
1.20
1.10
1.09
1.17
1.26▼
1.18▲
1.10
1.09▼
1.20
1.08
1.07
1.20
1.08
1.08
1.11
1.12
1.25▼
1.12▼
1.10
1.20
1.20
1.14
1.14

(a) r2a

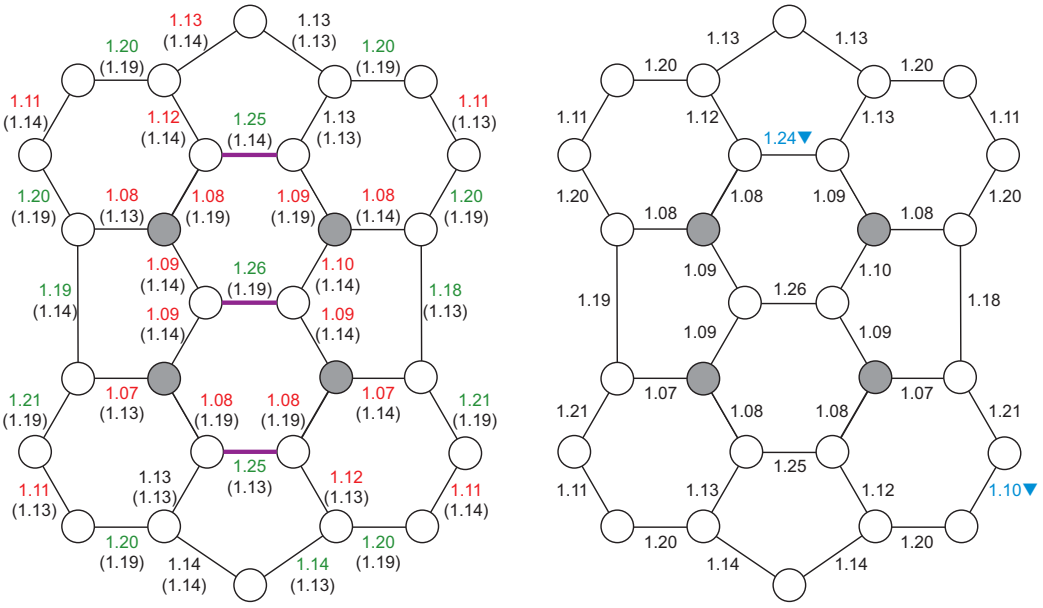
1.13 (1.14)
1.13 (1.13)
1.20 (1.19)
1.20 (1.19)
1.11 (1.14)
1.11 (1.13)
1.12 (1.14)
1.25 (1.14)
1.13 (1.13)
1.20 (1.19)
1.08 (1.13)
1.08 (1.19)
1.09 (1.19)
1.08 (1.14)
1.20 (1.19)
1.09 (1.14)
1.26 (1.19)
1.10 (1.14)
1.19 (1.14)
1.18 (1.13)
1.09 (1.14)
1.09 (1.14)
1.21 (1.19)
1.07 (1.13)
1.08 (1.19)
1.08 (1.19)
1.07 (1.14)
1.21 (1.19)
1.13 (1.13)
1.25 (1.13)
1.12 (1.13)
1.11 (1.13)
1.11 (1.14)
1.20 (1.19)
1.14 (1.14)
1.14 (1.13)
1.20 (1.19)
1.13
1.13
1.20
1.20
1.11
1.12
1.24▼
1.13
1.11
1.20
1.08
1.08
1.09
1.08
1.20
1.09
1.26
1.10
1.19
1.18
1.09
1.09
1.21
1.07
1.08
1.08
1.07
1.21
1.25
1.11
1.13
1.12
1.10▼
1.20
1.20
1.14
1.14

(b) r2e

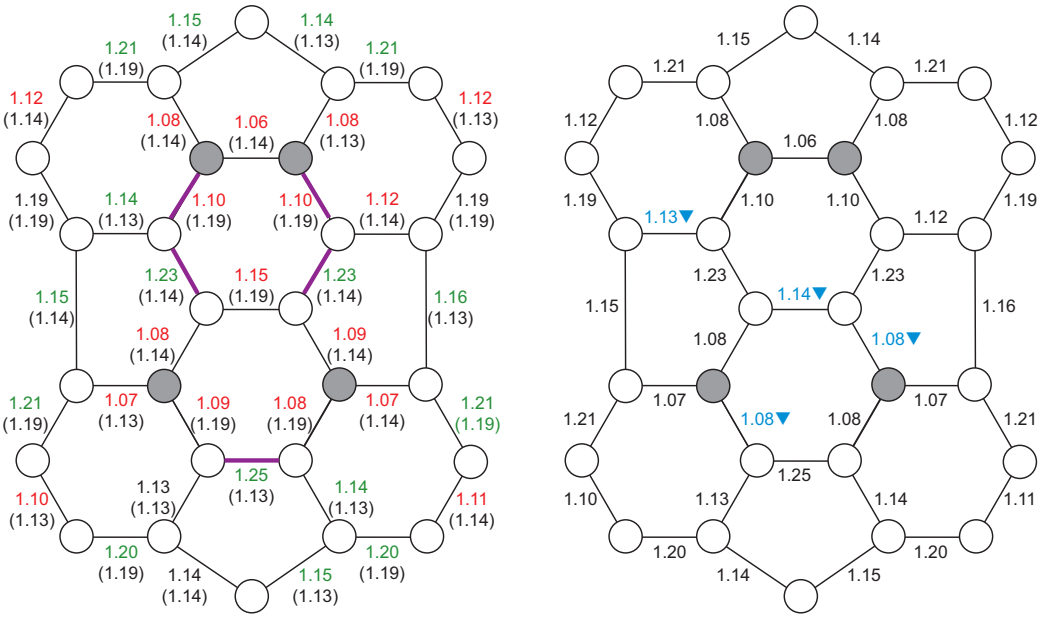
1.15 (1.14)
1.14 (1.13)
1.21 (1.19)
1.21 (1.19)
1.12 (1.14)
1.12 (1.13)
1.08 (1.14)
1.06 (1.14)
1.08 (1.13)
1.19 (1.19)
1.14 (1.13)
1.10 (1.19)
1.10 (1.19)
1.12 (1.14)
1.19 (1.19)
1.23 (1.14)
1.15 (1.19)
1.23 (1.14)
1.15 (1.14)
1.16 (1.13)
1.08 (1.14)
1.09 (1.14)
1.21 (1.19)
1.07 (1.13)
1.09 (1.19)
1.08 (1.19)
1.07 (1.14)
1.21 (1.19)
1.25 (1.13)
1.13 (1.13)
1.14 (1.13)
1.10 (1.13)
1.11 (1.14)
1.20 (1.19)
1.20 (1.19)
1.14 (1.14)
1.15 (1.13)
1.15
1.14
1.21
1.21
1.12
1.08
1.08
1.12
1.06
1.19
1.13▼
1.10
1.10
1.12
1.19
1.23
1.23
1.14▼
1.15
1.16
1.08
1.08▼
1.21
1.07
1.08▼
1.08
1.07
1.21
1.25
1.10
1.13
1.14
1.11
1.20
1.20
1.14
1.15

(c) t4b

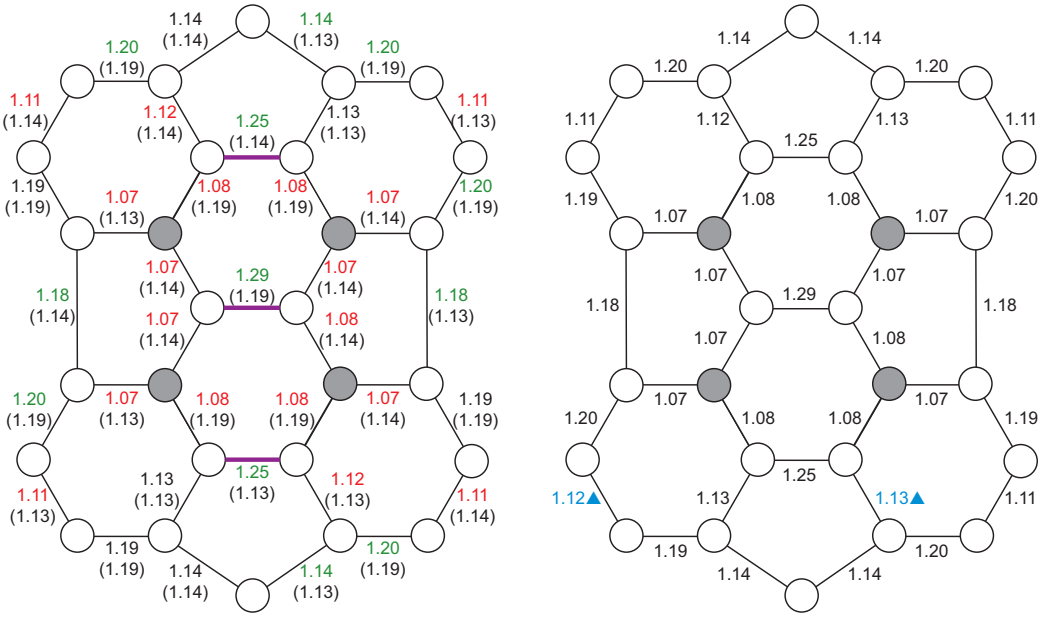
1.14 (1.14)
1.14 (1.13)
1.20 (1.19)
1.20 (1.19)
1.11 (1.14)
1.12 (1.14)
1.25 (1.14)
1.13 (1.13)
1.11 (1.13)
1.19 (1.19)
1.07 (1.13)
1.08 (1.19)
1.08 (1.19)
1.07 (1.14)
1.20 (1.19)
1.07 (1.14)
1.29 (1.19)
1.07 (1.14)
1.18 (1.14)
1.18 (1.13)
1.07 (1.14)
1.08 (1.14)
1.20 (1.19)
1.07 (1.13)
1.08 (1.19)
1.08 (1.19)
1.07 (1.14)
1.19 (1.19)
1.25 (1.13)
1.13 (1.13)
1.12 (1.13)
1.11 (1.13)
1.11 (1.14)
1.19 (1.19)
1.20 (1.19)
1.14 (1.14)
1.14 (1.13)
1.14
1.14
1.20
1.20
1.11
1.12
1.25
1.13
1.11
1.19
1.07
1.08
1.08
1.07
1.20
1.07
1.29
1.07
1.18
1.18
1.07
1.08
1.20
1.07
1.08
1.08
1.07
1.19
1.25
1.12▲
1.13
1.13▲
1.11
1.19
1.20
1.14
1.14

(d) t4c

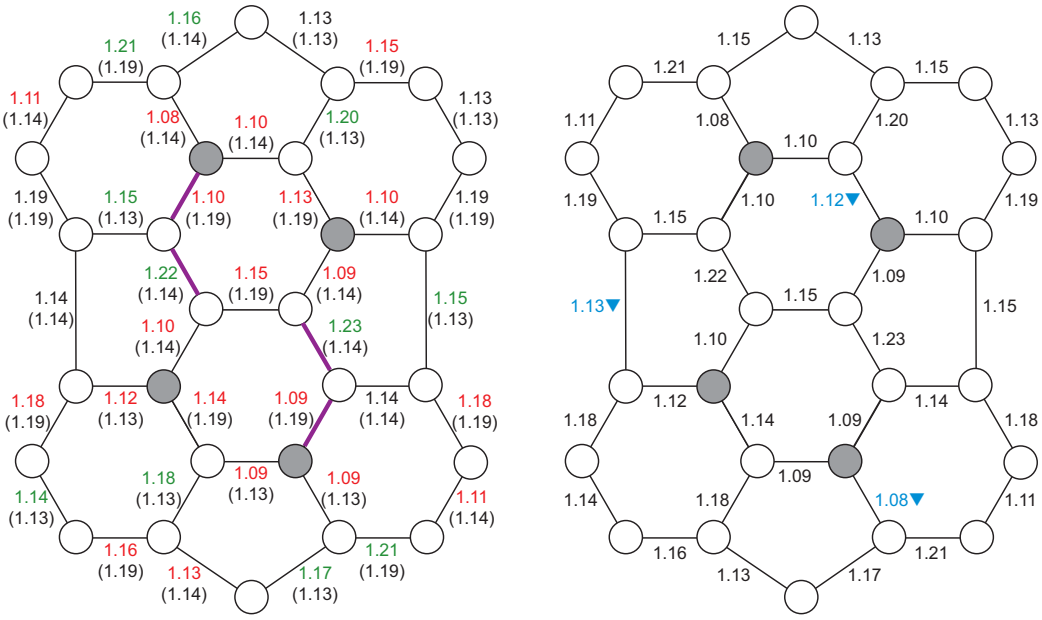

(e) t4h

Figure 5.6: The relevant configuration for the C_{60} on the left, and with the N@C_{60} on the right, with the accompanying ratios of the negative eigenvalues. For the C_{60}, the bond ratios for the isolated cage are bracketed underneath, and are shown in black. The differences between the ratios for the r2a configuration and the isolated cage are shown in red for a decrease in the C_{60} bond ratio from the isolated cage, and are shown in green for an increase in the C_{60} bond ratio from the isolated cage. Those bond ratios that remain unchanged, are shown in black. The key changes in rebonding (only in the C_{60} diagrams) are highlighted by purple bonds, instead of the standard black colour. For the N@C_{60}, the differences between the C_{60} and N@C_{60} bond ratios are shown in blue, with an arrow indicating the direction of change. For both diagrams the carbon atoms that bond with the silicon surface are shown in grey, and those carbon atoms that do not bond with the silicon surface are shown in white.

Type 2

The type 2 configurations have a pentagon and a hexagon in the immediate vicinity of the cage's bonding region with the surface. Three of the configura-

tions, r2b (see Figure 5.7(a)), r2f (see Figure 5.7(b)) and t4d (see Figure 5.7(d)), all possess the same set of bonding atoms as each other, and as such the rebonding patterns that take place are in general very similar. This basically entails the weakening of four of the bonds that are between the bonding atoms, and the significant strengthening of the fifth central bond. In the r2b and r2f configurations the two bonding atoms that are part of the pentagon also have two bonds that have significant rebonding taking place. The t4d configuration, however, only has a significant change taking place in one of these bonds, which makes sense as the C-Si bond formed between the other bonding atom and the surface is very long and weak (so the lack of rebonding in that area of the cage reflects that).

The t4a configuration (see Figure 5.7(c)) has the largest spread of the configurations, with the bonding atoms on two isolated hexagons (although two of the bonding atoms do share a third hexagon that is adjacent to both the isolated hexagons). Perhaps, unsurprisingly this leads to wider changes in terms of the scope of the rebonding, however, the main area of major rebonding is still enclosed in the area between the four bonding atoms. Here we effectively see two stronger (double) bonds on the third hexagon swap places with two weaker (single) bonds on the central pentagon.

The t4g configuration (see Figure 5.7(e)) illustrates a variation of the r2a, r2d, and t4d configurations, except one of the bonding atoms on the pentagon has been moved to the neighbouring hexagon. This leads to the majority of the rebonding that takes place being very similar to those previous configurations. The only difference being that in the t4g configuration there is a change in rebonding in the proximity of the moved bonding atom, with one of the weaker (single) bonds on the pentagon becoming a stronger (double) bond.

With the t4i configuration (see Figure 5.7(f)), the bonding atoms on the hexagon have moved to the back two positions of the hexagon. This actually has a large effect, as the centre region (between the four bonding atoms) remains largely unchanged by rebonding (which is unique among the Type 2 configura-

tions). The majority of the rebonding in the t4i configuration is localised more tightly around the bonding atoms than in previous configurations.

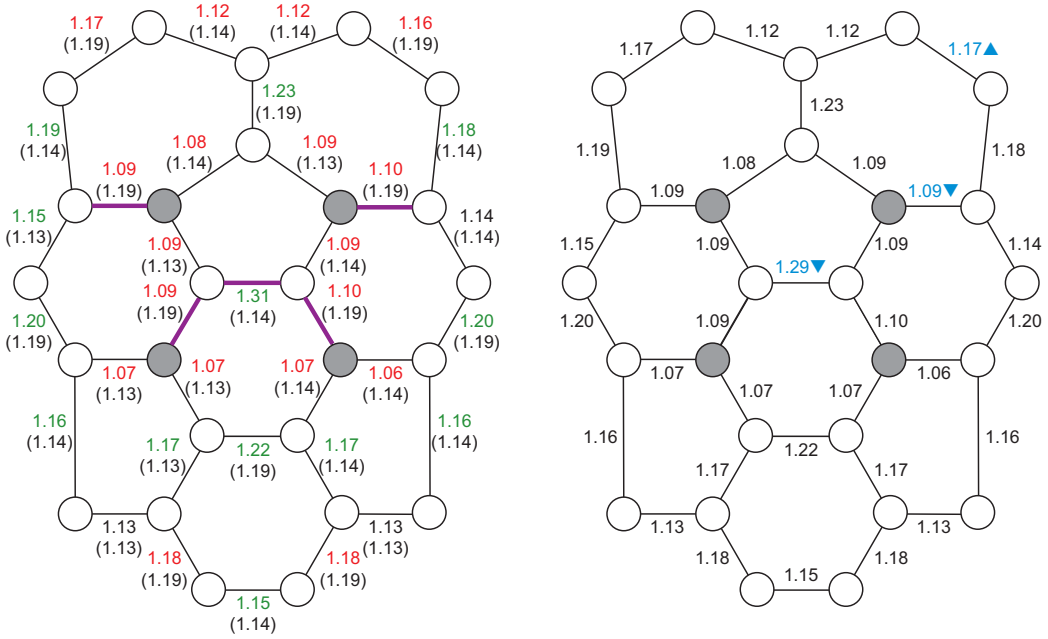

(a) r2b

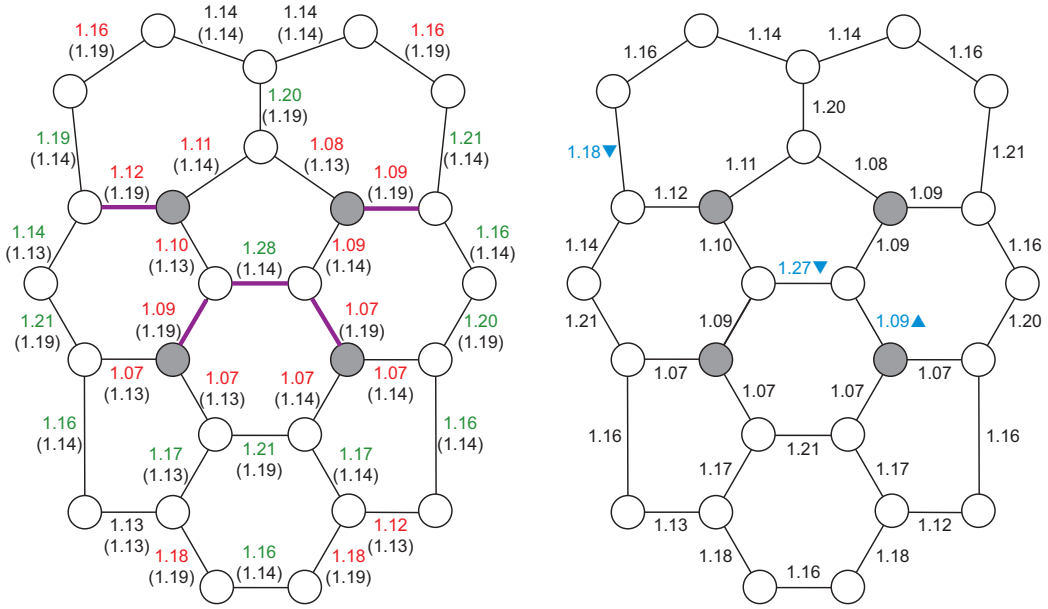

(b) r2f

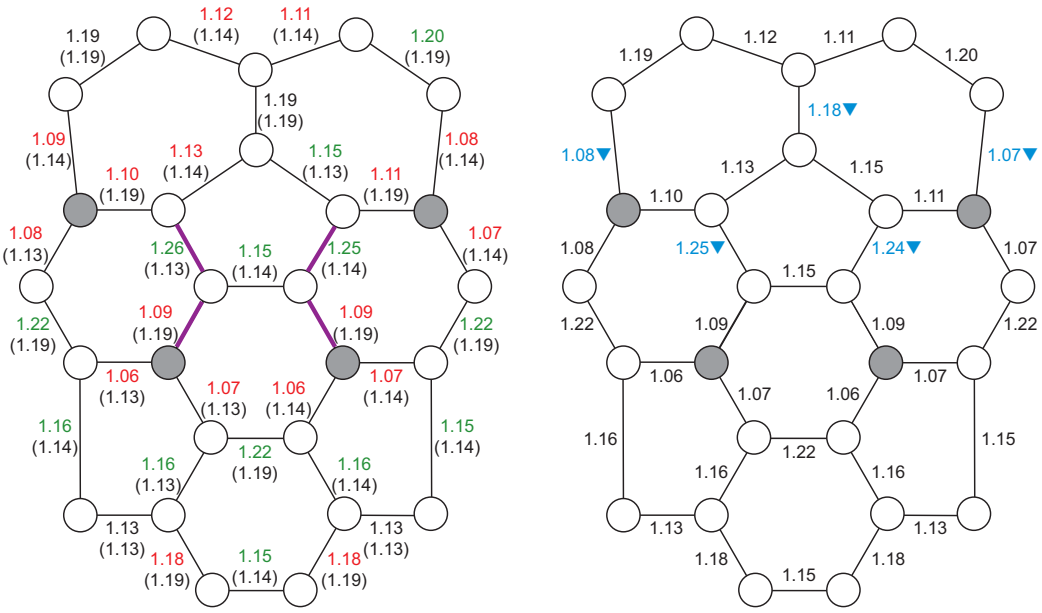
1.19 (1.19)
1.12 (1.14)
1.11 (1.14)
1.20 (1.19)
1.19 (1.19)
1.09 (1.14)
1.13 (1.14)
1.15 (1.13)
1.08 (1.14)
1.10 (1.19)
1.11 (1.19)
1.08 (1.13)
1.26 (1.13)
1.15 (1.14)
1.25 (1.14)
1.07 (1.14)
1.09 (1.19)
1.09 (1.19)
1.22 (1.19)
1.22 (1.19)
1.06 (1.13)
1.07 (1.13)
1.06 (1.14)
1.07 (1.14)
1.16 (1.14)
1.15 (1.14)
1.22 (1.19)
1.16 (1.13)
1.16 (1.14)
1.13 (1.13)
1.13 (1.13)
1.18 (1.19)
1.15 (1.14)
1.18 (1.19)
1.19
1.12
1.11
1.20
1.18▼
1.08▼
1.13
1.15
1.07▼
1.10
1.11
1.08
1.25▼
1.24▼
1.07
1.15
1.22
1.09
1.09
1.22
1.06
1.07
1.06
1.07
1.16
1.22
1.15
1.16
1.16
1.13
1.13
1.18
1.15
1.18

(c) t4a

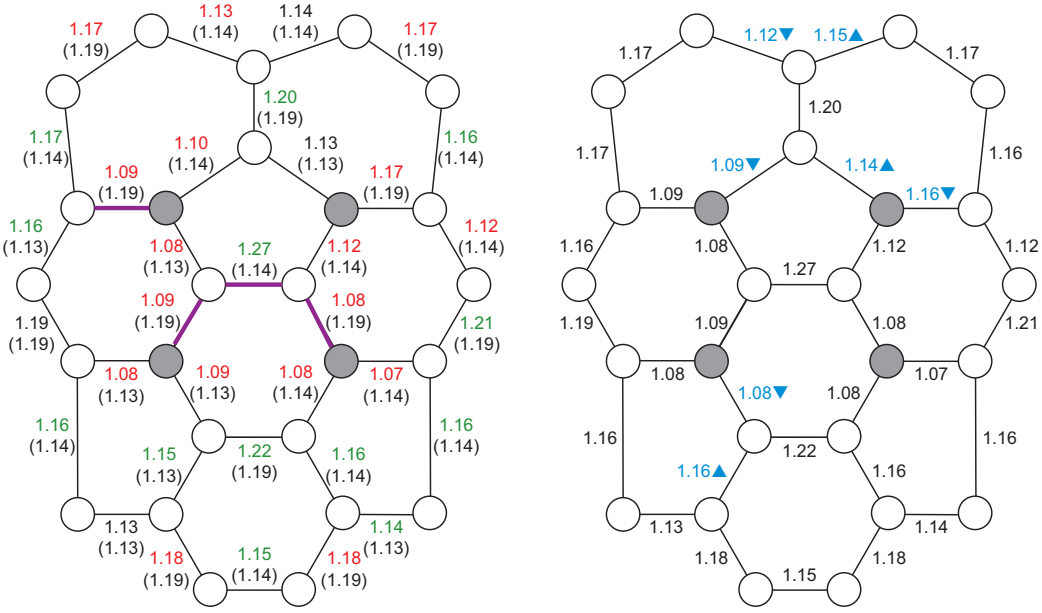
1.17 (1.19)
1.13 (1.14)
1.14 (1.14)
1.17 (1.19)
1.20 (1.19)
1.17 (1.14)
1.10 (1.14)
1.13 (1.13)
1.16 (1.14)
1.09 (1.19)
1.17 (1.19)
1.16 (1.13)
1.08 (1.13)
1.27 (1.14)
1.12 (1.14)
1.12 (1.14)
1.09 (1.19)
1.08 (1.19)
1.19 (1.19)
1.21 (1.19)
1.08 (1.13)
1.09 (1.13)
1.08 (1.14)
1.07 (1.14)
1.16 (1.14)
1.16 (1.14)
1.15 (1.13)
1.22 (1.19)
1.16 (1.14)
1.13 (1.13)
1.14 (1.13)
1.18 (1.19)
1.15 (1.14)
1.18 (1.19)
1.17
1.12▼
1.15▲
1.17
1.20
1.17
1.09▼
1.14▲
1.16
1.09
1.16▼
1.16
1.08
1.12
1.12
1.27
1.19
1.09
1.08
1.21
1.08
1.08▼
1.08
1.07
1.16
1.22
1.16
1.16▲
1.16
1.13
1.14
1.18
1.15
1.18

(d) t4d

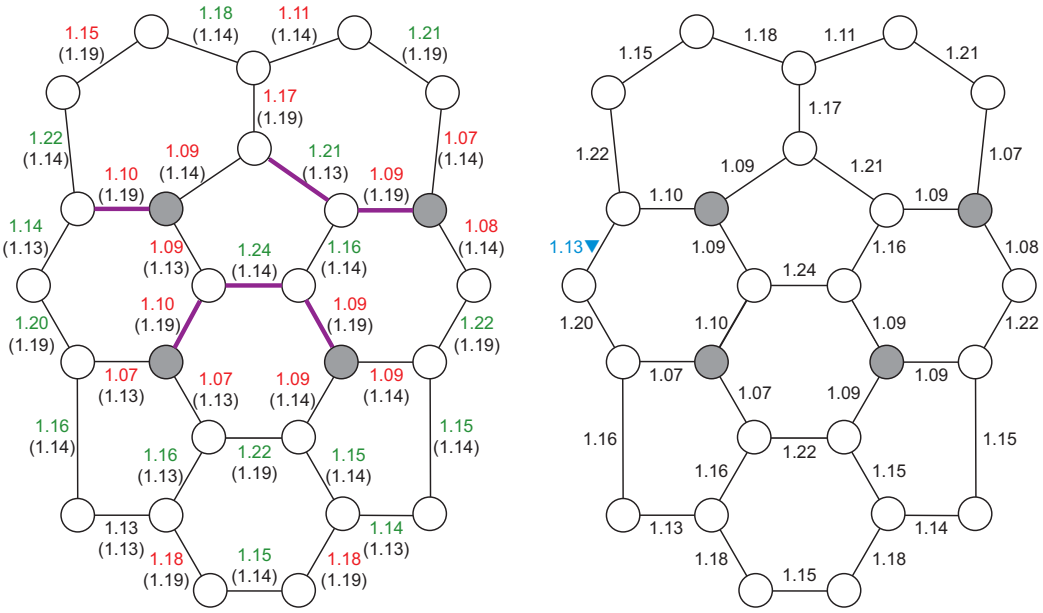

(e) t4g

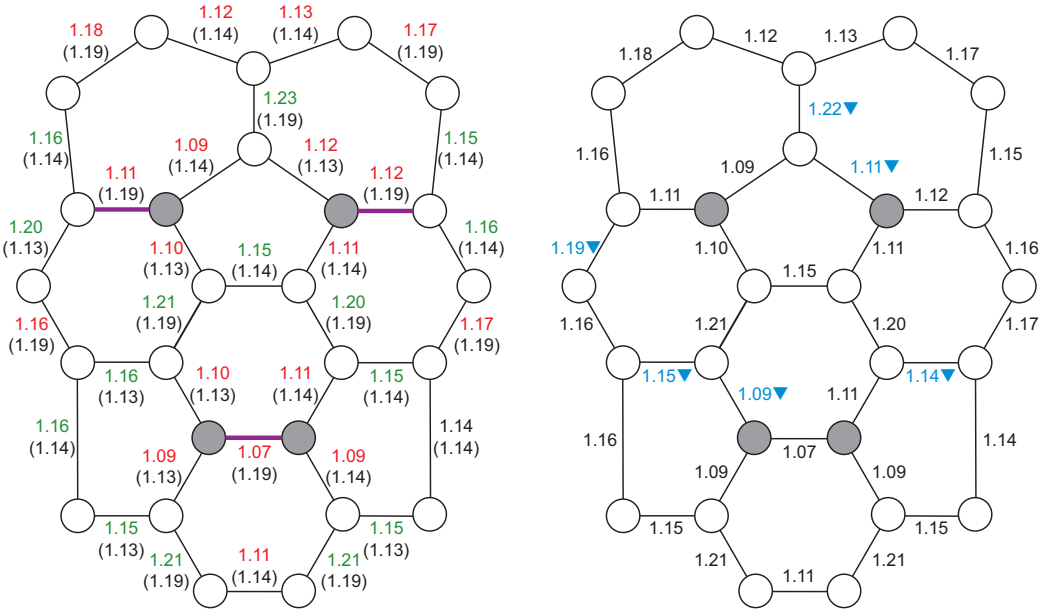

(f) t4i

Figure 5.7: The relevant configuration for the C_{60} on the left, and with the N@C60 on the right, with the accompanying ratios of the negative eigenvalues. The same colouring and labelling scheme from Figure 5.6 is used here.

Type 3

The type 3 configurations are the two configurations, r2c (see Figure 5.8(a)) and r2g (see Figure 5.8(b)), that have a single hexagon in the immediate vinicity of the cage's bonding region with the surface. The significant areas of rebonding are marginally different for these two confiurations, which is surprising as the r2g configuration is simply a 90° rotation of the r2c configuration. While the differences are only slight they are interesting as the other pairs of configurations (r2a & r2e and r2b & r2f) are more similar to one another. This could be due to the fact that the r2c and r2g configurations have a much smaller area of the fullerene cage in proximity to the surface, so it is more likely to be sensitive to slight changes, the changes may even be simply a by-product of the alternating nature of the 2×2 surface reconstruction. As expected of a smaller bonding site (in terms of the area of the cage's surface) the rebonding is much more localised and the only significant changes all take place on the hexagon that all four bonding atoms are a part of. All three of the stronger (double) bonds, and all three of the weaker (single) bonds that make up this hexagon, become weaker in order to create the required C-Si bonds.

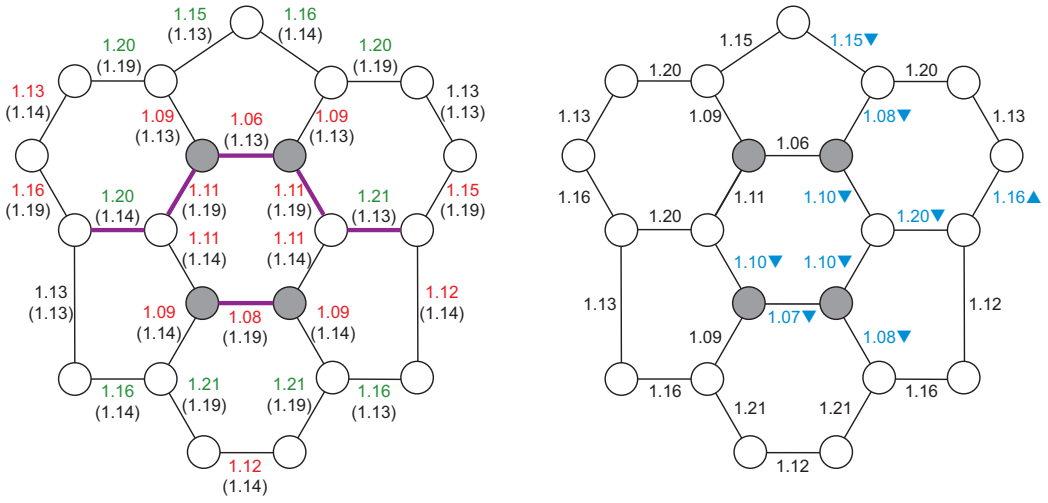

(a) r2c

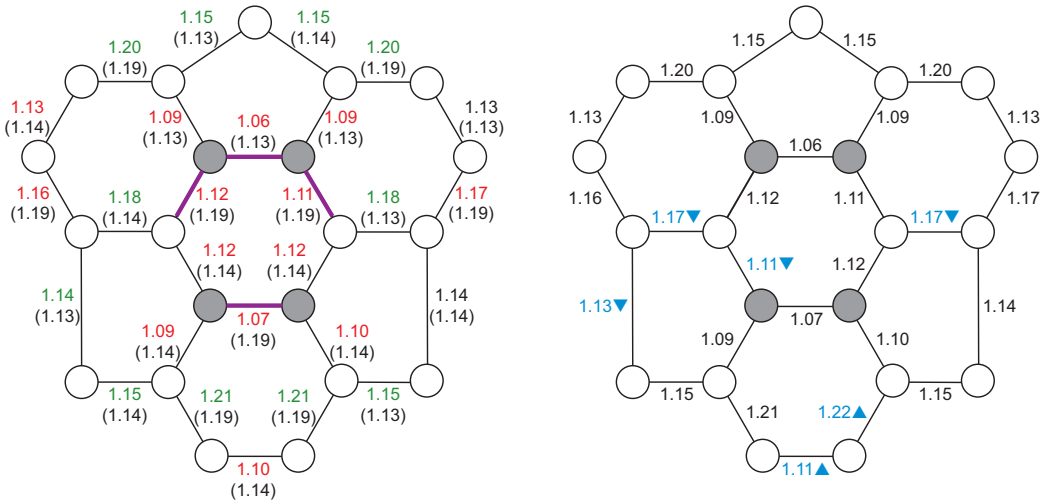

(b) r2g

Figure 5.8: The relevant configuration for the C_{60} on the left, and with the N@C60 on the right, with the accompanying ratios of the negative eigenvalues. The same colouring and labelling scheme from Figure 5.6 is used here.

Type 4

There is only one type 4 configuration, the r2d configuration (see Figure 5.9), which has a single pentagon in the vicinity of the cage's bonding region to the surface. All four of the bonding atoms are part of this pentagon, so the rebonding, in the main, is centred in that region. There does, however, appear to be a higher level of delocalised rebonding in this configuration than found in the other configurations. This can be associated to the smaller area of the cage that bonds to the surface and the higher level of curvature (which leads to strain) around the pentagon (it is after all the pentagons which supply the curvature to the fullerene cages).

Unlike previous configurations, when we compare our results for this configuration with those found in a previous study [17], there is a significant difference. This relates to the bonds surrounding one of the non-bonding atoms directly off of the central pentagon. In their work the bonds around this atom were all weakened, which in the authors' opinion could be a result of weak bonding

between that atom and the surface. Due to the significant level of tilt of the surface (a complete lack of dimer flatness) in their calculation, it is highly possible that the fullerene was in tilted so close to the surface that some extra C-Si bonding took place. Thus it is likely that their hypothesis is correct, and that their t4d results actually represent a configuration that has five bonding atoms.

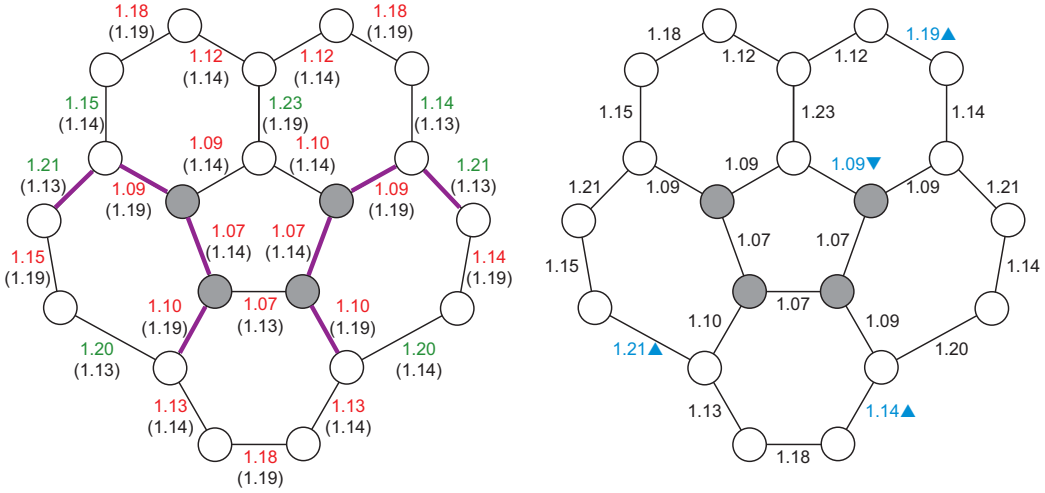

Figure 5.9: The r2d configuration for the C60 on the left, and the N@C60 on the right, with the accompanying ratios of the negative eigenvalues. The same colouring and labelling scheme from Figure 5.6 is used here.

When analysing the bonding within the lower part of the fullerene cage (the region which bonds to the silicon surface), our results compare favourably with those by Frangou *et al.* [17]. The C-C bonds for the carbon atoms that form the C-Si bonds have all decreased bond ratios (see Figures 5.6 through to 5.9), which results from the formation of the carbon-silicon bonds. While the majority of the rebonding is localised within the immediate vicinity of these carbon atoms, there are areas of delocalised rebonding taking place, as the fullerene has to internally readjust to the changes in its shape and curvature. As expected the bonding within the adsorbed fullerenes no longer resembles that found in the isolated fullerene cage (i.e. single bonds around pentagons and double bonds shared by hexagons). Comparing the C_{60} and $N@C_{60}$ Bader bond ratios of the cage around the bonding region (again see Figures 5.6 through to 5.9), it is clear

that the presence of the endohedral nitrogen atom has little or no effect on the internal rebonding of the fullerene cage due to adsorption on the silicon surface.

5.4 Conclusions

Adding an endohedral nitrogen atom to the buckminsterfullerene cage has little effect on how the cage bonds to the silicon surface, in terms of the rebonding within the fullerene and the carbon-silicon bond lengths. The binding energies are slightly different, and in general this change makes the N@C_{60} configurations more favourable than their C_{60} counterparts. The spin on the endohedral nitrogen atom is almost unchanged (~ 0.1 for all configurations). The displacement of the endohedral nitrogen atom is relatively small (a maximum of ~ 0.3 Å). The charge transfer between the endohedral nitrogen atom and the fullerene cage is minimal. The effect of these factors on the binding energies is minimal in the vast majority of cases. The results presented here indicate that the endohedral nitrogen atom is almost perfectly isolated from the fullerene cage, and that the fullerene cage is largely unaffected by the endohedral atom's presence. As such, there is a very strong and valid case for using nitrogen doped C_{60} molecules as part of a quantum computing qubit.

Chapter 6

Multiple fullerenes

6.1 Introduction

There has been little research done, in terms of *ab-initio* calculations, on investigating the behaviour of two C_{60} fullerenes in close proximity to one another upon the Si (100) surface. A previous *ab-initio* study, by Frangou [24], investigated systems of this kind with the fullerenes placed on adjacent silicon surface dimers. The study looked at the t4 group of configurations, which are generally assumed to be the most stable of the four groupings. The separation distance of the two fullerenes (measured as the distance from the centre of mass of one fullerene to the other) in these calculations was typically in the range of 8 to 9.5 Å; the reason for this large range is that the separation distance was shown to be very much dependent on the fullerene bonding configurations used. With the close proximity of these two fullerenes, a few interesting observations were made. In general there was a large decrease in the favourability, of the binding energies, for these combined systems, compared to the two corresponding isolated cases. In a few cases (the least stable ones) there was actually significant bonding and rearrangement taking place between the two fullerenes. As the fullerene separation was increased the combined systems started to become more favourable, approaching the levels seen in the isolated cases.

In a previous experimental study [4] the separation distances of pairs of C_{60}

molecules upon silicon surfaces were studied. When attempting to manipulate one C_{60} molecule towards a second C_{60} molecule, via STM tip manipulation, the closest the fullerenes could be moved together was 10.9 Å (from an initial separation of 11.5 Å). The only way the two fullerenes would sit that close was for one of the fullerenes to roll over into an adjacent trench. The closest the two fullerenes could be manipulated to one another, and remain within the same trench, was 11.5 Å. Separation distances in this range, compared to the computational study, proved more favourable. It is believed that in order to achieve a separation distance for the two fullerene cages within this range, there needs to be a silicon dimer between the two fullerene bonding sites; for this reason we have decided in this study, to investigate pairs of fullerenes in various t4 configurations, where there is a one silicon dimer gap between the two bonding sites on the silicon surface.

6.2 Methodology

As with our previous fullerene calculations, one way in which to assess the favourability of the new combined systems is the calculation of the binding energy for the combined system, which is given in Equation 6.1. This is shown for two configurations, A and B, and in our actual calculations these will be replaced with by combinations of the t4 configurations.

$$E_{\text{binding of A-B}} = E_{\text{A-B}} - 2 \times E_{\text{isolated fullerene}} - E_{\text{isolated MF surface}} \tag{6.1}$$

In order to calculate the favourability of the combined system we shall use the formula as shown in Equation 6.2; this measures the binding energy of the combined system with the binding energies of the two isolated systems. This provides a clear insight into the improvement of the combined system versus its isolated components, however it does not allow for direct comparison between different combined systems. This is because the measure of favourability as defined in Equation 6.2, only gives a measure of favourability for the specific

combined and isolated systems.

$$E_{\text{favourability of A-B}} = E_{\text{binding of A-B}} - E_{\text{binding of A}} - E_{\text{binding of B}} \tag{6.2}$$

By the way that the favourability measure is defined, a positive energy indicates that the combination of configurations is less favourable than the two fullerenes in isolation. A negative energy therefore indicates that the combination of configurations is more favourable than the two fullerenes in isolation. As with the previous study [24], the separation distance between the two fullerene cages is measured as the distance between the centre of mass of each fullerene cage.

6.2.1 Simulation cell

For the multiple fullerene configurations we have used a different surface than used in Chapter 5; this is because the previous surface of 128 atoms is physically too small to place two fullerenes on the surface and maintain the required separation between the two. For this reason we use the 384 atom silicon surface that has been previously use to study multiple fullerene systems [24].

One of the main considerations that went into the creation of this new surface was the distance between the periodic repeats of the fullerene molecule(s). In order to increase the periodic repeat distances, not only has the physical size of the surface been increased, but the surface has non-orthogonal cell vectors and the dimer rows do not run perpendicular, or at 45°, to the cell vectors. This means that the dimer row of the simulation cell connects to another dimer row of the periodic cell repeat; leading to a significant increase in the distance between periodic repeats of the fullerene(s).

The other characteristics of the smaller 128 atom surface are carried over to the new larger surface. So it is a 2×2 tilted dimer reconstruction, that has a depth of six layers of silicon (with the final two layers pinned in bulk positions), and the dangling bonds of the final silicon layer are saturated by hydrogen atoms

(pinned in their relaxed positions).

6.3 Initial work

In order to ascertain the favourability of configurations, as previously outlined, we first need to calculate the binding energy of a single fullerene molecule upon the new larger silicon surface in all of the trench configurations outlined in Chapter 5. The binding energies of these systems are presented in Table 6.1:

Config.	Previous surface (128 atoms)	New surface (384 atoms)
t4a	-2.84	-2.29
t4b	-3.14	-2.62
t4c	-3.14	-2.30
t4d	-2.40	-1.62
t4g	-2.77	-1.95
t4h	-2.52	-1.57
t4i	-2.41	-1.64

Table 6.1: Binding energies, in eV, of the C_{60} molecule, in the t4 group of configurations, on the two types of Si(100) surface that have been discussed.

As Table 6.1 illustrates, there appears to be a shift in not only the magnitude of the binding energies, with every configuration becoming less favourable on the larger surface, but the ordering of the favourability hierarchy has also changed. All of the differences in terms of hierarchy changes actually bring our results more in line with those found previously using the smaller size surface and the 2×1 surface reconstruction. For the t4d case in particular the length of the one long C-Si bond goes from 2.73 Å, with the 128 atom surface, to 2.43 Å with the new surface. This could indicate that the increased bond length for the 128 atom surface, with the t4d configuration, is solely a result of the surface size and not completely related to the surface reconstruction.

We attribute the decrease in system favourability in all configurations to a interesting concept of note, namely, that to an extent the fullerenes actually prefer sitting in proximity to one another. With the previous smaller surface we had a surface that consisted of two rows of four dimer pairs; this means that the periodic repeats of the fullerenes upon the surface only had two dimer pairs between the fullerene bonding site and its periodic repeat. In terms of separation across the trenches, there will only be one empty trench between the fullerene bonding site and its periodic repeat, and this is illustrated in Figure 6.1:

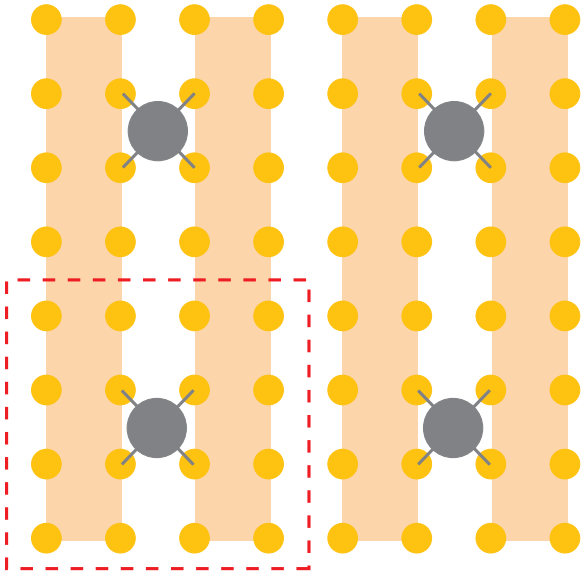

Figure 6.1: Top down schematic, showing only the top layer of atoms, of the previous 128 atom supercell for the silicon surface. The original supercell is the area within the dotted line, which is shown amongst three periodic repeats. The fullerene in the t4 position is shown as a grey circle, the dimer rows are the pale orange bars, and the white gap between the rows represents the trench. The silicon atoms that make up the surface dimers are shown as yellow circles.

With the new larger surface the distances between the periodic repeats are now much greater; and this new surface is illustrated in Figure 6.2.

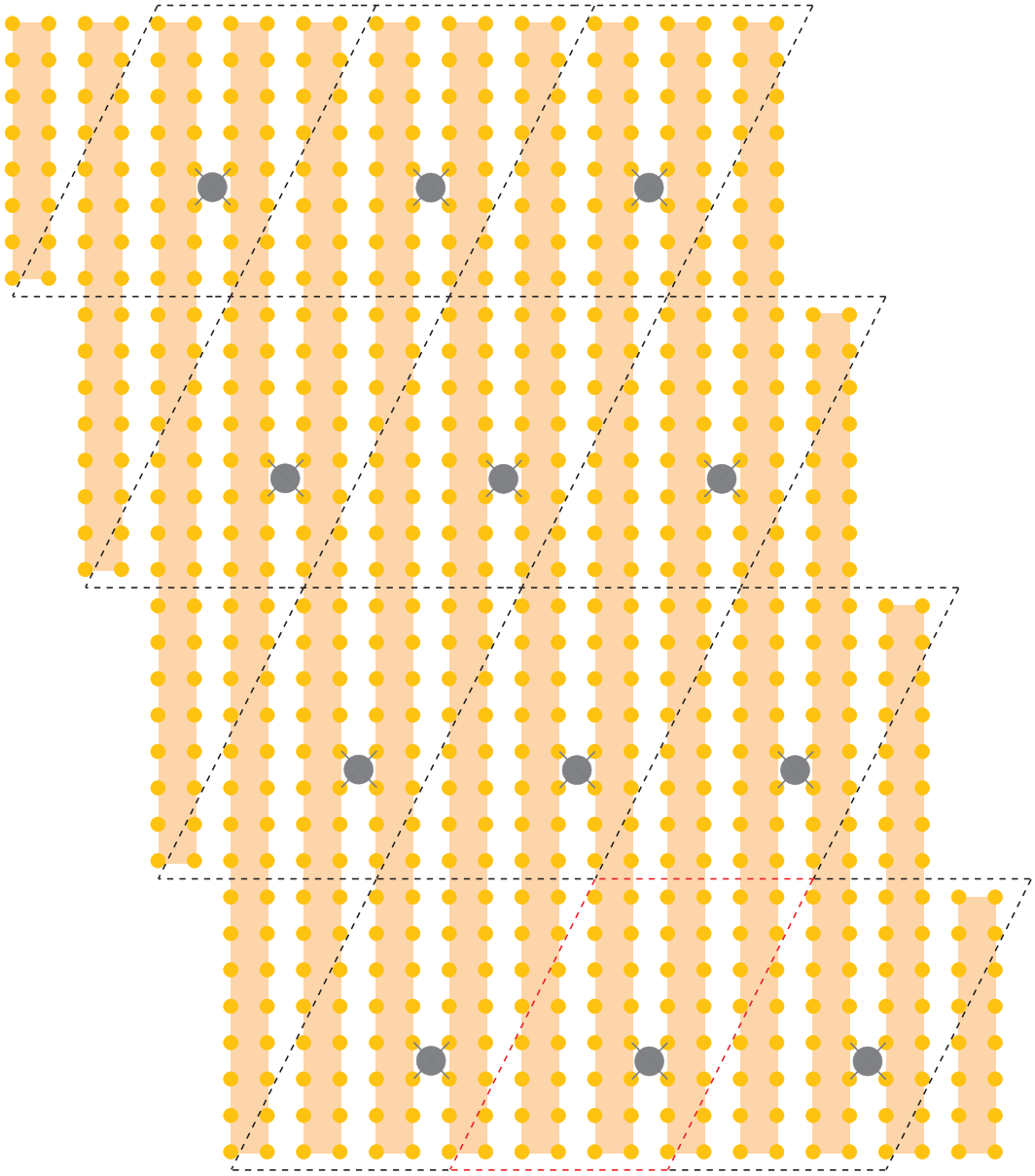

Figure 6.2: Top down schematic, showing only the top layer of atoms, of the new 384 atom supercell for the silicon surface. The original supercell is the area within the red dotted line, which is shown amongst eleven periodic repeats, which are shown as within the black dotted lines. The fullerene is the t4 position, and the colouring scheme is the same as in Figure 6.1.

There is now a two trench gap between periodic fullerene repeats, across the rows, and there are twenty-two silicon surface dimers between the periodic fullerene repeat within the same trench. This larger surface was specifically

designed to increase the distance between these two periodic repeats. In doing so, however, the non-uniform nature of the supercell leads to other periodic fullerene repeats that are, at times, closer, in terms of the separation distance, than the two periodic repeats discussed previously. There is now, for example, a periodic fullerene repeat in the trench adjacent to the fullerene in the original supercell, which is only separated by six silicon surface dimers.

In the next Sub-Section the issue of interaction with periodic fullerene repeats shall be explored, however, with a supercell of the non-uniform nature as we have here, it is difficult to gauge this interaction.

6.3.1 Investigating periodic repeat distances

In order to assess how significant the distances between the periodic fullerene repeats are, we performed two sets of calculations. For the first set we took the previous smaller (128 atom) surface as a starting point and increased the number of dimer pairs, that make up the dimer rows, from four to six; and then continued the increases in increments of two up until a surface with a two dimer rows of sixteen dimer pairs. This was in order to assess how much influence the periodic repeat within the same trench has on the calculation.

The second set of calculations were concerned with how much influence the periodic fullerene repeat that is separated (initially) by one trench has on the calculation; for those calculations we increased the number of dimer rows within the surface (keeping the number of dimer pairs constant at four). Initially there were two rows (the previous smaller surface was again used as the starting point for these calculations), which were increased to three, then four and as follows, up until a surface with eight dimer rows.

All of these custom surfaces were first allowed to relax in isolation and then a single fullerene was placed upon the surface in the t4b configuration (there was no need to look at a variety of fullerene configurations, so the most favourable configuration, t4b, was chosen) and allowed to relax. The binding energies were then calculated as given in Chapter 5, and the resulting binding energies are

Distance (in Å)	Repeat along trench Binding energy (in eV)	Repeat across rows Binding energy (in eV)
15.36	-3.14	-3.14
23.04	-3.06	-2.99
30.72	-3.00	-2.97
38.40	-2.88	-3.11
46.07	-2.99	-3.04
53.75	-3.10	-3.16
61.43	-2.96	-3.00

Table 6.2: The binding energies, in eV, for the t4b configuration upon the Si (100) surface. Various surfaces were created in order to accommodate the increases in periodic fullerene repeats. All of the extended surfaces were based on the original 128 atom silicon surface supercell.

given in Table 6.2.

The binding energies given in Table 6.2 have been shown graphically in Figure 6.3, providing a good illustration of the oscillation of the binding energies with increasing distance, for both cases. It is also clear that the influence of the periodic fullerene repeat within the same trench, is greater than the periodic fullerene repeat separated by the dimer rows. Another clear point is that neither set of binding energies has converged, so even when the periodic fullerene repeats are separated by over 60 Å, in both cases, there is still some level of interaction. It would appear that from the initial distance of $\sim$ 15 Å between the fullerene and its periodic repeat, as the distance is increased, in general, the binding energies become less favourable. This indicates that to an extent fullerenes are more favourably adsorbed onto the silicon surface within a close proximity of other fullerene molecules (although not at the close distances explored in the previous study [24]).

In terms of the calculations performed on C_{60} and $N@C_{60}$ molecules, in

isolation on the smaller 128 atom silicon surface (see Chapter 5), it would appear that there is a level of interaction with the periodic fullerene repeats. This has almost certainly made the binding energies more favourable, however, in the context of the calculations this is not important. The calculations were to allow for the comparison of C_{60} and $N@C_{60}$ molecules where the only system difference was the presence of the endohedral species, which the study still achieves. The same supercell for the silicon surface has previously been implemented by many studies [2, 14, 15, 16, 17].

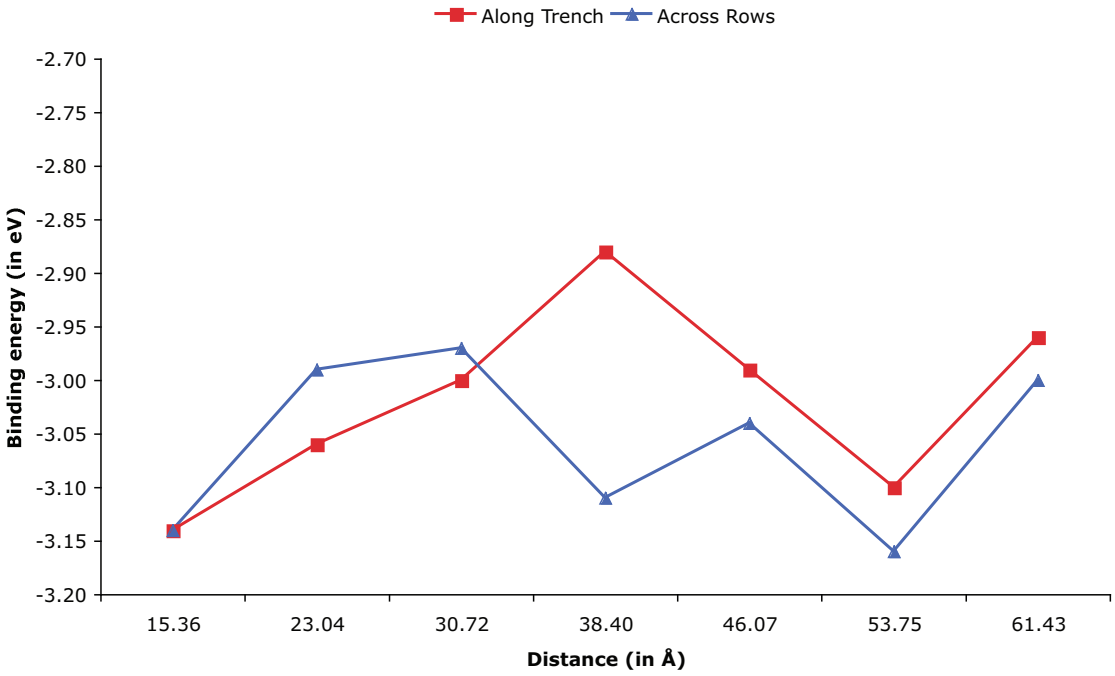

Figure 6.3: A graph showing the changes in binding energies, for the t4b configuration upon the Si (100) surface given in Table 6.2.

The larger 384 atom silicon surface has been previously used to study multiple fullerenes [24]; with this surface the interaction from the two types of repeats studied here is less of an issue, particularly for the periodic fullerene repeat within the same trench. The problem with this surface is its non-uniform nature which leads to other periodic repeats, whose influence is much harder to check. Some tests were performed where the surface was increased in terms

of both the number of dimer rows and dimer pairs, at the same time. These tests quickly became computationally unfeasible, as with using the previous technique of extending the 128 atom surface, quickly leading to surfaces with over 500 atoms for only a small increase in the number of dimer rows and dimer pairs. It is for this very reason that the 384 atom silicon surface was developed with its non-uniform nature.

Until either the computational effort is reduced, or the computational resources available increases, this will remain a topic of which further study could be performed. Although, as always the effort in doing so has to be weighed against the possible gain and its actual worth. We shall continue to use the 384 atom silicon surface, which has both previously been used for a study of this type [24], and addresses some of the issues raised here.

6.3.2 Distinct fullerene combinations

When placing the two fullerenes on to the silicon surface there are a vast array of possible arrangements and configurations. For this study of pairs of fullerenes on the Si (100) surface, we have chosen to focus on the seven configurations from the t4 configuration group that were successfully studied in isolation in Chapter 5. Even when the possible configurations are narrowed down to these seven configurations, there is still a lot of variation in the possible arrangements.

Since the two fullerene cages are in close proximity, the interaction between the molecules will be most significant in the regions of the two cages that are closest to one another. This is further complicated when a fullerene is placed on the surface as a 180° rotation of a specific configuration. In the isolated case the 180° rotation would be equivalent to the original configuration, however, with two fullerenes on the surface the 180° rotation affects which region of the fullerene cage will be closest to the other fullerene cage. These issues will be addressed subsequently in order to determine a set of unique fullerene combinations. We shall use the suffix "(R)" to denote those configurations which represent a 180° rotation, for example, the 180° rotation of the t4a configuration

will be denoted as t4a (R).

t4a

For the t4a configuration we have assumed a plane of reflective symmetry, which is shown in Figure 6.4(a). This reflective symmetry reduces the number of unique fullerene combinations that the t4a configuration is able to make with the other configurations. The t4a configuration possess no rotational symmetry, so the 180° rotational configuration, t4a (R), is unique (*i.e.* t4a $\neq$ t4a (R)).

t4b

The previous study [24] assumed a 180° rotational symmetry with the t4b configuration (*i.e.* t4b = t4b (R)). We have stuck with this assumption, as while it is obviously not strictly true we believe that the differences will be minimal, as the positioning of the fullerene will only have a small "slide" perpendicular to the direction of the trench. The t4b configuration already possessed one (vertical) plane of reflective symmetry, however, the assumption of the 180° rotational symmetry implies that there is a second (horizontal) plane of reflective symmetry. Both of these planes of reflective symmetries are illustrated in Figure 6.4(b). These symmetries, assumed or otherwise, significantly reduce the number of unique fullerene combinations involving the t4b configuration.

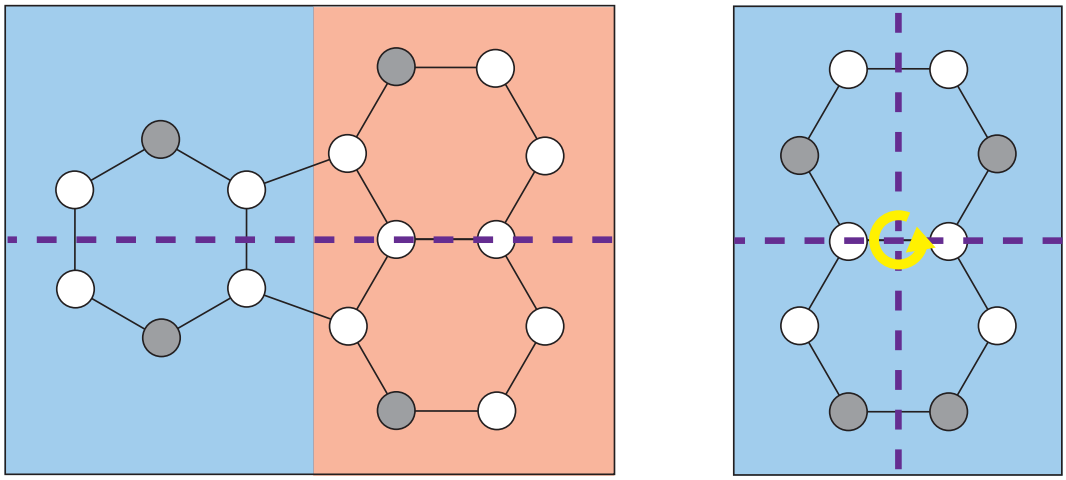

(a) t4a (b) t4b

Figure 6.4: Schematic illustrations demonstrating the symmetries associated with both the t4a and t4b configurations. The purple dashed lines represent the planes of reflective symmetry that the configurations possess. The red and blue shading in the t4a configuration illustrate the equivalent regions within the configuration, where the two red regions (separated by the plane of symmetry) are equivalent, and likewise the two blue regions. The t4b is completely shaded blue as all regions are equivalent under our assumptions. The yellow arrow on the t4b configuration signifies the 180° rotational symmetry associated with the configuration.

t4c

The t4c configuration, as shown in Figure 6.5(a), is the most uniform of all the configurations. It possesses a 180° rotational symmetry (*i.e.* t4c = t4c (R)), which unlike the t4b configuration is explicit rather than assumed. There are two planes of reflective symmetry associated with this configuration, which follows from the 180° rotational symmetry. As with the t4b configuration, the symmetries associated with the t4c configuration significantly reduce the number of unique fullerene combinations involving the t4c configuration.

t4d

The t4d configuration was treated by the previous study [24] as if it possessed no reflective or rotational symmetry. We treat the t4d configuration in a different manner, as the configuration possesses a single plane of reflective symmetry, which is shown in Figure 6.5(b). This plane of symmetry reduces, in comparison with the previous study [24], the number of unique fullerene combinations involving the t4d configuration. The t4d configuration does not possess a 180° rotational symmetry (*i.e.* t4d $\neq$ t4d (R)).

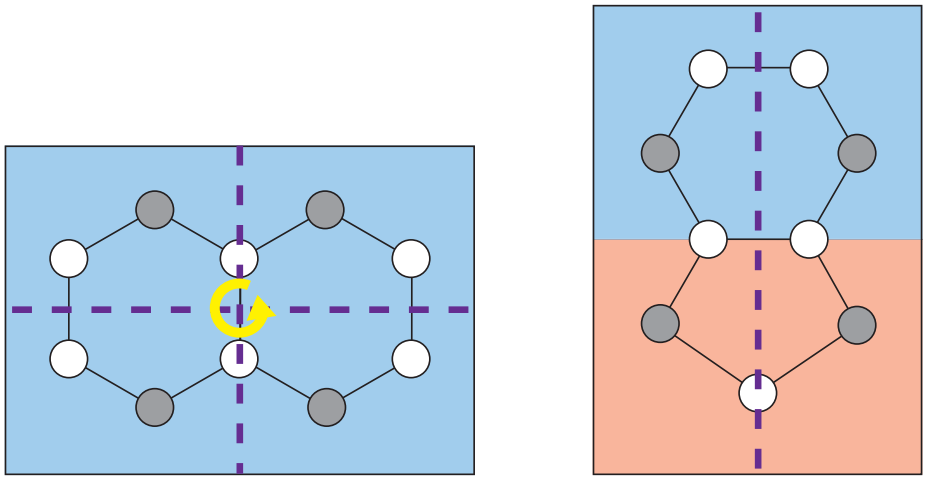

(a) t4c (b) t4d

Figure 6.5: Schematic illustrations demonstrating the symmetries associated with both the t4c and t4d configurations. The colouring scheme is the same as implemented in Figure 6.4.

t4g

The t4g configuration, as shown in Figure 6.6, is unique amongst all the t4 configurations in that it possesses no symmetry, be it reflective or rotational. The lack of symmetry, especially the configuration not possessing 180° rotational symmetry (*i.e.* t4g $\neq$ t4g (R)), seriously increases the number of unique combinations that the t4g configuration can form with the other configurations. We did consider treating the t4g configuration as having a (horizontal) plane of

symmetry, similar to the assumption made with the t4b configuration, however it was felt that the changes in the positioning of the fullerene would be more complex than the t4b configuration, so this potential assumption was dismissed.

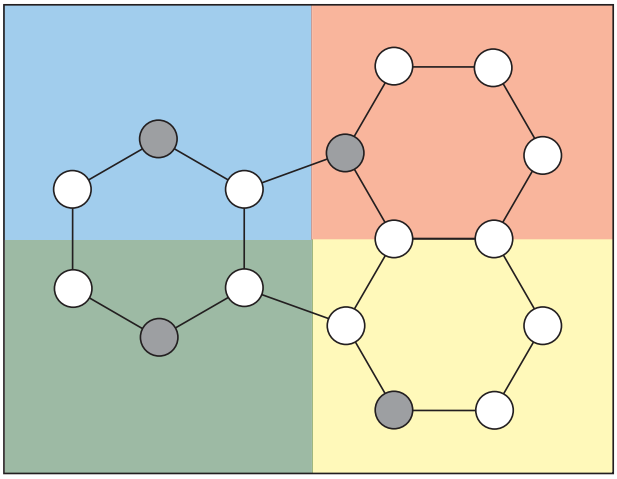

Figure 6.6: Schematic illustration demonstrating the lack of symmetries associated with the t4g configuration. The colouring of the regions signifies that all of the regions are unique.

t4h

The t4h configuration, shown in Figure 6.7(a), was treated in the previous study [24] as possessing no symmetry, rotational or otherwise. We have, however, treated the t4h configuration as possessing a 180° rotational symmetry (*i.e.* t4h = t4h (R)), which reduces the number of unique combinations the t4h configuration can form with the other configurations. There are no planes of reflective symmetry associated with the t4h configuration due to its unique "rotated" positioning. The t4h configuration does posses an equivalent rotational configuration, in which the fullerene molecule is rotated by 60°, however we have chosen not to include this equivalent configuration as it would further complicate the proceedings.

t4i

As with the t4d configuration, the t4i configuration was treated by the previous study [24] as if it possessed no reflective or rotational symmetry. Again, as with the t4d configuration, we chose to treat the t4i configuration as if it possesses a single plane of reflective symmetry, which is shown in Figure 6.7(b). This plane of symmetry reduces, in comparison with the previous study [24], the number of unique fullerene combinations involving the t4i configuration. The t4i configuration does not possess a 180° rotational symmetry (*i.e.* t4i $\neq$ t4i (R)).

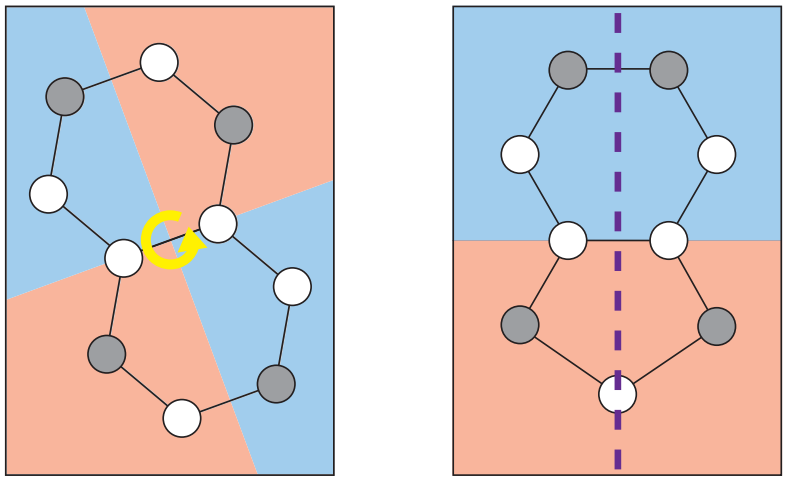

(a) t4h (b) t4i

Figure 6.7: Schematic illustrations demonstrating the symmetries associated with both the t4h and t4i configurations. The colouring scheme implemented is the same as used in Figure 6.4.

Fullerene bonding sites

The bonding sites for the pairs of fullerenes on the silicon surface required consideration, as the 2×2 tilted dimer reconstruction introduces an alternating dimer orientation, which complicates proceedings. Within this study we have chosen a separation between the two fullerenes that results in the two fullerene bonding sites being separated by one silicon dimer. This situation is illustrated in Figure

6.8:

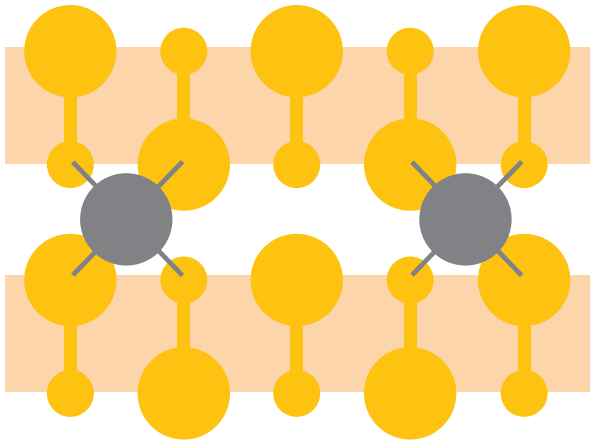

Figure 6.8: Schematic illustration of the two fullerene bonding sites on the Si (100) 2×2 tilted dimer surface reconstruction used within this study. The yellow circles represent the silicon atoms, with the size illustrating the atoms relative height (the larger circles are higher than the smaller ones). The relative height of the silicon atoms also illustrates the direction of the dimer tilt. The orange bar represents the dimer row, and the white space between the two rows represents the trench. The fullerene molecules are represented by the grey circles, and the C-Si bonds are also shown in grey.

The alternating nature of the 2×2 tilted dimer surface reconstruction means that the two fullerene bonding sites are not equivalent, as demonstrated in Figure 6.8. The separation between the two fullerenes that was implemented in the previous study [24] was smaller than the distance we have investigated in this study, and the smaller separation corresponded to having the two fullerene bonding sites adjacent to one another, as shown in Figure 6.9:

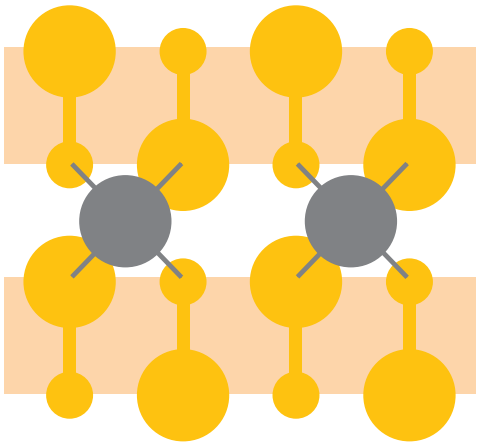

Figure 6.9: Schematic illustration of the two fullerene bonding sites on the Si (100) 2×2 tilted dimer surface reconstruction used within the previous study by Frangou. The colouring scheme used in this diagram is the same as implemented within Figure 6.8.

As is clear from Figure 6.9, the issue of non-equivalent fullerene bonding sites is not relevant for the C_{60} separation in the previous study [24]. We decided within this study to treat the two fullerene bonding sites as being equivalent to one another. While this assumption is not strictly true, within the aims of this study, we felt that the assumption was justified. If the two fullerene bonding sites were treated as unique, then the number of combinations that the set of t4 configurations could form with one another would increase significantly, which corresponds to a significant computational effort. This increased effort could come with potentially little gain, as it is debatable how much could be learned from treating the two fullerene bonding sites as unique.

Final set of unique combinations

The additional assumptions we have made, when compared to the previous study [24], have reduced the set of unique configurations of the fullerene pairs from 78 to 54. The full list of configurations is given below:

t4a - t4a	t4b - t4c	t4d - t4h
t4a (R) - t4a	t4b - t4d	t4d (R) - t4h
t4a - t4a (R)	t4b - t4g	t4d - t4i
t4a - t4b	t4b - t4g (R)	t4d (R) - t4i
t4a (R) - t4b	t4b - t4h	t4g - t4g
t4a - t4c	t4b - t4i	t4g (R) - t4g
t4a (R) - t4c	t4c - t4c	t4g - t4g (R)
t4a - t4d	t4c - t4d	t4g - t4h
t4a (R) - t4d	t4c - t4g	t4g (R) - t4h
t4a - t4g	t4c - t4g (R)	t4g - t4i
t4a (R) - t4g	t4c - t4h	t4g (R) - t4i
t4a - t4g (R)	t4c - t4i	t4g - t4i (R)
t4a (R) - t4g (R)	t4d - t4d	t4g (R) - t4i (R)
t4a - t4h	t4d (R) - t4d	t4h - t4h
t4a (R) - t4h	t4d - t4g	t4h - t4i
t4a - t4i	t4d (R) - t4g	t4h - t4i (R)
t4a (R) - t4i	t4d - t4g (R)	t4i - t4i
t4b - t4b	t4d (R) - t4g (R)	t4i (R) - t4i

If all of our assumptions were discarded (both on the symmetry of fullerenes and the fullerene bonding sites) then there would be several hundred unique configurations for which the computational time would be immense and of dubious value. Even the configurations that contain a high level of symmetry, such as the t4c configuration, would, in principle, have to be treated as possessing no symmetry at all, because in actuality the deformation of the fullerene cage (due to rebonding within the cage) would break the symmetry. This is also true of many other factors, such as the fact that the fullerenes do not sit exactly in the middle of the dimer trench, the differences in fullerene bonding sites, and so on. We believe that our assumptions are valid with respect to the interest of this

research, and within the limitations of practical realism.

6.4 Results

The results from our calculations are presented and discussed in this section. The full list of unique combinations of fullerene configurations have been successfully modelled and the measures of favourability and separation are given in Tables 6.3 to 6.9. This is a marked improvement from the previous study [24], as in those results (with a shorter seperation distance between the two fullerenes) only about half of the calculations relaxed into the desired configurations. This was attributed to the proximity of the fullerene cages, as often the cage with the weaker bonds would reorientate itself, often resulting in less C-Si bonds being formed and less favourable energies. Within our results this is not an issue, and in all cases all C-Si bonds are formed (four per C_{60} molecule). The t4d configurations are interesting because, as explained previously, there is always one C-Si bond that is considerably longer than the other three. In the isolated case this C-Si bond is 2.43 Å long, but throughout the combinations explored here this bond ranges from 2.26 to 2.55 Å. Another marked difference from the previous study [24], which again is a result of the differences in fullerene separation, is that in all of our systems of fullerene combinations there is no evidence of any C-C bonding taking place between the two C_{60} molecules. In the previous study a handful of combinations showed significant and complex C-C bonding occuring between the two fullerene cages.

The results given in Tables 6.3 to 6.9, are summarised and presented in Figure 6.10. The variation of the separation values for the all the combinations is shown to be $\sim$ 1.5 Å, which is about the same range as seen in the previous study [24]. This range is slightly more than we expected to see, as with the previous study, some of the combinations experienced bonding between the two fullerenes which would significantly reduce the distance between the two cages, so it was somewhat surprising to see the same range of values within our own

Config. 1	Config. 2	Favourability (in eV)	Separation (in Å)
t4a	t4a	-0.30	11.59
t4a (R)	t4a	-0.28	12.22
t4a	t4a (R)	-0.17	11.09
t4a	t4b	0.01	11.42
t4a (R)	t4b	-0.14	11.88
t4a	t4c	-0.13	11.37
t4a (R)	t4c	-0.35	11.87
t4a	t4d	-0.19	11.26
t4a (R)	t4d	-0.38	11.77
t4a	t4g	0.03	11.08
t4a (R)	t4g	-0.12	11.62
t4a	t4g (R)	-0.13	11.70
t4a (R)	t4g (R)	-0.29	12.17
t4a	t4h	-0.36	11.42
t4a (R)	t4h	-0.58	11.97
t4a	t4i	0.00	11.72
t4a (R)	t4i	-0.15	11.20

Table 6.3: The measure of favourability, in eV, and separation, in Å, for the configurations with the leftmost fullerene in either the t4a or t4a (R) configuration. The leftmost fullerene configuration is specified by the "Config. 1" column, and the rightmost fullerene configuration is specified by the "Config. 2" column.

Config. 1	Config. 2	Favourability (in eV)	Separation (in Å)
t4b	t4b	-0.16	11.59
t4b	t4c	-0.39	11.45
t4b	t4d	-0.42	11.35
t4b	t4g	-0.12	11.26
t4b	t4g (R)	-0.30	11.92
t4b	t4h	-0.61	11.56
t4b	t4i	-0.21	11.33

Table 6.4: The measure of favourability, in eV, and separation, in Å, for the configurations with the leftmost fullerene in the t4b configuration. The leftmost fullerene configuration is specified by the "Config. 1" column, and the rightmost fullerene configuration is specified by the "Config. 2" column.

Config. 1	Config. 2	Favourability (in eV)	Separation (in Å)
t4c	t4c	-0.44	11.34
t4c	t4d	-0.48	11.24
t4c	t4g	-0.27	11.09
t4c	t4g (R)	-0.36	11.61
t4c	t4h	-0.68	11.41
t4c	t4i	-0.24	11.19

Table 6.5: The measure of favourability, in eV, and separation, in Å, for the configurations with the leftmost fullerene in the t4c configuration. The leftmost fullerene configuration is specified by the "Config. 1" column, and the rightmost fullerene configuration is specified by the "Config. 2" column.

Config. 1	Config. 2	Favourability (in eV)	Separation (in Å)
t4d	t4d	-0.42	11.51
t4d (R)	t4d	-0.52	11.46
t4d	t4g	-0.29	11.25
t4d (R)	t4g	-0.21	11.35
t4d	t4g (R)	-0.45	11.92
t4d (R)	t4g (R)	-0.36	11.92
t4d	t4h	-0.68	11.63
t4d (R)	t4h	-0.62	11.67
t4d	t4i	-0.36	11.33
t4d (R)	t4i	-0.25	11.42

Table 6.6: The measure of favourability, in eV, and separation, in Å, for the configurations with the leftmost fullerene in either the t4d or t4d (R) configuration. The leftmost fullerene configuration is specified by the "Config. 1" column, and the rightmost fullerene configuration is specified by the "Config. 2" column.

Config. 1	Config. 2	Favourability (in eV)	Separation (in Å)
t4g	t4g	-0.41	11.46
t4g (R)	t4g	-0.29	10.78
t4g	t4g (R)	-0.77	11.68
t4g	t4h	-1.06	11.46
t4g (R)	t4h	-0.76	11.21
t4g	t4i	-0.70	11.17
t4g (R)	t4i	-0.35	11.02
t4g	t4i (R)	-0.64	11.31
t4g (R)	t4i (R)	-0.32	11.01

Table 6.7: The measure of favourability, in eV, and separation, in Å, for the configurations with the leftmost fullerene in either the t4g or t4g (R) configuration. The leftmost fullerene configuration is specified by the "Config. 1" column, and the rightmost fullerene configuration is specified by the "Config. 2" column.

Config. 1	Config. 2	Favourability (in eV)	Separation (in Å)
t4h	t4h	-0.80	11.55
t4h	t4i	-0.45	11.25
t4h	t4i (R)	-0.30	11.54

Table 6.8: The measure of favourability, in eV, and separation, in Å, for the configurations with the leftmost fullerene in the t4h configuration. The leftmost fullerene configuration is specified by the "Config. 1" column, and the rightmost fullerene configuration is specified by the "Config. 2" column.

Config. 1	Config. 2	Favourability (in eV)	Separation (in Å)
t4i	t4i	-0.13	11.51
t4i (R)	t4i	-0.38	11.23

Table 6.9: The measure of favourability, in eV, and separation, in Å, for the configurations with the leftmost fullerene in either the t4i or t4i (R) configuration. The leftmost fullerene configuration is specified by the "Config. 1" column, and the rightmost fullerene configuration is specified by the "Config. 2" column.

study. The majority of our results, in terms of the separation between the two fullerene cages, seem to be centred around the separation distance of 11.5 Å, which corresponds to the distance found in the experimental study [4] when the two fullerenes were in the same trench. In terms of system favourability, the vast majority ($\sim$ 94%) of the fullerene combinations are more favourable when considered as a combination pair, rather than as individual configurations. The range of favourability in our results is $\sim$ 1 eV, which is significantly reduced from the $\sim$ 14 eV range in favourability found in the previous study. This is down to two factors. First the separation is no longer an issue, as the bonding between the fullerenes in the previous study will have skewed the results, and secondly, at the separation we have chosen, the orientation of the two C_{60} molecules seems to have less of an influence over proceedings.

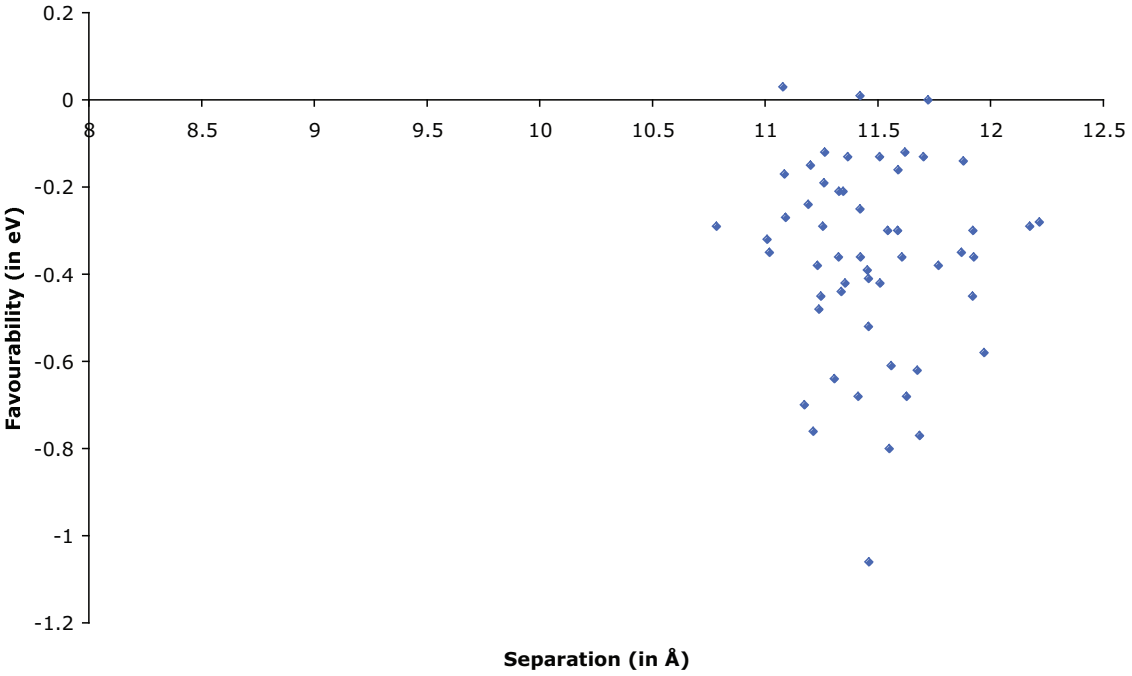

Figure 6.10: The separation between the centres of mass of the C_{60} cages plotted against the measure of favourability for the binding energy of the combined system when compared to the isolated cases.

When the results from the previous study [24] are combined with our own results, as shown in Figure 6.11, a few observations can be made. Firstly this helps put our results in context, as the variety that we have observed, in terms of the favourabilities, no longer seems to be significant. The trend of the fullerene pairings becoming more favourable continues, as the separation of the two fullerenes is increased. It also becomes noticable that the range of separations demonstrated might have more to do with the configurations in which the two fullerenes are placed, rather than any interaction between the two, as the range of separations shown for the two studies are very similar. As was concluded by the previous study [24], there does appear to be a general curve that could be used to represent the relationship between the separation of the two fullerene cages and the favourability of the combined system (with respect to the isolated systems), this conclusion gains extra weight as our results confirm the general pattern.

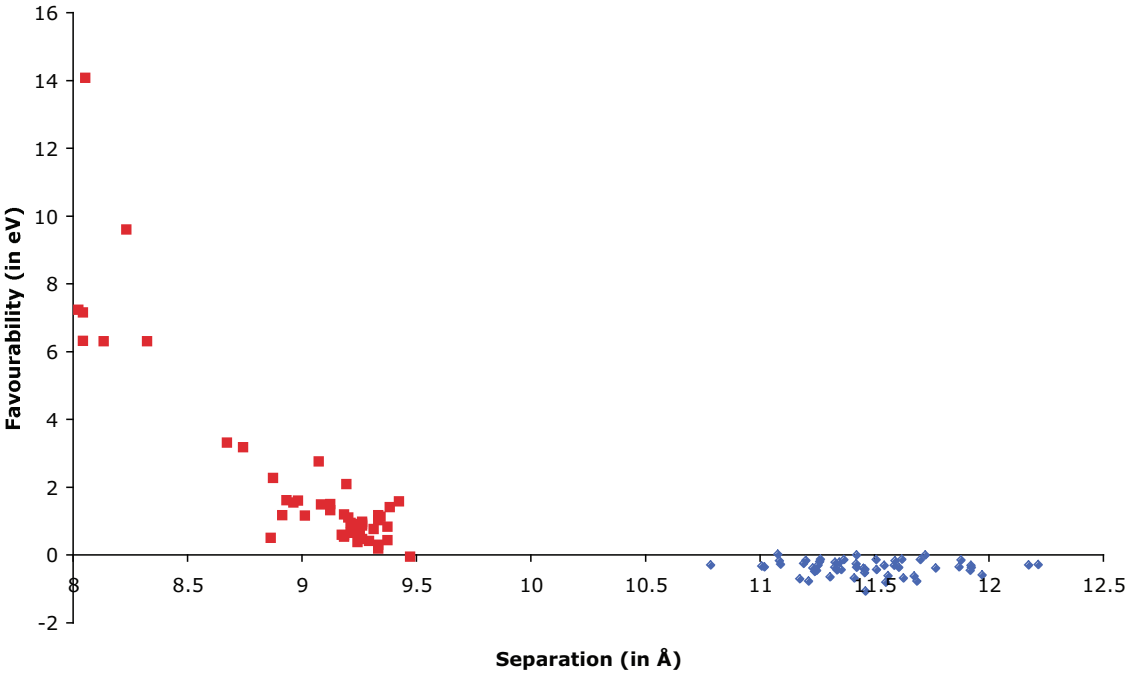

Figure 6.11: The separation between the centres of mass of the C_{60} cages plotted against the measure of favourability for the binding energy of the combined system when compared to the isolated cases. This plot includes the results from Figure 6.10 (the blue diamonds) and the results from the previous study by Frangou (the red squares).

The results for the isolated configurations, as shown in Table 6.1, are compared to the average binding energies for each of the configurations in Figure 6.12. These average binding energies were calculated by taking the mean value for each configuration, taking into account every combination that each configuration takes part in. Figure 6.12 shows that the difference between all the configurations is reduced when comparing the average binding energies, which is unsurprising as it could be expected that some of the more favourable configurations would compensate for some of the less favourable configurations. The most significant change between the binding energies of the isolated cases and the averages of the fullerene combinations, is for the t4h configuration, which moves in front of the t4d and t4i configurations and also closes up to the other

configurations. One possible explanation for this improvement in the t4h configuration could be that its unique "rotated" placement on the surface, makes one region of the cage closer than the other region, to the other fullerene. In the other configurations this is a lot more uniform, so it could account for the improvement observed in the t4h configuration.

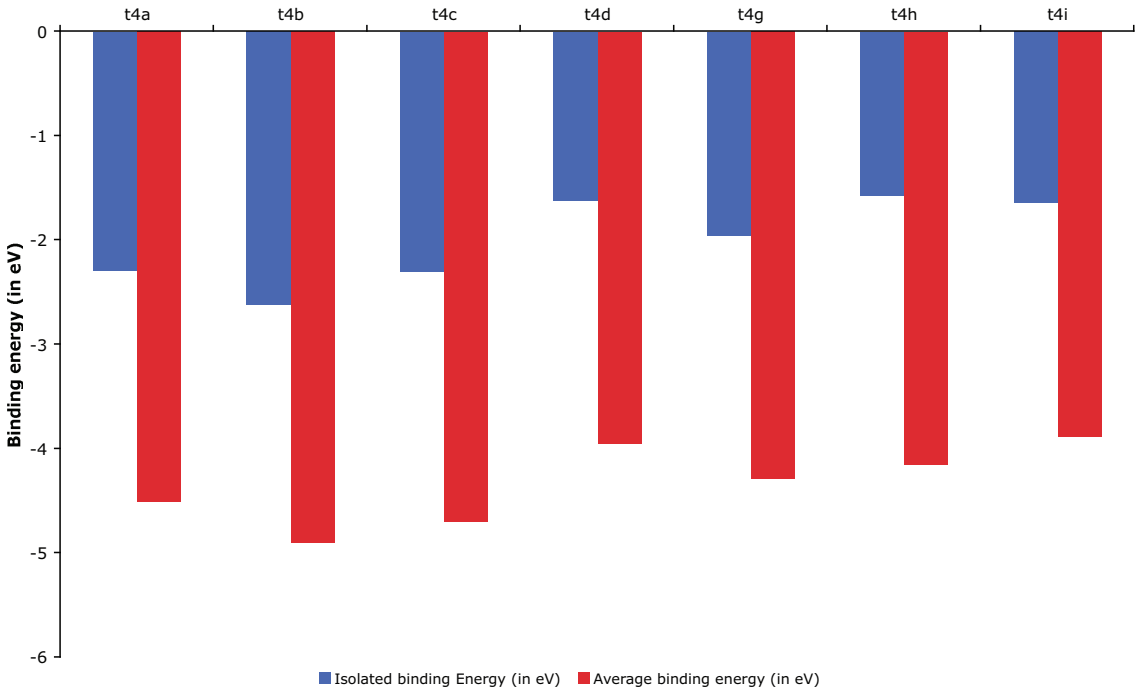

Figure 6.12: The binding energies for the isolated t4 configurations shown with the average binding energies for the combinations of fullerene pairs.

The average favourability graph, see Figure 6.13, futher illustrates the improvement in the t4h configuration when it is placed alongside another fullerene, compared with when it is in isolation. The t4h configuration is clearly the most favourable configuration for the other fullerenes to be combined with. This does however highlight that the t4h configuration is the most unfavourable configuration in isolation, so it is possible that this improvement has more to do with our method of calculating favourability than anything more significant. The results for the t4a configuration are interesting, as while it remains favourable in terms of the binding energies of both the isolated case and the fullerene pair

combinations, in terms of average system favourability it is the least favourable of all the configurations. It is possible that this is related to the fact it has the largest bonding configuration, in terms of the area of the fullerene cage that bonds with the fullerene surface. This could lead to a greater deformation within the fullerene cage, which would affect the area of the fullerene cage that is closest to the second fullerene. The only combinations that possess a non-negative favourability (meaning that the isolated components are more favourable than the combined pair), all involve the t4a configuration, which is obviously also going to affect the average favourabilities.

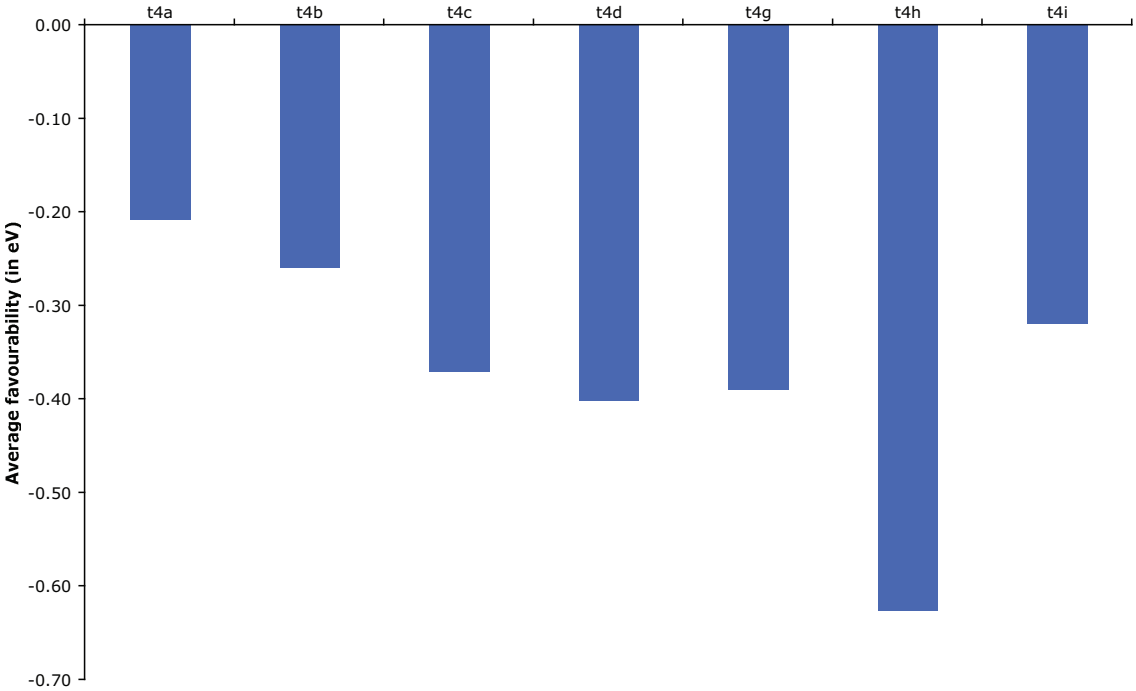

Figure 6.13: The average favourability, in eV, for each of the t4 configurations, from the results for the combinations of fullerene pairs.

In the following sub-sections we shall explore several of the outlier and more interesting cases, and investigate the reasons for the differences between these few combinations and the majority of the other combinations.

6.4.1 t4a-t4g

The combination of the t4a and t4g fullerene cages is one of the few combined fullerene systems that resulted in a positive favourability after the system's relaxation. As with all of our fullerene combinations there are no C-C bonds formed between the two cages. In Figure 6.14, we have compared the bond lengths for the eight C-Si bonds that have formed between the two C_{60} molecules and the silicon surface.

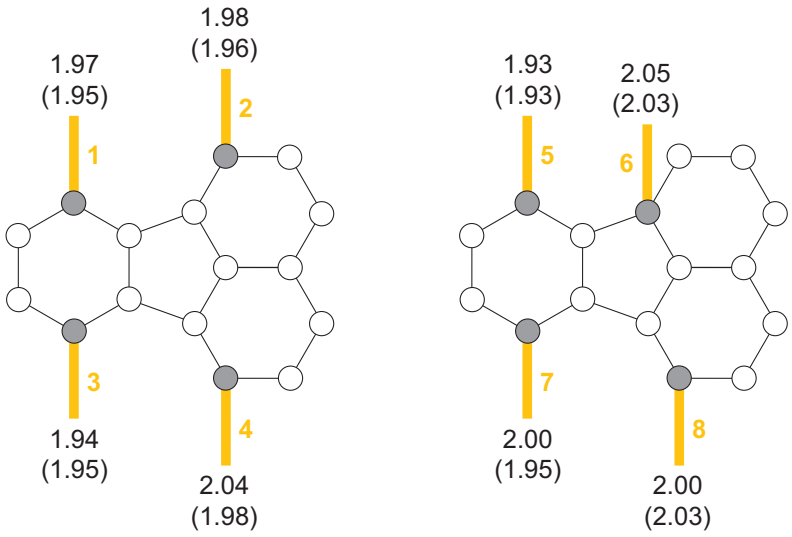

Figure 6.14: Bond lengths, in Å, for the C-Si bonds in the combined t4a-t4g system compared with the isolated cases for t4a and t4g (the values for the isolated cases are given within brackets). The t4a configuration is given on the left and the t4g configuration is given on the right.

As Figure 6.14 illustrates, the t4a cage generally shows, a lengthening of the bond lengths, bond 4 in particular shows a large increase. The same trend is found in the t4g cage, where bond 7 in particular shows a sizable increase in length. The energies for the C-Si bonds are given in Table 6.10.

Bond number	Combined system (in eV)	Isolated system (in eV)
1	-9.29	-9.95
2	-6.77	-6.65
3	-9.91	-9.91
4	-4.78	-6.45
5	-10.27	-10.12
6	-6.74	-8.21
7	-6.83	-8.77
8	-7.96	-6.98

Table 6.10: Bond energies, in eV, for the C-Si bonds in the combined t4a-t4g system compared with the isolated cases for t4a and t4g. The bond numbers correspond with those given in Figure 6.14

The results for the energies show a general weakening in the majority of C-Si bonds, in particular a large decrease in bond energies of bonds 4 and 7. The general trend shown here of a weakening and lengthening of the C-Si bonds, could account for why this combined fullerene system is less favourable than its isolated components.

6.4.2 t4a-t4b

The combination of the t4a and t4b fullerene cages is another one of the combined fullerene systems that resulted in a positive favourability after relaxation. Again, no C-C bonding between the two C_{60} molecules takes place. The bond lengths for the eight C-Si bonds that are formed upon the fullerene molecules adsorption upon the silicon surface, are given in Figure 6.15.

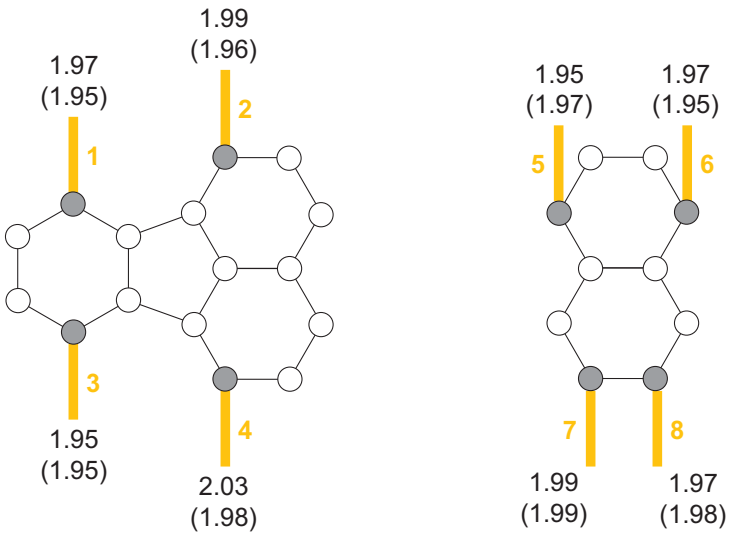

Figure 6.15: Bond lengths, in Å, for the C-Si bonds in the combined t4a-t4b system compared with the isolated cases for t4a and t4b (the values for the isolated cases are given within brackets). The t4a configuration is given on the left and the t4b configuration is given on the right.

The t4a cage illustrates the same trend in bond lengthening as found for the fullerene combination of the t4a-t4g orientations, although this occurs to a lesser extent. The t4b configuration appears, apart from a slight movement which results in two bonds swapping around, almost identical to the isolated configuration. The energies for the C-Si bonds are given in Table 6.11.

Bond number	Combined system (in eV)	Isolated system (in eV)
1	-9.30	-9.95
2	-6.39	-6.65
3	-9.82	-9.91
4	-5.23	-6.45
5	-9.27	-8.49
6	-8.57	-9.15
7	-7.32	-7.41
8	-7.78	-7.78

Table 6.11: Bond energies, in eV, for the C-Si bonds in the combined t4a-t4b system compared with the isolated cases for t4a and t4b. The bond numbers correspond with those given in Figure 6.15

The results for the bond energies of the t4a configuration show a general weakening of the C-Si bonds, however to a smaller extent than found in the t4a-t4g case (again the largest change occurs in bond 4). The energies in the t4b configuration show little change apart from the apparent swapping of bonds 5 and 6. The change in favourability of the t4a configuration within this combination leads to the combination being less favourable, although not to the extent of the t4a-t4g combination of fullerenes.

6.4.3 t4a-t4i

The combination of the t4a and t4i fullerene cages provides an interesting result, as the measure of favourability illustrates that there is no difference between the isolated configurations and the combination presented here. As with all of our combinations of fullerenes, no C-C bonding took place between the two fullerene molecules. The eight C-Si bonds that form between the two C_{60} molecules and the silicon surface have their bond lengths illustrated in Figure 6.16.

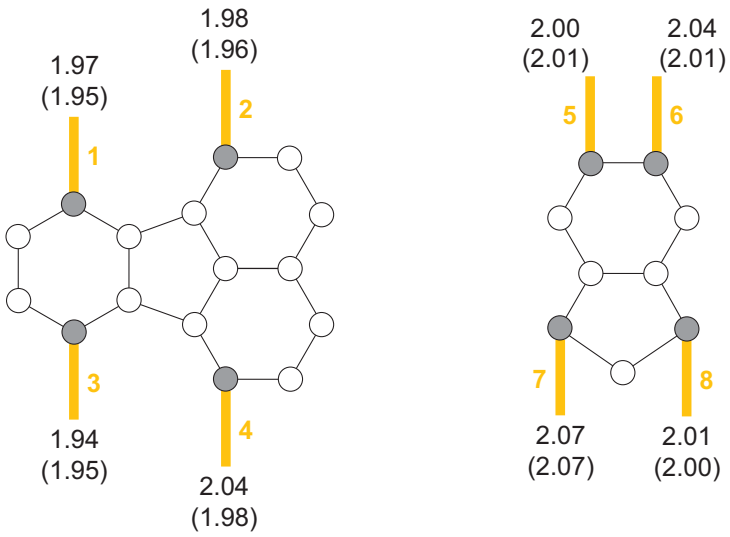

Figure 6.16: Bond lengths, in Å, for the C-Si bonds in the combined t4a-t4i system compared with the isolated cases for t4a and t4i (the values for the isolated cases are given within brackets). The t4a configuration is given on the left and the t4i configuration is given on the right.

The t4a cage illustrates an almost identical change to the t4a cage within the t4a-t4g combination of fullerenes. The t4i cage, with the exception of the slight lengthening of bond 6, shows very little change in bond lengths compared to the isolated case. The energies for these C-Si bonds are given in Table 6.12.

Bond number	Combined system (in eV)	Isolated system (in eV)
1	-9.27	-9.95
2	-7.14	-6.65
3	-9.93	-9.91
4	-4.79	-6.45
5	-5.45	-4.59
6	-5.56	-6.07
7	-3.81	-4.24
8	-7.11	-7.20

Table 6.12: Bond energies, in eV, for the C-Si bonds in the combined t4a-t4i system compared with the isolated cases for t4a and t4i. The bond numbers correspond with those given in Figure 6.16

The results for the t4a fullerene show a similar, but more favourable, trend of bond weakening (in the case of bond 2, a strengthening), as in the t4a-t4g fullerene combination. The t4i configuration shows a slight weakening of three of the bonds and a reasonable strengthening in the remaining bond. The changes in bond length and energies probably could result in a slightly positive favourability, however, the magnitude of the changes are small, so perhaps it is unsurprising not to see a difference in favourability in the combined system compared to the isolated configurations.

6.4.4 t4g-t4h

The combination of the t4g and t4h fullerene cages is the most favourable configuration found, out of all 54 systems that have been investigated. There is no C-C bonding between the two C_{60} molecules, so the increase in favourability presumably comes from the C-Si bonds. The lengths of these eight C-Si bonds is explored in Figure 6.17.

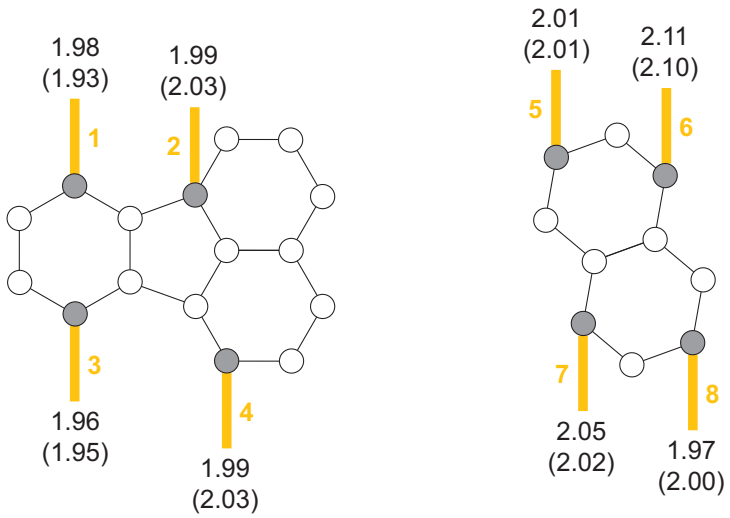

Figure 6.17: Bond lengths, in Å, for the C-Si bonds in the combined t4g-t4h system compared with the isolated cases for t4g and t4h (the values for the isolated cases are given within brackets). The t4g configuration is given on the left and the t4h configuration is given on the right.

The t4g cage is interesting as while the shorter bonds (1 and 3) have become longer, the longer bonds (2 and 4) have become shorter. This leaves the four C-Si bonds for the t4g cage of a much more uniform length. The t4h cage shows little overall change in terms of bond lengths, compared to the isolated system. The energies for these C-Si bonds are given in Table 6.13.

Bond number	Combined system (in eV)	Isolated system (in eV)
1	-8.73	-10.12
2	-8.54	-8.21
3	-9.45	-8.77
4	-7.29	-6.98
5	-7.59	-6.90
6	-3.92	-4.26
7	-4.94	-5.82
8	-7.82	-6.83

Table 6.13: Bond energies, in eV, for the C-Si bonds in the combined t4g-t4h system compared with the isolated cases for t4g and t4h. The bond numbers correspond with those given in Figure 6.17

The t4g C-Si bond energies further illustrate a more uniform type of bonding, with the energies becoming closer to one another. The t4h configuration show slight increases and decreases, in terms of bond energies, that probably cancel each other out. It is likely that the overall changes in the t4g cage, which seem to stabilise the configuration, account for the increased favourability of the system, as the difference between the isolated and combined t4h cage is too minimal to account for the combined systems favourability.

6.5 Conclusions

The clear trend suggested by the previous study [24], that showed a relationship between the separation of the two C_{60} molecules upon the silicon surface and the resulting favourability of the combination of the two configurations when compared to the two isolated cases, is confirmed with this work. As the distance between the two C_{60} molecules is increased, the stability of the system increases. The two studies result in two distinct groups of separations; in order to achieve

fullerene separations in between the two studies the t2 configuration group would have to be employed for one or more of the two C_{60} molecules. This would be difficult to model, as the t2 configurations are not known for their inherent stability.

All of our calculations resulted in the desired fullerene configurations after the relaxation had been performed, with all the correct C-Si bonds being formed. These C-Si bonds seem to play a significant role in the stability of the combined systems. The range of favourabilities for all of our results are $\sim$ 1 eV, which is quite small and would imply that while the configurations chosen do affect the favourability, the extent to which they do is significantly reduced from the previous study [24].

In the previous experimental study [4] that explored the manipulation of C_{60} molecules upon the silicon surface using a STM tip, the closest the two C_{60} molecules could be manipulated to each other and have both fullerene molecules remain within the same trench was 11.5 Å. The range of separations found in our study are between $\sim$ 10.75 to $\sim$ 12.25 Å, with the majority of the results in the $\sim$ 11.5 Å area. This shows an excellent level of agreement with the experimental study.

Chapter 7

Conclusions

In Chapter 3 an extensive computer programming project was outlined, and subsequently undertaken in order to allow for a more complete description of atoms within calculations performed with PLATO. This was achieved by a re-evaluation of how the Slater-Koster integrals and their derivatives were calculated within PLATO and its associated support programs. Previously within PLATO an analytic method was utilised in order to calculate the Slater-Koster integrals and their derivatives; the intention being to replace this analytic method with a recursive method [20, 21]. After the successful implementation of the recursive method, it was clear that the recursive method could potentially slow down calculations; thus a compromise was reached whereby the analytic method became the default method for the calculation of the Slater-Koster integrals and their derivatives, leaving the recursive method to complement the analytic method, whereby it is only used when required. This achieved the aim of extending the capabilities of PLATO, while still maintaining the computational speed of the calculations. Further to the addition of the recursive Slater-Koster method, various alterations and generalisations were made to the remainder of the programs; these resulted in PLATO being able to perform calculations that included f-orbitals (and even orbitals of higher quantum angular momenta).

A series of tests were then performed in order to assess the relative improvement in accuracy, and the computational impact of including f-orbitals within

our basis sets. The systems tested contained silver, silicon and nitrogen atoms (each of the systems contained only one atom species). In all calculations involving f-orbitals there were modest increases in the accuracy of the bulk properties, system energies, and bond lengths calculated. The computational cost of including f-orbitals with basis sets was mixed, with both increases and decreases in simulation times attributed to their inclusion. For example, the static relaxations performed on the silver systems experienced a reduction in simulation time when the f-orbitals were included. This was due to the calculations in question taking less self-consistent loops within PLATO to achieve the required force tolerance, which, it is believed is due to the more complete description offered by the basis sets with f-orbitals included. The silver single point calculations involving f-orbitals did not benefit from this decrease in computational time, as in these calculations there is only one self-consistent loop, so the increased completion of the basis sets including f-orbitals becomes a hinderance rather than a benefit.

Overall it was concluded that the potential gain in accuracy might be small, however, the computational times could be both positively and negatively affected (depending on the system in question and the calculation to be performed). Thus careful consideration would be required in order to describe when to include f-orbitals in basis sets for PLATO calculations, especially in systems that do not traditionally require f-orbitals. The extension of PLATO does, however, offer a higher level of precision in calculations than was previously possible, and with it the scope to investigate systems with atomic species that do require f-orbitals.

In Chapter 5 we explored the adsorption of C_{60} and N@C_{60} molecules upon the Si (100) surface, focussing on the r2 and t4 groups of configurations which previous studies [2, 14, 15, 16, 17] had indicated as the most favourable configuration groups. We have used the same standard of completedness for our basis set as the previous study [17]. However for the endohedral nitrogen atom we took advantage of the f-orbital extension in PLATO for a more accurate

description. A variety of checks were performed to ascertain the effect on the endohedral nitrogen atom by the fullerene, and the effect that the fullerene has on the endohedral atom. It was shown that in general the presence of an endohedral atom caused little change in how the C-Si bonds were formed, and in the C-C rebonding within the fullerene cage itself. There was very little change in the spin on the nitrogen atom, and the charge transfer between the endohedral nitrogen atom and the fullerene cage was minimal. The endohedral nitrogen atom was also shown to be only slightly displaced from the centre of mass of the fullerene cage. In general the binding energies for the N@C_{60} molecules were more favourable than the C_{60} molecules. Our binding energies for the C_{60} molecules showed some slight differences when compared to those published previously [14, 16, 17], however, these can be explained by the differences in surface reconstruction implemented, and the large range of metastable states for the adsorption of the fullerene molecules upon the silicon surface.

There were two outlying configurations, the r2g and t4g configurations, in terms of the binding energies when comparing the C_{60} and N@C_{60} configurations. Both of these cases showed a larger increase in favourability for the N@C_{60} configurations compared to the C_{60} configurations, than observed elsewhere. The r2g configuration's difference in binding energies can be explained as the charge transfer to the endohedral nitrogen atom is amongst the highest for all the N@C_{60} configurations. The endohedral nitrogen atom in the N@C_{60} r2g configuration is also an outlier in terms of the spin on the atom, as this spin is lower than expected. The N@C_{60} t4d configuration is a metastable minimum, where it is the very presence of the endohedral atom itself that affects the C-Si bonds formed between the fullerene and the silicon surface. These C-Si bond lengths are reduced, which leads to a more favourable binding energy for the N@C_{60} t4d case. Overall, our work provided evidence that the endohedral nitrogen atom was almost perfectly isolated within the fullerene cage, which is of vital importance in order to achieve the intended application of the endohedral fullerene molecule as a quantum computing qubit.

In Chapter 6 systems involving pairs of fullerenes were investigated. Prior to this, a brief exploration of the impact of the periodic fullerene repeats on the systems' properties was undertaken. It was shown that the results from previous studies [2, 14, 15, 16, 17] and those in Chapter 5, experience a level of interaction between the fullerene and its periodic repeats, which skews the systems' energies, most likely leading to an increase in the configuration's favourabilities. The work from the previous computational study on multiple fullerenes [24] was then extended. The previous study had the two fullerenes bonding onto the silicon surface at adjacent bonding sites, whereas our study had the two bonding sites separated by one silicon dimer. As with the previous study only a selection of t4 configurations were explored. The separation our study investigated was more in keeping with the separations found in experimental work [4]. The separations for our relaxed fullerene molecules were found to be between ~ 10.75 to ~ 12.25 Å, with the majority being ~ 11.5 Å, which coincides with the separation found in the aforementioned experimental study.

The pairs of fullerene configurations were more favourable than their isolated components in nearly all ($\sim 94\%$) of the cases. The cases where the isolated components are more favourable than the combined pair, all include the t4a configuration for one of the fullerenes. This affects the average system favourability for the t4a configuration, making it the least favourable of all the configurations examined. This could be related to the size of the rebonding in the fullerene cage for the t4a configuration, which is the largest of all t4 configurations, which might lead to a greater deformation within the fullerene cage. The three configurations that possess a positive favourability (which corresponds to the isolated components being more favourable than the pair) are the t4a-t4g, t4a-t4b and t4a-t4i configuration combinations. In all of these cases there is a distinct increase in the C-Si bond length in the combined system compared to the isolated components, and these C-Si bonds also become weaker in terms of the bond energies. As stated previously, the vast majority of the pairs of fullerenes were more favourable as pairs than their isolated components, the most favourable

being the t4g-t4h combination. In this case the change in bonding between the t4h cage and its isolated counterpart was minimal, however, the t4g cage showed significant changes in the C-Si bonds formed, with both the bond lengths and bond energies becoming more favourable, which accounts for the combined systems favourablity.

In general, the difference between the combined system and its isolated components was usually less than 1 eV; this is in stark contrast to the previous computational study [24] which had a range of favourabilities $\sim$ 14 eV for its combinations. This can be accounted for by the difference in separation between the two fullerene molecules, as with the previous study the fullerenes were much closer than in our own study, so that in some cases C-C bonding occured between the two fullerene cages, which significantly skewed their results. No C-C bonding between the two fullerenes occured in any of our pairs, which can be attributed to the increased separation between the two fullerenes. The general trend displayed by our results is that at the separation distance chosen for our study, the two fullerenes are more favourable as pairs than as isolated components. In contrast the previous study [24], which investigated a smaller separation distance than our own, found the pairs of fullerenes to be less favourable than the isolated components.

7.1 Future studies

Our work, discussed in Chapter 3, possesses the greatest scope for future studies, as it extends the potential of PLATO, the code with which our calculations were performed. Previously the TNDP basis sets provided the highest available precision within PLATO, but that is no longer the case. As was illustrated in Chapter 3, relatively simple calculations involving silicon and silver atoms could be improved with the addition of f-orbitals. Theoretically this would mean that all previous studies that have used PLATO, could be repeated with higher precision, although the actual benefit of doing so would, in the majority of cases,

be debatable. The main scope for further studies, that this work enables, is the study of systems involving the Lanthanide (this consists of elements with atomic numbers between 57 and 71, so La through to Lu) and Actinide (this consists of elements with atomic numbers between 89 and 103, so Ac through to Lr) series of elements, as these species require f-orbitals in order to accurately model them.

Following on from our own studies with fullerenes, there is still further scope for investigation. An important question raised within our research is how the choice of simulation cells can affect the calculation due to the impact of the periodic fullerene repeats. Our intial work in this area (see Chapter 6) suggests that this impact is greater than previously anticipated. Following on from this we feel that reinvestigating the r2 fullerene configurations (where the fullerene is above the dimer row and centred between two dimers) would be worthwhile. These configurations are only found at high temperatures experimentally [4], yet within computational calculations [2, 14, 15, 16, 17] they are found to be relatively favourable. When the t4 fullerene configurations were investigated in Chapter 6 on the second larger surface, the whole group became less favourable, so it stands to reason that the r2 group would also be affected (possibly to a greater extent, which would tie in with the experimental results).

The work on multiple fullerenes (see Chapter 6) could be extended by first looking at different pairings of configurations, for example, combinations of r2 and t4 configurations. The distances between the two fullerenes could be further investigated by using a t4 configuration for one fullerene and a t2 configuration for the other fullerene, as this could reduce the distance between the two molecules. The experimental study [4] found that the closest that the two fullerenes could be manipulated was 9.5 Å, which only occured when the fullerenes were in adjacent trenches. This could be investigated via computational calculations such as the ones implemented here.

All of the calculations with multiple fullerenes could be repeated with combinations of one or two endohedrally doped fullerenes, extending the work of Chapter 5. Further endohedral topics of study could include the investigation

of other candidate species, as phosphorus has previously been discussed as an endohedral species for the fullerene qubit [5, 6]. Beyond the immediate scope of our research, many further studies in the field could be performed, for example, larger fullerene cages, different endohedral species (or molecules), and chains of fullerenes, endohedrally doped or otherwise. The fullerene chains could, for example, have alternating endohedral species, as discussed in [6]. The study of fullerenes and the potential applications of them, remains a topic for which further study is not just interesting, but important.

Bibliography

[1] H.W. Kroto, J.R. Heath, S.C. O'Brien, R.F. Curl, and R.E. Smalley. C_{60}: Buckminsterfullerene. *Nature*, 318:14, 1985.

[2] P.D. Godwin, S.D. Kenny, R. Smith, and J. BelBruno. The structure of C_{60} and endohedral C_{60} on the Si (100) surface. *Surface Science*, 490:409, 2001.

[3] D.L. Keeling, M.J. Humphry, P. Moriarty, and P.H. Beton. Attractive mode manipulation of covalently bound molecules. *Chemical Physics Letters*, 366:300, 2002.

[4] P. Moriarty, Y.R. Ma, M.D. Upward, and P.H. Beton. Translation, rotation and removal of C_{60} on Si (100) - 2×1 using anisotropic molecular manipulation. *Surface Science*, 407:27, 1998.

[5] W. Harneit, C. Meyer, A. Weidinger, D. Suter, and J. Twamley. Architectures for a Spin Quantum Computer Based on Endohedral Fullerenes. *Physics Status Solidi B*, 233:453, 2002.

[6] J. Twamley. Quantum-cellular-automata quantum computing with endohedral fullerenes. *Physical Review A*, 67:052318, 2003.

[7] T. Hashizume, X.D. Wang, Y. Nishina, H. Shinohara, Y. Saito, Y. Kuk, and T. Sakurai. Field Ion-Scanning Tunneling Microscopy Study of c_{60} on the Si (100) Surface. *Japanese Journal of Applied Physics*, 31:880, 1992.

[8] X.D. Wang, T. Hashizume, Y. Shinohara, Y. Nishina, and T. Sakurai. Adsorption of C_{60} and C_{84} on the Si (100) - 2×1 surface studied by using the scanning tunneling microscope. *Physical Review B*, 47:15923, 1993.

[9] D. Chen and D. Sarid. Growth of C_{60} films on silicon surfaces. *Surface Science*, 318:74, 1994.

[10] D. Klyachkko and D.M. Chen. Ordering of C_{60} on Anisotropic Surfaces. *Physical Review Letters*, 75:3693, 1995.

[11] M.J. Butcher, M.J. Humphry, P. Moriarty, P.H. Beton, K. Passides, K. Kordatos, and N. Tagmatarchis. Room temperature manipulation of the heterofullerene $C_{59}N$ on Si (100) - 2×1. *Applied Physics Letters*, 75:1074, 1999.

[12] D.L. Keeling, M.J. Humphry, R.H.J. Fawcett, P.H. Beton, C. Hobbs, and L. Kantarovich. Bond Breaking Coupled with Translation in Rolling of Covalently Bound Molecules. *Physical Review Letters*, 94:146104, 2005.

[13] M.J. Butcher, J.W. Nolan, M.R.C. Hunt, P.H. Beton, L. Dunsch, P. Kuran, P. Georgi, and T.J.S. Dennis. Adsorption and manipulation of endohedral and higher fullerenes on Si (100) - 2×1. *Physical Review B*, 67:125413, 2003.

[14] P.D. Godwin, S.D. Kenny, and R. Smith. The bonding sites and structure of C_{60} on the Si (100) surface. *Surface Science*, 529:237, 2003.

[15] C. Hobbs and L. Kantarovich. Adsorption of C_{60} on the Si (001) surface calculated within the generalized gradient approximation. *Nanotechnology*, 15:S1, 2004.

[16] C. Hobbs, L. Kantarovich, and J.D. Gale. An *ab-initio* study of C_{60} adsorption on the Si (001) surface. *Surface Science*, 591:45, 2005.

[17] P.C. Frangou, S.D. Kenny, and E. Sanville. Adsorption of C_{82} on Si (100). *Surface Science*, 602:1532, 2008.

[18] S.D. Kenny, A.P. Horsfield, and H. Fujitani. Transferable atomic-type orbital basis sets for solids. *Physical Review B*, 62:4899, 2000.

[19] J.C. Slater and G.F. Koster. Simplified LCAO Method for the Periodic Potential Problem. *Physics Review*, 94:1498, 1954.

[20] A.V. Podolskiy and P. Vogl. Compact expression for the angular dependence of tight-binding Hamiltonian matrix elements. *Physical Review B*, 69:233101, 2004.

[21] A.M. Elena and M. Meister. Automatic generation of matrix element derivatives for tight binding models. *Physical Review B*, 72:165107, 2005.

[22] P.H. Beton, A.W. Dunn, and P. Moriarty. Manipulation of C_{60} molecules on a Si surface. *Applied Physics Letters*, 67:8, 1995.

[23] B. Pietzak, M. Waiblinger, T. Alemeida Murphy, A. Weidinger, M. Höhne, E. Dietel, and A. Hirsch. Buckminsterfullerene C_{60}: a chemical Faraday cage for atomic nitrogen. *Chemical Physics Letters*, 279:259, 1997.

[24] P.C. Frangou. *Modelling of fullerenes on silicon surfaces.* PhD thesis, Loughborough University, 2008.

[25] M. Born and J.R. Oppenheimer. On the Quantum Theory of Molecules. *Annals Of Physics*, 84:457, 1927.

[26] W. Kohn and L.J. Sham. Self-Consistent Equations Including Exchange and Correlation Effects. *Physical Review A*, 140:1133, 1965.

[27] P. Hohenberg and W. Kohn. Inhomogeneous Electron Gas. *Physical Review B*, 136:864, 1964.

[28] J.P. Perdew, K. Burke, and M. Ernzerhof. Why the Generalized Gradient Approximation Works and How to Go Beyond It. *International Journal Of Quantum Chemistry*, 61:287, 1997.

[29] J.P. Perdew, K. Burke, and M. Ernzerhof. Generalized Gradient Approximation Made Simple. *Physical Review Letters*, 77:3865, 1996.

[30] C. Hartwigsen, S. Goedecker, and J. Hutter. Relativistic separable dual-space Gaussian psuedopotentials from H to Rn. *Physical Review B*, 58:3641, 1998.

[31] S. Boys and F. Bernardi. The calculation of small molecular interactions by the differences of separate total energies. Some procedures with reduced errors. *Molecular Physics*, 19:553, 1970.

[32] E. Sanville, S.D. Kenny, R. Smith, and G. Henkelman. Improved Grid-Based Algorithm for Bader Charge Allocation. *Journal Of Computational Chemistry*, 28:899, 2007.

[33] R. Bader. *Atoms In Molecules: A Quantum Theory.* Oxford University Press, 1990.

[34] G. Bozzolo, J.E. Garcés, and G.N. Derry. Atomistic modeling of segregration and bulk ordering in Ag-Au alloys. *Surface Science*, 601:2038, 2007.

[35] W.-K. Leung, R.J. Needs, and G. Rajagopal. Calculations of Silicon Self-Interstitial Defects. *Physical Review Letters*, 83:2351, 1999.

[36] S. Goedecker, T. Deutsch, and L. Billard. A Fourfold Coordinated Point Defect in Silicon. *Surface Science*, 88:235501, 2002.

[37] P.W. Fowler and D.E. Manopoulos. *An Atlas of Fullerenes.* Oxford University Press, 1995.

[38] H.W. Kroto. The stability of the fullerenes c_n, with n = 24, 28, 32, 36, 50, 60, 70. *Nature*, 329:529, 1987.

[39] D.M. Eigler and E.K Schweizer. Positioning single atoms with a scanning tunnelling microscope. *Nature*, 344:524, 1990.

[40] S. Maruno, K. Inanaga, and T. Isu. Theshold height of movement of C_{60} molecules of Si (111) - 7×7 with a scanning tunneling microscope. *Applied Physics Letters*, 63:1339, 1993.

[41] Y.Z. Li, M. Chander, J.C. Patrin, J.H. Weaver, L.P.F. Chibante, and R.E. Smalley. Adsorption of individual C_{60} molecules on si (111). *Physical Review B*, 45:13837, 1992.

[42] L. Bartels, G. Meyer, and K.-H. Rieder. Basic Steps of Lateral Manipulation of Single Atoms and Diatomic Clusters with a Scanning Tunneling Microscope Tip. *Physical Review Letters*, 79:697, 1997.

[43] D.S. Bethune, D.R. Johnson, J.R. Salem, M.S. de Vries, and C.S. Yannoni. Atoms in carbon cages: the structure and properties of endohedral fullerenes. *Nature*, 366:123, 1993.

[44] R. Tellgmann, N. Krawez, S.-H. Lin, I.V. Hertel, and E.E.B. Campbell. Endohedral fullerene production. *Nature*, 382:407, 1996.

[45] M. Saunders, R.J. Cross, A. Jimenez-Vazquez, R. Shimshi, and A. Khong. Noble Gas Atoms Inside Fullerenes. *Science*, 271:1693, 1996.

[46] T. Alemeida Murphy, T. Pawlik, A. Weidinger, M. Höhne, R. Alcala, and J.M. Spaeth. Observation of Atomlike Nitrogen in Nitrogen-Implanted Solid C_{60}. *Physical Review Letters*, 77:1075, 1996.

[47] D.G. Cory, R. Laflamme, E. Knill, L. Viola, T.F. Havel, N. Boulant, G. Boutis, E. Fortunato, S. Lloyd, R. Martinez, C. Negrevergne, M. Pravia, Y. Sharf, G. Teklemariam, Y.S. Weinstein, and W.H. Zurek. NMR Based Quantum Information Processing: Achievements and Prospects. *Fortschritte der Physik*, 48:875, 2000.

[48] L.M.K. Vandersypen, M. Steffen, G. Breyta, C.S. Yannoni, M.H. Sherwood, and I.L. Chuang. Experimental realization of Shor's quantum factoring algorithm using nuclear magnetic resonance. *Nature*, 414:883, 2001.

[49] J.A. Jones. NMR Quantum Computation: A Critical Evaluation. *Fortschritte der Physik*, 48:909, 2000.

[50] B.E. Kane. A silicon-based nuclear spin quantum computer. *Nature*, 393:133, 1998.

[51] D. Loss and D.P. DiVincenzo. Quantum computation with quantum dots. *Physical Review A*, 57:120, 1998.

[52] C. Knapp, K. P. Dinse, B. Pietzak, M. Waiblinger, and A. Weidinger. Fourier transform EPR study of $N@C_{60}$ in solution. *Chemical Physics Letters*, 272:433, 1997.

[53] K. Lips, M. Waiblinger, B. Pietzak, and A. Weidinger. Atomic Nitrogen Encapsulated in Fullerenes: Realization of a Chemical Faraday Cage. *Physica Status Solidi (a)*, 177:81, 2000.

[54] M. Waiblinger, K. Lips, W. Harneit, A. Weidinger, E. Dietel, and A. Hirsch. Thermal stability of the endohedral fullerenes $N@C_{60}$, $N@C_{70}$, and $P@C_{60}$. *Physical Review B*, 64:159901, 2001.

[55] S. Lloyd. A Potentially Realizable Quantum Computer. *Science*, 261:1569, 1993.

[56] S. C. Benjamin. Schemes for parallel quantum computation without local control of qubits. *Physical Review A*, 61:020301, 2000.